X-660-77-85

TMX 71309

# STUDIES ON SOLAR HARD X-RAYS AND GAMMA-RAYS: COMPTON BACKSCATTER, ANISOTROPY, POLARIZATION AND EVIDENCE FOR TWO PHASES OF ACCELERATION

(NASA-TM-X-71309) STUDIES ON SOLAR HARD X-RAYS AND GAMMA-RAYS: COMPTON BACKSCATTER, ANISOTROPY, POLARIZATION AND EVIDENCE FOR TWO PHASES OF ACCELERATION Ph.D. Thesis - Maryland Univ. (NASA) 159 p HC A08/MF A01 G3/93 N77-24048 Unclas 28948

T. BAI

APRIL 1977

GSFC — GODDARD SPACE FLIGHT CENTER —
GREENBELT, MARYLAND

MAY 1977
RECEIVED
NASA STI FACILITY
INPUT BRANCH

For information concerning availability
of this document contact:

Technical Information & Administrative Support Division
Code 250
Goddard Space Flight Center
Greenbelt, Maryland 20771

(Telephone 301—982—4488)

"This paper presents the views of the author(s), and does not necessarily reflect the views of the Goddard Space Flight Center, or NASA."

# STUDIES ON SOLAR HARD X-RAYS AND GAMMA-RAYS: COMPTON BACKSCATTER, ANISOTROPY, POLARIZATION, AND EVIDENCE FOR TWO PHASES OF ACCELERATION

by

Taeil Bai

Dissertation submitted to the Faculty of the Graduate School
of the University of Maryland in partial fulfillment
of the requirements for the degree of
Doctor of Philosophy
1977

*Supported in part by NASA Grant NGL21-002-316

ABSTRACT

Title of Thesis: Studies on Solar Hard X-Rays and Gamma-Rays: Compton Backscatter, Anisotropy, Polarization, and Evidence for Two Phase of Acceleration

Taeil Bai, Doctor of Philosophy, 1977

Thesis directed by: Frank B. McDonald
Professor of Physics

This thesis deals with the theory of hard x-ray emission from solar flares, with emphasis upon the following two aspects of this radiation: the Compton backscatter of X-rays from the solar photosphere, and bremsstrahlung in the transition energy region from non-relativistic to relativistic electron energies.

Hard X-rays incident upon the phosphere with energies $\gtrsim 15$ keV have high probabilities of backscatter due to Compton collisions with electrons. This effect has a strong influence on the spectrum, intensity and polarization of solar hard X-rays--especially for anisotropic models in which the primary X-rays are emitted predominantly toward the photosphere. We have carried out a detailed study of X-ray backscatter, and we have investigated the interrelated problems of anisotropy, polarization, and center-to-limb variation of the X-ray spectrum and Compton backscatter in a coherent fashion. The results of this study are compared with observational data. Because of the large contribution from the backscatter, for an anisotropic primary X-ray source which is due to bremsstrahlung of accelerated electrons moving predominantly down towards the photosphere, the observed X-ray flux around 30 keV does not depend significantly on the position of flare on the sun. For such an anisotropic source, the X-ray spectrum observed in the 15 to 50 keV range becomes steeper with the increasing heliocentric angle of the flare. These results are compatible with the

data. The degree of polarization of the sum of the primary and reflected X-rays with energies between about 15 and 30 keV is very large for anisotropic primary X-ray sources, whereas it is less than about 4% for isotropic sources. We also discuss the characteristics of the brightness distribution of the X-ray albedo patch created by the Compton backscatter. The height and anisotropy of the primary hard X-ray source might be inferred from the study of the albedo patch.

Until recently observations and theoretical studies of solar hard X-rays have been limited to energies below about 300 keV. Observations of solar X-rays and gamma-rays from large flares such as the August 4, 1972 flare show that the hard X-ray spectrum extends into the gamma-ray region, where a flattening in the spectrum of the continuum emission is observed above about 1 MeV. This emission is believed to be due to bremsstrahlung. In addition to electron-proton collisions, at energies greater than $\sim$500 keV, bremsstrahlung due to electron-electron collisions becomes significant. The cross section for this process, applicable in the mildly relativistic region became available only recently. We provide a detailed calculation of bremsstrahlung production for a variety of electron spectra extending from the nonrelativistic region to relativistic energies and we take into account electron-electron bremsstrahlung. By comparing these calculations with data, we find that the flattening in the spectrum of the continuum emission from the August 4, 1972 flare can be best explained by an electron spectrum consisting of two distinctive components. This evidence, together with information on the X-ray and gamma-ray time profiles, implies the existence of two phases of acceleration. The first phase accelerates electrons mainly up to about several hundred keV; the second phase accelerates a small fraction of the electrons accelerated in the first phase to relativistic energies and accelerates protons to tens and hundreds of MeV.

ACKNOWLEDGMENTS

I am indebted to many people for the successful completion of my thesis.

First of all, it is my pleasure to thank Dr. Reuven Ramaty who has provided essential guidance and advice in all phases of the work. He has also provided considerate advice on matters other than physics. I also would like to thank Professor Frank B. McDonald for providing helpful advice and giving me a good opportunity to perform the research in the Laboratory for High Energy Astrophysics at the Goddard Space Flight Center. I also thank Dr. A. N. Suri for the gamma-ray work used in Chapter V prior to publication.

I would like to acknowledge Professor Klaus Pinkau for the hospitality shown during my stay from May to September, 1975 at the Max Planck Institute for Extraterrestrial Physics, Garching bei Munich, West Germany.

I thank Professor D. Wentzel for his comments which improved the thesis. Ms. Julia Saba's careful reading of a part of the thesis manuscript is also acknowledged. I also thank Messers. Adam Thompson, Frank Shaffer, Harry Trexel, and Larry White, for their excellent drawings for this thesis.

I thank my family in Korea for encouraging me continuously and having pride in my work--especially, Grandparents, Mother, Uncle Chong Chul Bai. Finally, but not least, I thank my wife Suin for her continuous encouragement and sacrifices made while assisting me in all phases of the work. The coincidence of the birth of our first child, Samuel, with the completion of my thesis must have given her extra difficulty.

Chapter Page

ACKNOWLEDGEMENTS . . . . . iii

LIST OF TABLES . . . . . vi

LIST OF FIGURES . . . . . vii

I. INTRODUCTION . . . . . 1

II. PRODUCTION MECHANISMS OF SOLAR FLARE PHOTONS IN THE 10 KEV TO 10 MEV RANGE . . . . . 8

A. Production Mechanisms other than Bremsstrahlung Photons from Accelerated Electrons . . . . . 9

1. Compton Scattering . . . . . 9

2. Bremsstrahlung due to Energetic Protons . . . . . 14

3. Gamma Rays due to Accelerated Nuclei . . . . . 16

B. Electron-Proton Bremsstrahlung . . . . . 17

C. Electron-Electron Bremsstrahlung . . . . . 26

D. Bremsstrahlung Rate due to Isotropic Electrons with Power Power-Law Spectra . . . . . 29

III. A COHERENT STUDY OF POLARIZATION, COMPTON BACKSCATTER, ANISOTROPY, AND ALBEDO PATCH OF SOLAR HARD X-RAYS . . . . . 40

A. Introduction . . . . . 40

B. Methods of Calculations . . . . . 44

1. The Stokes Parameters and the Matrix Representation of the Compton Scattering Cross Section . . . . . 44

2. Calculation of the Stokes Parameters of the Bremsstrahlung Hard X-Rays due to Anisotropic Electrons . . . . . 50

3. A Monte Carlo Simulation . . . . . 54

C. Backscatter, Anisotropy, and Spectral Characteristics of Solar Hard X-Rays . . . . . 57

1. General Properties of Backscatter . . . . . 57

2. The Albedo of Isotropic Sources . . . . . 60

3. Anisotropic Sources . . . . . 64

D. Compton Backscatter and Polarization . . . . . 75

E. Characteristics of the Albedo Patch . . . . . 79

F. Discussion and Summary . . . . . 93

Chapter Page

IV. DATA-ORIENTED DISCUSSIONS ON THE HEIGHT AND THE ANISOTROPY OF THE SOLAR HARD X-RAY SOURCE AND ON THE POLARIZATION OF SOLAR HARD X-RAYS. . . . . 96

A. Introduction . . . . . 96

B. Determination of the Height . . . . . 98

1. Sources at the Disk Center . . . . . 99

2. Sources away from the Disk Center . . . . . 103

3. Extended Sources . . . . . 105

C. Anisotropy of Solar X-Rays . . . . . 106

D. Discussion on Polarization Measurements . . . . . 109

V. X-AND GAMMA-RAY EVIDENCE FOR TWO PHASES OF ACCELERATION IN SOLAR FLARES . . . . . 112

A. Introduction . . . . . 112

B. The Energy Spectrum of the Accelerated Electrons . . . . . 114

C. Time Profiles of Radiation Intensities . . . . . 124

D. Summary and Conclusion . . . . . 130

VI. SUMMARY AND CONCLUSION . . . . . 134

APPENDIX A. THE ANGLE BETWEEN THE SCATTERING PLANE AND THE NORMAL PLANE OF THE SCATTERED PHOTON . . . . 138

APPENDIX B. MONTE CARLO METHODS . . . . . 139

APPENDIX C. THE REFLECTION PROBABILITY DUE TO A SINGLE SCATTERING. . . . . 141

REFERENCES. . . . . 142

## LIST OF TABLES


| Table | | Page |
|---|---|---|
| 2.1. | Electron-Electron Bremsstrahlung Cross Section ($cm^2$/MeV) . . . . . | 31 |
| 3.1. | Spectral Indexes of Photon Spectra in the Range from 15 keV to 50 keV . . . . . | 73 |
| 3.2. | Spectral Indexes of Photon Spectra in the Range from 100 to 300 keV for the Anisotropic Sources . . . . . | 74 |
| 5.1. | Prompt Gamma Ray Lines. . . . . | 117 |
| 5.2. | Atomic Abundances used for Gamma-Ray Calculations. . . . . | 118 |

LIST OF FIGURES


| Figure | | Page |
|---|---|---|
| 2.1. | Photon production rate due to inverse Compton scattering of accelerated electrons with the spectrum $E^{-2.5}$ with thermal photons of the sun and photon production rates due to bremsstrahlung of the same accelerated electrons in the medium of $n = 10^{10}$ $cm^{-3}$ and $10^9$ $cm^{-3}$, respectively | 12 |
| 2.2. | Angular dependence of the bremsstrahlung cross section for the electron energies, 30 keV, 50 keV, and 100 keV | 21 |
| 2.3. | Angular dependence of the bremsstrahlung cross section for the electron energies 500 keV and 1 MeV | 22 |
| 2.4. | Degree of polarization of bremsstrahlung | 25 |
| 2.5. | Electron-electron bremsstrahlung cross section integrated over the emission angle | 30 |
| 2.6. | Photon production rates due to e-p bremsstrahlung of accelerated electrons with power-law spectra | 34 |
| 2.7. | Photon production rates due to e-e bremsstrahlung of accelerated electrons with power-law spectra | 35 |
| 2.8. | Total photon production rates obtained by adding up the results of Figures 2.6 and 2.7 | 36 |
| 2.9. | Plot of $A_1(s)$, $\delta_1(s)$, $A_2(s)$, and $\delta_2(s)$ | 38 |
| 3.1. | Differential Compton cross section of unpolarized radiation, for several values of $\epsilon_0/mc^2$ | 49 |
| 3.2. | Photoelectric absorption cross section and total Compton cross section | 51 |
| 3.3. | Distribution of photons escaped from the photosphere as a function of the number of collisions | 58 |
| 3.4. | Distribution of photons escaped from the photosphere as a function of final energy | 59 |
| 3.5. | Integral reflectivities of isotropic X-ray sources | 62 |

Figure | Page

3.6. Differential reflectivities of isotropic sources with power-law spectra . . . . . 63

3.7. Photon spectra due to a thermal hydrogen plasma with $n_e = n_i = 1$ $cm^{-3}$, and kT = 20 keV and kT = 30 keV . . . . . 65

3.8. The degree of polarization of primary hard X-rays due to the accelerated electrons moving toward the photosphere with velocity vectors uniformly distributed in a cone with half opening angle 30° and centered at the vertical to the photosphere. The spectrum of the accelerated electrons is $E^{-2.5}$ . . . . . 67

3.9. Primary X-ray intensities due to the same electrons as in the above . . . . . 68

3.10. Same as Figure 3.8, except that the electron spectrum is $E^{-3.5}$ . . . . . 69

3.11. Same as Figure 3.9, except that the electron spectrum is $E^{-3.5}$ . . . . . 70

3.12. Photon spectra taken from the results of Figures 3.9 and 3.11; $\theta$ is the angle between the direction of observation and the normal to the photosphere . . . . . 72

3.13. Degree of polarization due to Compton backscatter of unpolarized isotropic primary photons . . . . . 77

3.14. Degree of polarization of photons due to anisotropic electrons, where the angular distribution of the electrons is

$$g(\theta) = \begin{cases} \text{const} & \text{for} \quad 150^\circ < \theta < 180^\circ \\ 0 & \text{for} \quad \theta < 150^\circ \end{cases}$$ . . . . . 78

3.15. The same as Figure 3.14, except that

$$g(\theta) = \begin{cases} \text{const} & \text{for} \quad 120^\circ < \theta < 180^\circ \\ 0 & \text{for} \quad \theta < 120^\circ \end{cases}$$ . . . . . 80

3.16. A schematic drawing of the geometry of the scattering . . . . . 81

3.17. The plotting of $f_1(\theta, \theta_o, \phi) = 1/(1 - \cos\theta_o/\cos\theta)$ and $f_2(\theta, \theta_o, \phi)$ $= \left(\frac{4\pi}{\sigma_T}\right)\frac{d\sigma_T}{d\Omega}(\theta_s(\theta, \theta_o, \phi))$ for $\phi = \frac{\pi}{2}$ . . . . . 85

Figure | Page


3.18. The differential reflectivity of an unpolarized beam as a function of the beam direction. It is measured in the interval from 16 to 22 keV, and the spectrum of the incident beam is $\epsilon^{-3}$ . . . . . 87

3.19. Same as the above Figure, except the energy interval is from 22 keV to 30 keV . . . . . 88

3.20. The differential reflectivity of a completely polarized beam as a function of the beam direction. The energy interval is from 16 to 22 keV, and the incident photon spectrum is $\epsilon^{-3}$. . . . . 89

3.21. Same as the above Figure, except that the energy interval is from 22 keV to 30 keV . . . . . 90

3.22. Isobrightness contours of the albedo patch for various cases. Starting from the center brightness drops by a factor 1/2 from one contour to the next . . . . . 92

4.1. Calculated albedo photon counts registered in the mpc's of the Hard X-ray Imaging Spectrometer, for an isotropic source at $\theta = 0°$ and h = d . . . . . 100

4.2. Calculated albedo photon counts, for an isotropic source at $\theta = 0°$ and h = 4d . . . . . 101

4.3. Calculated albedo photon counts, for an isotropic source at $\theta = 45°$ and h = 4d . . . . . 104

4.4. Calculated albedo photon counts, for an anisotropic, polarized source at $\theta = 45°$ and h = 4d . . . . . 106

4.5. The degree of polarization measured by Tindo and his coworkers v.s. heliocentric angle of the flare . . . . . 110

5.1. The observed hard X-ray and gamma-ray continuum from the 1972, August 4 flare . . . . . 115

5.2. The gamma-ray counts from the 1972, August 4 flare measured by the New Hampshire group and the calculated nuclear gamma-ray counts . . . . . 120

5.3. The gamma-ray counts from the August 4, 1972 flare and a theoretical fit to the data . . . . . 122

Figure Page

5.4. An electron spectrum which gives a best fit to the continuum data . . . . . 123

5.5. Time dependences of radiations of the 1972 August 4, flare . . . . . 125

5.6. Energy loss times, E/(dE/dt), of electrons and protons in the medium with $n = 7.1 \times 10^{10}$ $cm^{-3}$, B = 415 gauss, and $T = 4.5 \times 10^6$K . . . . . 129

5.7. Observed count rates for the 1972, August 4 flare . . . . . 131

# CHAPTER I

# INTRODUCTION

This thesis is concerned with the solar flare continuum radiation from 10 keV to 10 MeV. This continuum radiation is believed to be mainly due to bremsstrahlung of accelerated electrons, except for the MeV region where a part of the continuum is due to Doppler broadened nuclear gamma-ray lines. Therefore, the study of the flare continuum radiation from 10 keV to 10 MeV can give information on the accelerated particles in the flare region and on the properties of the emitting medium. Emphasis of the thesis is laid upon the two aspects of this continuum: the Compton backscatter of X-rays from the photosphere and related problems, and the properties of the continuum in the transition region from non-relativistic to relativistic energies.

Hard X-rays from a solar flare were first detected by Peterson and Winckler (1959) with a balloon-born detector at an atmospheric depth of 10 $g/cm^2$. Soon after that, solar hard X-rays were also detected by Chubb, Friedman, and Kreplin (1960) with a detector mounted on a rocket. However, the detection limitation due to the earth's atmosphere and the short exposure time available in rocket flights could be overcome only after hard X-ray detectors were flown on artificial satellites starting from the early 1960's (principally on the OSO and OGO series). In this introduction we summarize the pertinent observational characteristics of solar hard X-ray bursts, and we discuss the theoretical problems presented by these observations. We then describe the research done in each chapter of this thesis.

The observational characteristics of solar hard X-ray bursts, generally referring to small flares or subflares, have been analyzed in detail by Kane and Anderson (1970), Kane (1971, 1973, 1974), Peterson, Datlowe, and McKenzie (1973), and Datlowe, Elcan,

and Hudson (1974). They are summarized by Švestka (1976) as follows: (1) The hard X-ray burst occurs during the flash phase and peaks usually 0.5 to 3 minutes before the flare maximum observed in $H_\alpha$ light. (2) The increases and decreases of the X-ray flux at 40 keV are roughly exponential, with e-folding rise times of 2 to 5 seconds and similar or slightly longer e-folding decay times. For large flares, the X-ray time profile consists of many spikes of the order of one minute durations; short-lived spikes of the order of one second duration are superimposed on top of them (van Beek et al. 1973). (3) The peak X-ray flux at the earth, above 10 keV, is usually $10^{-7}$ to $10^{-5}$ erg $cm^{-2}$ $sec^{-1}$. (4) The X-ray spectrum is of the power-law form, $\frac{dq(\epsilon)}{d\epsilon} \sim \epsilon^{-\delta}$ (photons $cm^{-2}$ $sec^{-1}$ $keV^{-1}$), with $3.5 \lesssim \delta \lesssim 5.5$ (median $\delta \simeq 4.6$) in the range 10 keV to about 80 keV, at the maximum flux, and above about 80 keV the spectrum becomes much steeper. Spectral indexes larger than 7 are very rare and hard to determine because of the pileup effect (Datlowe et al. 1974), and they almost never become smaller than 2.5 (Kane 1974, Datlowe et al. 1974). (5) The spectrum is hardest near the flux maximum (Kane and Anderson 1970, Kane 1973).

Once measurements of the energy spectra of solar hard X-rays became available, it was possible to deduce the energy spectra of the accelerated electrons and to calculate the number and the energy content of the accelerated electrons (Lin and Hudson 1976). Electrons with power-law energy spectra can produce power-law photon spectra usually observed, and this fact was regarded as an evidence of the nonthermal origin of solar hard X-rays (Takakura and Kai 1966, Holt and Cline 1968, Holt and Ramaty 1969). However, power-law spectra of hard X-rays can also be due to a multi-temperature plasma (Chubb 1972, Milkey 1971). Because the thermal and nonthermal interpretations require

quite different flare models, it is very important to determine the nature of solar flare hard X-rays.

If solar hard X-rays are due to nonthermal electrons, these electrons are expected to be anisotropic. It was thought that, if there existed a prevailing direction of anisotropy, because of the directionality of bremsstrahlung, the frequency of occurrence of hard X-ray events above a certain threshold should depend on the solar longitude of the events. By analyzing the observational data, Ohki (1969), Pinter (1969), and Pizzichini et al. (1974) have studied the center-to-limb variation of the solar X-ray emission. The results, however, were contradictory and moreover the statistics were too low to draw a meaningful conclusion. Meanwhile, the angular dependence of the hard X-ray flux due to anisotropic electrons streaming down to the photosphere was calculated by Brown (1972) and by Petrosian (1973). These calculations predict that the observed X-ray flux will be larger for flares near the limb than for those near the disk center, and that the X-ray spectrum will be slightly flatter for limb flares. However, the limb brightening effect was not confirmed by the detailed analyses of Kane (1974) and Datlowe et al. (1974), who used OGO-5 data and OSO-7 data, respectively. Contrary to the prediction of these calculations, the result of Datlowe et al. (1974) showed that the average X-ray spectrum of limb flares is steeper than that of disk flares.

The anisotropy of accelerated electrons can also be studied by polarization measurements (Korchak 1967). Polarization measurements have been carried out mainly by Tindo and his coworkers (Tindo et al. 1970, 1972a, 1972b), and finite degrees of polarization have been reported. The degree of polarization of hard X-rays due to anisotropic accelerated electrons was calculated by Haug (1972) and by Brown (1972). Thus, on the one hand, the results of polarization measurements seem to support a nonthermal

interpretation and this interpretation is supported by studies of spectra and the time variations of X-rays. On the other hand, the lack of limb-brightening and limb-flattening effects seems to contradict the nonthermal interpretation. This apparent contradiction is resolved when the backscatter of X-rays described below is taken into account.

Tomblin (1972) and Santangelo, Horstman, and Horstman-Moretti (1973) showed that at energies above 15 keV a significant fraction of hard X-rays incident upon the photosphere is backscattered due to the Compton scattering process. Thus, for anisotropic models in which hard X-rays are predominantly emitted down toward the photosphere, the albedo X-rays constitute a large fraction of the observed hard X-ray flux. Furthermore, the Compton scattering cross section is dependent upon the polarization of the X-ray beam. Therefore, the study of the anisotropy of the accelerated electrons and the polarization of hard X-radiation should be studied together with the Compton backscatter. This fact has been realized only recently. Henoux (1975) briefly discussed the effects of the backscatter of hard X-rays on the directivity and polarization, and suggested that the apparent contradiction between the lack of limb brightening effect and the polarization measurements could be resolved by taking the Compton backscatter into account. In this thesis we perform a detailed calculation and confirm this result. We further investigate the effects of the backscatter on the spectrum of hard X-rays, and show that the limb steepening observed by Datlowe et al. (1974) is well explained by an anisotropic model when the backscatter is taken into account.

Another direction of solar hard X-ray research is the quest for good spatial resolution. The knowledge on the size and the shape of the hard X-ray emitting region is very important for the understanding of flare phenomena. Hard X-ray measurements with a very good spatial resolution not only can tell the size and shape of the emitting

region, but also can give information on the height and anisotropy of the primary X-ray source by resolving the photospheric albedo from the primary X-ray source (Brown, van Beek, and McClymont 1975). However, to evaluate the relationships among the height, the anisotropy and the albedo brightness distribution, a complete calculation of backscatter is required. So far the spatial resolution of hard X-ray emission has not been attempted except the one-dimensional scanning by Takakura et al. (1971). However, an X-ray detector with 8 arcsecond resolution will be flown on NASA's Solar Maximum Mission (SMM), and detectors with even better resolution might become available in the future.

The study of temporal variation of solar hard X-rays is also very important. Through such studies, we can learn about the characteristic time of X-ray emission, $\tau$, the characteristic acceleration time of electrons, $\tau_a$, the characteristic energy loss time, $\tau_i$, which is related to the ambient medium, and the characteristic escape time, $\tau_e$, which is chiefly related to the magnetic field configuration of the emitting region. Until recently, the temporal resolution was not so good, and theoretical discussions were mainly confined to arguing whether the interaction model of the accelerated electrons is thin-target ($\tau_e \ll \tau_i < \tau$) or thick-target ($\tau > \tau_e \gg \tau_i$) or the trap model ($\tau_e \gg \tau_i \gtrsim \tau$). Van Beek et al. (1973) have measured hard X-rays with a time resolution of 1.2 seconds for a long duration ($\sim 10^3$ seconds) during the August 4, 1972 flare. A theoretical study of the hard X-ray time profiles of this flare was performed by Brown and Hoyng (1975). However, a very large coronal magnetic trap geometry proposed by these authors for this flare is unrealistic. Thus, further studies of the X-ray time profiles are needed. On the experimental side, the detector being prepared by Frost (1976) for the SMM can provide very good time resolution down to $10^{-3}$ seconds.

Because of steep energy spectra, observations and theoretical studies of solar hard X-rays have been limited mainly to energies below 300 keV. However, from observations of flare-associated electrons with mildly relativistic and relativistic energies and from observations of type IV metric bursts believed to be due to relativistic electrons, we know that such electrons are accelerated in large flares. From radio observations Wild, Smerd, and Weiss (1963) and de Jager (1969) proposed that energetic particles in solar flares are produced in two steps of acceleration. As observational evidence for the two-step acceleration theory, Frost and Dennis (1971) presented their data of hard X-rays below 250 keV, which consisted of an impulsive X-ray burst with a steeper spectrum and a more gradual X-ray burst with a flatter spectrum which followed the former.

In the two-step acceleration theory, electrons with energies between ten to several hundred keV are accelerated in the first step, and electrons with relativistic energies and protons with energies greater than about 10 MeV are accelerated in the second step (e.g., de Jager 1969). Electrons accelerated in the second step will produce bremsstrahlung continuum extending to the MeV region. Through nuclear interactions, protons and heavy nuclei accelerated in the second step will produce gamma-ray lines and a continuum due to Doppler broadening of lines (Ramaty, Kozlovsky, and Lingenfelter 1975, Ramaty, Kozlovsky, and Suri 1977). Therefore, in order to investigate the numbers and spectra of the accelerated electrons, protons and heavy ions, it is necessary to extend the energy limit of the research on the flare radiation up to the MeV region. Among recent observations of gamma rays in this region (Gruber, Peterson, and Vette 1973, Chupp et al. 1973, Meliorensky et al. 1975), only Chupp et al. (1973) give a detailed spectrum and a time profile. The spectrum measured by the New Hampshire group (Chupp et al. 1973, Suri et al. 1975) shows a flattening at about 1 MeV, and a similar

feature could be also inferred from the other two measurements. In this thesis, by investigating in detail the spectral characteristics of the observed continuum up to 7 MeV and the characteristics of time profiles of X- and gamma-ray fluxes, we provide additional evidence for the two-step acceleration theory.

In Chapter II we discuss various radiation mechanisms of hard X-rays with emphasis on bremsstrahlung--especially on electron-electron bremsstrahlung, whose cross section in the mildly relativistic region became available only recently. The inclusion of electron-electron bremsstrahlung is essential for a full understanding of the photon spectrum in the transition band from the hard X-ray to gamma-ray region. In Chapter III the anisotropy, Compton backscatter of solar hard X-rays and related problems are investigated. Here we present a coherent study of the anisotropy, polarization, and backscatter. We discuss the effect of the backscatter on the characteristics of the X-ray spectrum, and we investigate the brightness distribution of the area from which X-rays are reflected. In Chapter IV we discuss how future observations with high spatial resolution could determine the relation between the height and anisotropy of the primary source and the albedo brightness distribution. In this chapter we also compare our results with observational data on polarization. In Chapter V, by investigating in detail the X- and gamma-ray continuum from 0.35 to 8 MeV and the X-ray time profiles of the August 4, 1972 flare, we provide evidence for two phases of acceleration. In Chapter VI we summarize our results.

# CHAPTER II

## PRODUCTION MECHANISMS OF SOLAR FLARE PHOTONS IN THE 10 KEV TO 10 MEV RANGE

Accelerated electrons with energy $\gtrsim$10 keV produce hard X-rays with energy $\gtrsim$10 keV. Accelerated protons and heavy nuclei produce narrow gamma ray lines in the MeV range and also gamma ray continuum in this range due to Doppler broadening of these lines (e.g., Ramaty, Kozlovsky, and Suri 1977). In addition, inverse Compton scattering of relativistic electrons with thermal solar photons (Shklovskii 1965) and bremsstrahlung due to collisions of accelerated protons with the ambient electrons (Boldt and Serlemitsos 1969) can produce hard X-rays.

In Section A we discuss briefly the relative importance of these radiation mechanisms in the solar flare, and show that inverse Compton scattering and bremsstrahlung due to energetic protons are not important under usual flare conditions. We also discuss in this section the gamma ray continuum due to accelerated ions. Then, we devote the rest of this Chapter to the discussion of bremsstrahlung of accelerated electrons. In Section B we review the various characteristics of bremsstrahlung due to collisions of accelerated electrons with the ambient ions. In Section C we discuss the characteristics of bremsstrahlung due to collisions of accelerated electrons with the ambient electrons. In Section D we provide calculations of bremsstrahlung production rates due to collisions of accelerated electrons with the ambient particles, by assuming that the momentum vectors of accelerated electrons are isotropically distributed, and that the energy spectra of the electrons are power laws. Such calculations can be used as a handy reference for quick estimations of the spectrum and the number of accelerated electrons in the flare region.

## A. Production Mechanisms other than Bremsstrahlung Photons from Accelerated Electrons

### 1. Compton Scattering

Relativistic electrons in the flare region make high energy photons by colliding with thermal photons flowing out of the sun's surface. Once this mechanism was proposed to be responsible for the production of hard X-rays from solar flares (Shklovskii 1965). In this subsection we discuss the relative importance of this mechanism in solar flares.

When an electron with total energy $\gamma mc^2$ collides with a photon of energy $\epsilon_0$, the resultant photon energy is (Felten and Morrison 1966)

$$\epsilon_1 = \gamma^2 \epsilon_0 (1 - \beta \cos \alpha_0)(1 + \beta \cos \alpha_1'), \tag{2.1}$$

where $\alpha_0$ is the angle between electron's direction of motion and the incident photon's direction of motion in the lab frame, and $\alpha_1'$ is the angle between the direction of incident electron and the direction of the outgoing photon in the electron's rest frame. For isotropically distributed photons, the average energy of the resultant photons is 4/3 $\gamma^2 \epsilon_0$. In a thermal photon field, the photon spectrum produced by inverse Compton scattering of accelerated electrons with a power-law spectrum,

$$N(E) = KE^{-s} \text{ (electrons/MeV)}, \tag{2.2}$$

is given by (Ginzburg and Syrovatskii 1964)

$$Q(\epsilon) = f(s) \cdot \frac{2}{3} c\, \sigma_T w_{ph} (mc^2)^{1-s} \left(\frac{4}{3}\bar{\epsilon}\right)^{\left(\frac{s-3}{2}\right)} K\epsilon^{-\frac{(s+1)}{2}} \text{ (photons/MeV/sec)}. \tag{2.3}$$

Here c is the speed of light, $\sigma_T$ is the Thompson cross section, $w_{ph}$ is the photon energy density, $mc^2$ is the electron rest mass energy, and $\bar{\epsilon} = 2.7$ kT is the mean photon

energy. The factor f(s) is of the order of unity, and in particular f(2) = 0.86, f(3) = 0.99 (Ginzburg and Syrovatskii 1964).

Because the average amplification factor of the photon energy due to inverse Compton scattering with an electron with energy $\gamma mc^2$ is $4/3\ \gamma^2$, we need much higher energy electrons in order to produce hard X-rays through inverse Compton scattering than through bremsstrahlung. Also the energy spectrum of the photons due to inverse Compton scattering is flatter than the spectrum of the bremsstrahlung photons. The spectral index of the former is $(s + 1)/2$, and the spectral index of the latter is about $s + 0.5$ (see Section II.D), where s is the spectral index of the accelerated electrons. Thus, the photon production due to inverse Compton scattering can be important if the energy spectrum of the accelerated electrons is relatively flat.

The energy spectrum of the flare-associated electrons has been reported for many solar events (Cline and McDonald 1968, Datlowe 1971, Datlowe et al. 1970, Sullivan 1970, Dillworth et al. 1972, Simnett 1972, 1973). In his review paper, Simnett (1974) reported that the spectral index of the electrons associated with visible flares ranges from 2.5 to 3 in the 0.3 to 12 MeV region, and it ranges from 2.5 to 4.5 in the 12 to 45 MeV region. He also reported that the spectrum sometimes steepens towards higher energies for events for which the energy spectra are measured in the both energy intervals.

Let us calculate the photon production rates due to inverse Compton scattering by relativistic electrons with a power index 2.5 and with no high energy cut off. Considering the observed electron spectra, this assumption for the electron spectrum is the most favorable assumption for X-ray production by inverse Compton scattering. Using T = 5800° K, $w_{ph} = 1.31 \times 10^6$ MeV/cm$^{-3}$ (Allen 1964), $\bar{\epsilon} = 2.7\ kT = 1.35 \times 10^{-6}$

MeV, and equation (2.3), we get the following formula for photon production rate due to inverse Compton scattering

$$Q(\epsilon) = 3.18 \times 10^{-4}\, \epsilon^{-1.75} \text{ (photons/MeV/sec)} \tag{2.4}$$

for an electron spectrum $N(E) = 2.64 \times 10^2\, E^{-2.5}$ ($N(>30 \text{ MeV}) = 1$), where $\epsilon$ and E are in units of MeV. This equation is plotted in Figure 2.1, as a solid line. Bremsstrahlung production rates by the same accelerated electrons are shown by two dashed lines, for ambient densities $n = 10^{10}\ \text{cm}^{-3}$ and $n = 10^9\ \text{cm}^{-3}$, respectively. The figure shows that the photon production rate due to inverse Compton scattering may be non-negligible at high photon energies, if the electron spectrum is flat ($s \lesssim 2.5$) up to the several hundred MeV region and $n \ll 10^{10}\ \text{cm}^{-3}$.

Observational data on the electron spectrum above 45 MeV are not available. However, for the following reasons, it is very unlikely that the electron spectrum in the flare region is as flat as $s = 2.5$ up to the several hundred MeV region. First, severe synchrotron energy loss rate of high energy electrons will steepen the spectrum at higher energies. Second, considering the short flare time ($\lesssim$1000 seconds) and the small dimension of the flare region, we can hardly expect that electrons are accelerated efficiently up to several hundreds of MeV. (However, protons are accelerated up to these energies. See Chapter V for particle acceleration.) Third, the observational data available up to 45 MeV show a trend of steepening of the spectrum toward higher energies (Simnett 1974).

In addition to the likely steepening of the electron spectrum at higher energies, the following two effects also reduce the photon production rate due to inverse Compton scattering. Since electrons which make X-rays through inverse Compton scattering

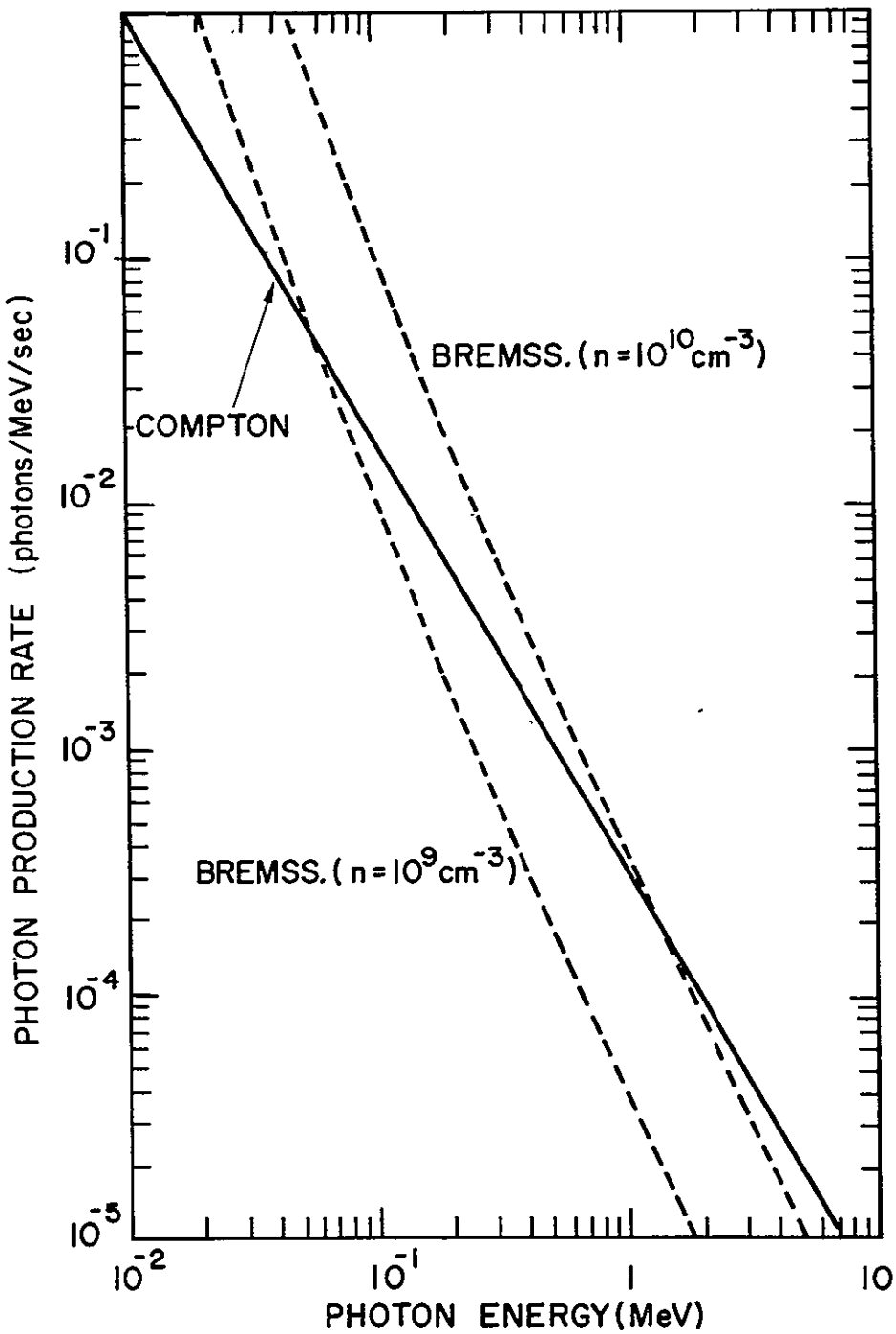


Figure 2.1. Photon production rate due to inverse Compton scattering of accelerated electrons with the spectrum $E^{-2.5}$ with thermal photons of the sun and photon production rates due to bremsstrahlung of the same accelerated electrons in the medium of $n = 10^{10}$ cm$^{-3}$ and $10^{9}$ cm$^{-3}$, respectively.

have very high energies, even though the scattered photons are emitted almost isotropically in the electron's rest frame, in the lab frame almost all the scattered photons are well collimated in a very small cone around the electron's direction of motion. Therefore, photons are observable only if they are scattered by electrons moving toward the observer. Near the solar surface the photon field is not isotropic; in fact most of the photons come outward from the sun, so that those electrons moving toward the observer collide with red-shifted photons (corresponding to small values of $\alpha_o$ in equation 2.1). Consequently, the average energy of the photons scattered by an electron moving toward an observer away from the sun is less than the average energy of the photons scattered by an electron with the same energy in an isotropic field. Since the number of electrons decreases as energy increases, this means that for disk flares the photon intensity due to Compton scattering is lower than that obtained for an isotropic photon field.

Furthermore, the collision frequency is expressed by (Feenberg and Primakoff 1948)

$$\frac{dNcol}{dt} = c\int d\Omega\, n(\theta, \phi)\,(1 - \beta \cos \theta) \tag{2.5}$$

where $n(\theta, \phi)$ is the angular distribution function of the photons, and $\theta$ is the angle between the electron's direction of motion and that of the photon. Thus the scattering frequency is also lower in solar flares than in an isotropic photon field. These two effects are more pronounced for flares near the disk center.

We may conclude as follows. The photon production due to inverse Compton scattering may be important at high energies, if the electron spectrum is very flat ($s \lesssim 2.5$) up to several hundred MeV and the ambient density is not too high ($\ll 10^{10}$ cm$^{-3}$). Expected steepening of the electron spectrum at higher energies and the anisotropic

distribution of thermal photons from the sun's surface, however, make the photon production due to inverse Compton scattering less important. Furthermore, because the ambient density deduced by various methods is considerably larger than $10^{10}$ $cm^{-3}$ (e.g., Chapter V), the importance of the inverse Compton radiation in flares is further reduced. Under the usual flare conditions, therefore, the photon production due to inverse Compton scattering is most likely to be negligible. This is particularly certain for photon energies below 100 keV.

2. Bremsstrahlung due to Energetic Protons

Energetic protons make hard X-rays by colliding with the ambient thermal electrons. This mechanism was once suggested to be responsible for the production of hard X-rays from flares (Boldt and Serlemitsos 1969). Because an estimation of the number and spectrum of the accelerated protons in the flare region is available for the first time from the gamma ray data of the August 4, 1972 flare, we can discuss the relative importance of this mechanism for producing solar hard X-rays with more confidence.

In the proton's rest frame, ambient thermal electrons approach the proton with approximately the same velocity as the proton's velocity in the laboratory system, and are scattered by the stationary proton, giving rise to bremsstrahlung. For nonrelativistic protons, the transformation of the coordinate system back into the laboratory system does not significantly alter the radiation pattern in the proton's rest frame. Therefore, the instantaneous photon production rate and energy spectrum due to a nonrelativistic proton in a hydrogen plasma are the same as those of an electron with the same velocity in the same plasma. Thus, the instantaneous photon production rate and energy spectrum due to accelerated protons with a given velocity spectrum is

the same as those due to accelerated electrons with the same velocity spectrum. If the energy spectrum of accelerated protons is given by

$$N_p(E) = K\,E^{-s} \text{ (protons/MeV) for } E_1 < E < E_2, \tag{2.6}$$

the electron spectrum equivalent to this proton spectrum, in terms of instantaneous bremsstrahlung rate, is just

$$N_e(E) = \left(\frac{m}{M}\right)^s \cdot K\,E^{-s} \text{ (electrons/MeV) for } \frac{m}{M}E_1 < E < \frac{m}{M}E_2, \tag{2.7}$$

where m is the electron mass, and M is the proton mass.

The proton spectrum deduced from the gamma ray line data of Chupp et al. (1973) for the August 4, 1972 flare is given by (Ramaty, Kozlovsky and Lingenfelter 1975)

$$n\,N_p(E) = 1.6 \times 10^{45}\,E^{-2} \text{ (protons/MeV/cm}^3\text{) for 10 MeV} \lesssim E \lesssim \text{200 MeV.} \tag{2.8}$$

The equivalent electron spectrum in terms of the instantaneous bremsstrahlung rate is

$$n\,N_e(E) = 4.75 \times 10^{38}\,E^{-2} \text{ (electrons/MeV/cm}^3\text{) for 5 keV} \lesssim E \lesssim \text{100 keV.} \tag{2.9}$$

The photon intensity at 1 AU due to this spectrum can be obtained from the results in Section II. D:

$$Q(\epsilon) \simeq 2.2 \times 10^{-5}\,\epsilon^{-2.3} \text{(photons/sec/cm}^2\text{/MeV)}, \tag{2.10}$$

where $\epsilon$ is in units of MeV. This intensity is five or six orders of magnitude below the intensity observed from this flare in the 10 to 100 keV range.

Considering that the interplanetary proton flux (above 20 MeV) associated with the August 4, 1972 flare is among the largest (McDonald, Fichtel, and Fisk 1974),

bremsstrahlung due to collisions of accelerated protons with the ambient electrons must be negligible in all flares.

3. Gamma Rays due to Accelerated Nuclei

Ambient heavy nuclei are excited by collisions with accelerated protons and alpha particles in the flare region, and accelerated heavy nuclei in the flare region are excited by collision with ambient protons and alpha particles. Deexcitation of these nuclei generates nuclear gamma rays in the MeV range (e.g., Ramaty et al. 1975). The former process makes narrow lines with widths of about 100 keV. The latter process makes broad lines (with widths of about 1 MeV) due to the Doppler broadening, because excited nuclei in this process emerges with large velocities, comparable to their initial velocities. In addition to nuclear lines, neutrons produced by collisions of accelerated nuclei generate a 2.2-MeV line by deuteron formation, and positrons produced by collisions of accelerated nuclei give rise to a 0.51 MeV line through pair annihilation. The study of gamma ray lines can provide information on the accelerated nuclei which produce them. Solar gamma rays have been studied mainly by Ramaty, Lingenfelter, and coworkers (Ramaty et al. 1975 and references therein). Solar gamma rays have been positively detected for the first time by Chupp et al. (1973) for the August 4, 1972 flare.

Because the widths of the gamma ray lines due to collisions of accelerated nuclei with ambient protons and alpha particles are about 1 MeV, they overlap each other, and can no longer be called lines. Instead they form a gamma ray continuum in the MeV region, whose highly structured shape can be distinguished from a bremsstrahlung continuum by measurements with high energy resolution. According to Ramaty et al. (1977), the gamma ray continuum from 4 to 8 MeV for the August 4, 1972 flare could

be entirely due to Doppler-broadened nuclear lines. A detailed study of this continuum is provided in Chapter V.

## B. Electron-Proton Bremsstrahlung

So far we have discussed various hard X-ray production mechanisms in solar flares. We have found that below the MeV region bremsstrahlung of accelerated electrons is the important radiation mechanism. Let us discuss this mechanism in detail.

Bremsstrahlung cross-section formulas and related data have been extensively reviewed by Koch and Motz (1959). An "exact" expression for the bremsstrahlung cross section cannot be obtained, primarily because, to be exact, an electron should be represented by an infinite series of wave functions. However, many authors have tried to obtain bremsstrahlung cross-section formulas by using various approximate wave functions.

Among these formulas, those calculated by the Born-approximation procedure are available in relatively simple analytical forms, and their accuracy is good in the wide energy range of interest (10 keV ~ 10 MeV). In general, the Born-approximation theory becomes less reliable as (a) the atomic number of the target increases, (b) the initial electron energy decreases, and (c) the photon energy approaches the high-frequency limit (Koch and Motz 1959). However, the above conditions are not very relevant to our calculations of the production rates of solar hard X-rays for the following reasons: (a) in the solar atmosphere bremsstrahlung is almost entirely due to hydrogen and helium nuclei, (b) we are interested in electrons with energies $\gtrsim$10 keV, and (c) the inaccuracy of the Born-approximation formulas at the high-frequency limit is not pronounced for targets with low atomic numbers. Therefore, the Born-approximated formulas are expected to be reasonably accurate for our purpose.

A Born-approximated bremsstrahlung formula differential in photon energy and angle is given by (Koch and Motz 1959; Formula 2BN; Bethe and Heitler 1934)

$$\frac{d^2\sigma}{d\epsilon d\Omega}(E, \epsilon, \theta) = \frac{Z^2}{8\pi}\frac{r_o^2}{137}\frac{p'}{p}\frac{1}{\epsilon}\left\{\frac{8\sin^2\theta(2\gamma^2+1)}{p^2\Delta^4}\right.$$

$$-\frac{2(5\gamma^2+2\gamma\gamma'+3)}{p^2\Delta^2}-\frac{2(p^2-k^2)}{Q^2\Delta^2}+\frac{4\gamma'}{p^2\Delta}$$

$$+\frac{L}{pp'}\left[\frac{4\gamma\sin^2\theta(3k-p^2\gamma')}{p^2\Delta^4}+\frac{4\gamma^2(\gamma^2+\gamma'^2)}{p^2\Delta^2}\right. \tag{2.11}$$

$$\left.+\frac{2-2(7\gamma^2-3\gamma\gamma'+\gamma'^2)}{p^2\Delta^2}+\frac{2k(\gamma^2+\gamma\gamma'-1)}{p^2\Delta}\right]$$

$$\left.-\left(\frac{4\ell}{p'\Delta}\right)+\frac{\ell_0}{pQ}\left[\frac{4}{\Delta^2}-\frac{6k}{\Delta}-\frac{2k(p^2-k^2)}{Q^2\Delta}\right]\right\}.$$

Here E is the kinetic energy of the incident electron, $\epsilon$ is the photon energy, $\theta$ is the photon angle with respect to the momentum vector of the incident electron, Z is the atomic number of the target, and $r_o = 2.82 \times 10^{-13}$ cm. Other symbols are defined as follows:

$$\gamma = E/mc^2 + 1;\ \gamma' = \gamma - \epsilon/mc^2;\ k = \epsilon/mc^2;\ p = (\gamma^2 - 1)^{1/2}$$

$$p' = (\gamma'^2 - 1)^{1/2};\ L = 2\cdot\ell n\left(\frac{\gamma\gamma' + pp' - 1}{k}\right);\ \ell = \ell n\left(\frac{\gamma + p}{\gamma - p}\right); \tag{2.12}$$

$$\ell_o = \ell n\left(\frac{Q+p}{Q-p}\right);\ Q^2 = p^2 + k^2 - 2pk\cos\theta;\ \Delta = \gamma - p\cos\theta.$$

The integration of equation (2.11) over the photon angle gives rise to the bremsstrahlung cross-section formula differential in photon energy (Koch and Motz 1959; Equation 3BN),

$$\frac{d\sigma}{d\epsilon}(E, \epsilon) = \frac{Z^2 r_0^2}{137} \frac{p'}{p} \frac{1}{\epsilon} \left\{ \frac{4}{3} - 2\gamma\gamma' \left( \frac{p^2 + p'^2}{p^2 p'^2} \right) + \frac{\ell\gamma'}{p^3} \right.$$

$$+ \frac{\ell'\gamma}{p'^3} - \frac{\ell\ell'}{pp'} + L \left[ \frac{8\,\gamma\gamma'}{3\,pp'} + \frac{k^2(\gamma^2\gamma'^2 + p^2 p'^2)}{p^3 p'^3} \right. \tag{2.13}$$

$$\left. \left. + \frac{k}{2pp'} \left( \ell \frac{\gamma\gamma' + p^2}{p^3} - \ell' \frac{\gamma\gamma' + p^2}{p'^3} + \frac{2k\gamma\gamma'}{p^2 p'^2} \right) \right] \right\}$$

where $\ell' = \ell n \left( \frac{\gamma' + p'}{\gamma' - p'} \right)$, and all other symbols are the same as above in equation (2.12). For energies below 2 MeV, as a Coulomb correction factor, equation (2.13) is multiplied by the Elwert factor, $f_E$, (Koch and Motz 1959; Equation II-6)

$$f_E = \frac{\beta[1 - \exp\{-2\pi/(137\beta)\}]}{\beta'[1 - \exp\{-2\pi/(137\beta')\}]} \tag{2.14}$$

where $\beta' = (\gamma'^2 - 1)^{1/2}/\gamma'$. A Coulomb correction factor is not applied to equation (2.11) because a detailed angle-dependent Coulomb correction factor is not available. Equations (2.11) and (2.13) are for non-screened targets. Because the medium of the emitting region in the flare is believed to be almost completely ionized, the screening due to atomic electrons is negligible. Therefore, we use the nonscreened formulas.

The accuracy of equation (2.13) with the Elwert factor applied is within 5% below 100 keV, within 10% above 2 MeV, and within a factor of two between these energies (Koch and Motz 1959). The inaccuracy between 100 keV and 2 MeV, however, is large only when the atomic number of the target is large; and even when Z = 13, equation (2.13) with the Elwert factor applied is correct within 35% at worst. Therefore, in

the solar atmosphere where most of the targets are hydrogen and helium nuclei, we expect the above Born-approximated formulas to be reasonably accurate.

Radiation by a high-velocity electron is directional. In the rest frame of the incident electron, the rest electron is accelerated by the nucleus approaching with the electron's velocity in the laboratory frame. In the electron's initial rest frame, the motion of the electron after the collision is nonrelativistic except for very close collisions; therefore, the radiation power has the classical distribution proportional to $\sin^2 \Theta$, where $\Theta$, is the angle measured relative to the direction of acceleration. Because of the Doppler effect, in the lab frame the photons in the forward directions become more energetic than the photons in the backward directions, and more photons are emitted in the forward directions. When the electron is relativistic, the number of emitted photons peaks at $\theta = 0°$ and decreases with increasing $\theta$, and most of the photons are emitted with angles $\theta \lesssim 1/\gamma$ radians. Here $\theta$ is the angle measured from the electron's momentum vector (Jackson 1962). Therefore, the faster the electron is, the more directional its radiation becomes. The angular dependence of the bremsstrahlung cross section is plotted in Figures 2.2 and 2.3 for several values of electron energy and photon energy. (For more drawings of the angular dependence of the bremsstrahlung cross section, see Koch and Motz (1959) and Petrosian (1973).) The anisotropy problems of the radiation by accelerated electrons will be discussed in detail in Chapters III and IV.

Bremsstrahlung by an electron is polarized. In radiation problems, it is usual that the incident direction of the electron and the direction of the outgoing photon are known, but the deflected electron's direction is not known. Consequently the radiation plane which is defined by these first two directions, is a natural reference plane with respect to which one specifies the state of polarization. Because of the symmetry with

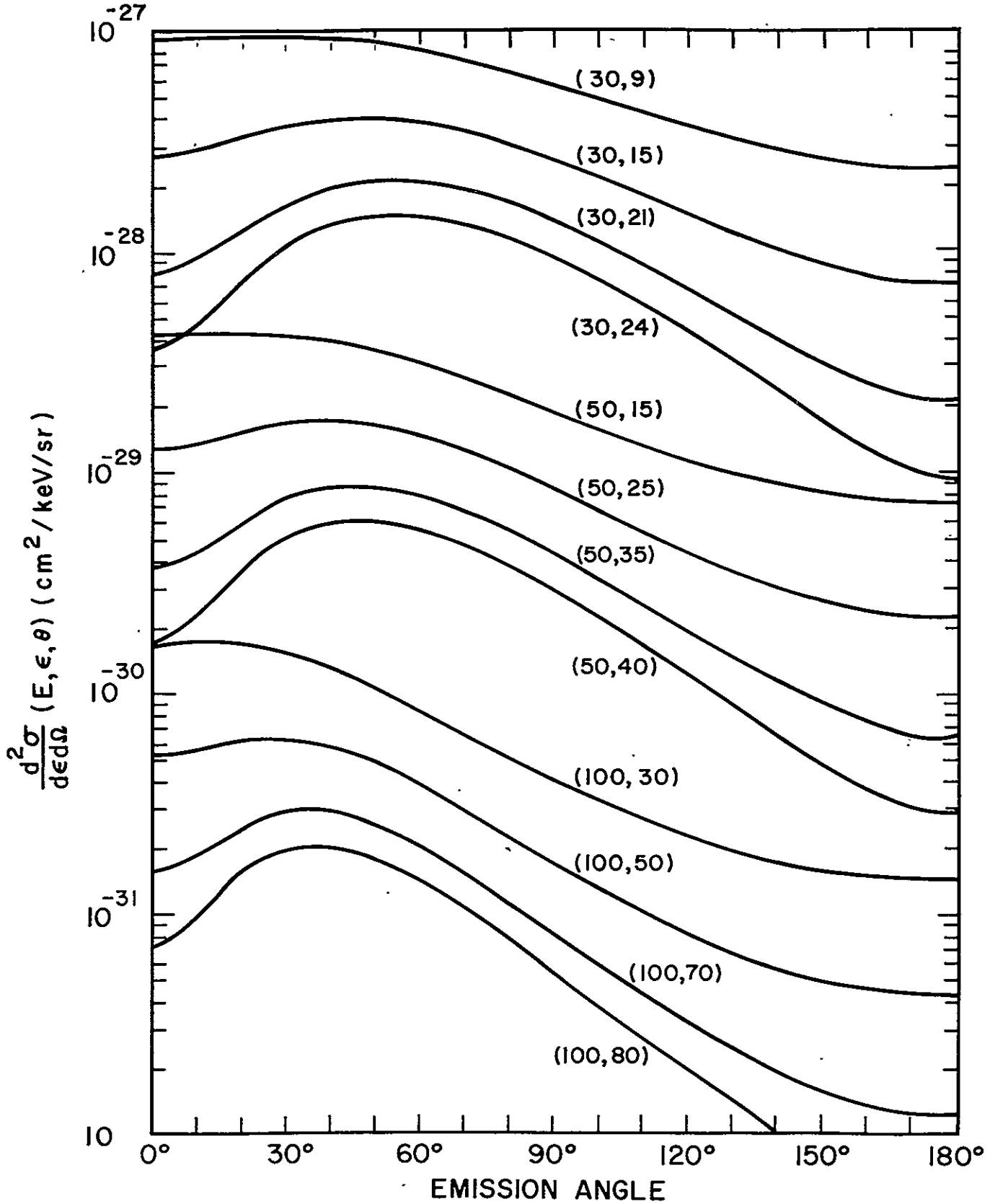


Figure 2.2. Angular dependence of the bremsstrahlung cross section for the electron energies, 30 keV, 50 keV, and 100 keV.

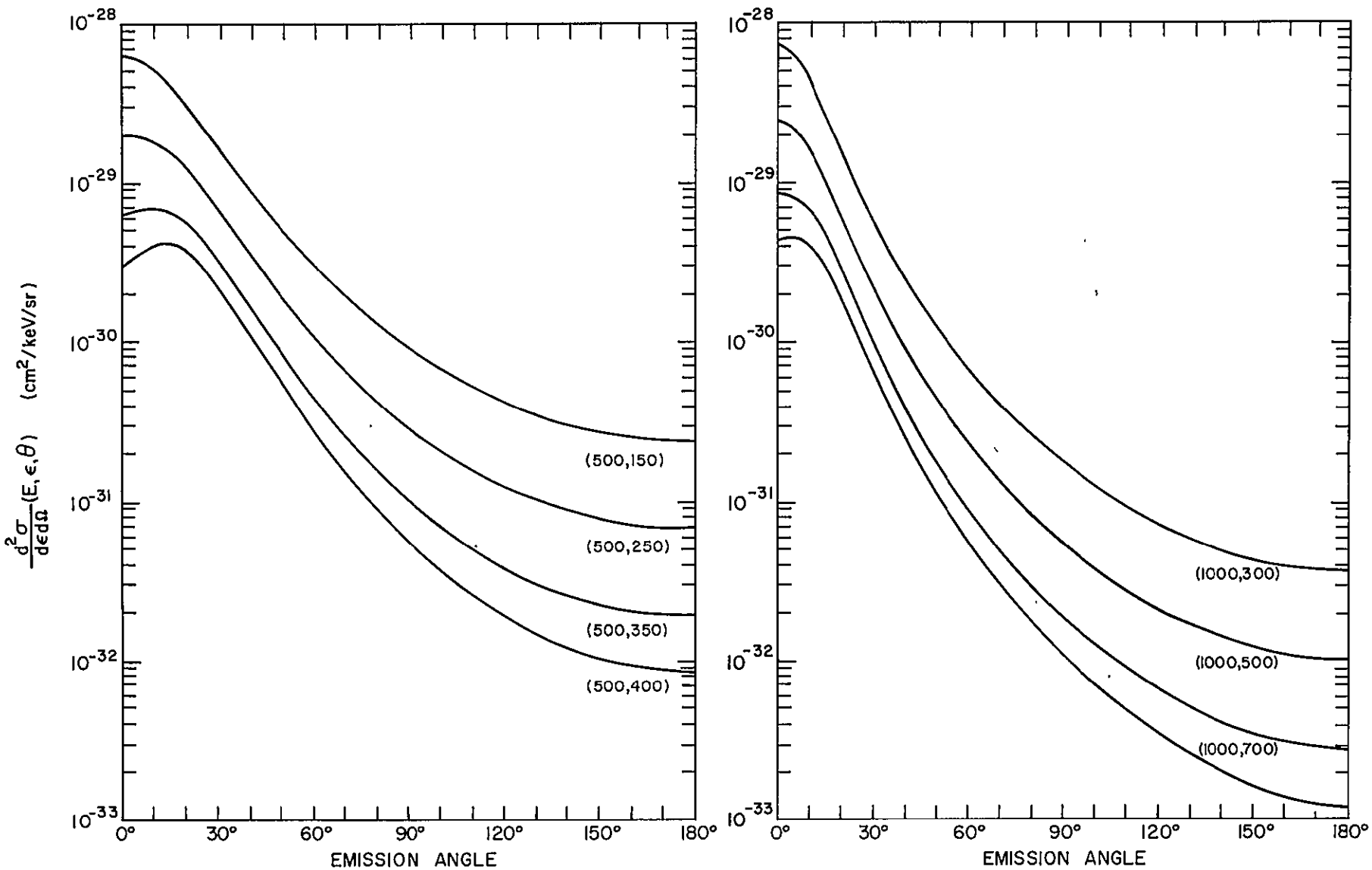


Figure 2.3. Angular dependence of the bremsstrahlung cross section for the electron energies 500 keV and 1 MeV.

respect to the radiation plane, the possibility of elliptical polarization of the bremsstrahlung by an unpolarized beam of electrons is ruled out (Gluckstern and Hull 1953, McMaster 1961).

Formulas for the polarization-dependent bremsstrahlung cross section were derived by various authors (Heitler 1933, Heitler 1949, Bethe and Heitler 1934, May 1951). Of these, the cross-section formulas of Gluckstern and Hull (1953) are accurate in the wide energy range. The bremsstrahlung cross sections for polarization perpendicular and parallel to the radiation plane are given by (Gluckstern and Hull 1953)

$$\begin{aligned}\frac{d^2\sigma_\perp(E,\epsilon,\theta)}{d\epsilon d\Omega} = \frac{Z^2}{8\pi}\frac{r_o^2}{137}\frac{p'}{p}\frac{1}{\epsilon}\Bigg\{&\frac{-(5\gamma+2\gamma\gamma'+1)}{p^2\Delta^2} - \frac{(p^2-k^2)}{Q^2\Delta^2} \\ &- \frac{2k}{p^2\Delta} + \frac{L}{pp'}\Bigg[\frac{2\gamma^2(\gamma^2+\gamma'^2)-(5\gamma-2\gamma\gamma'+\gamma'^2)}{p^2\Delta^2} \\ &+ \frac{k(\gamma^2+\gamma\gamma'-2)}{p^2\Delta}\Bigg] + \frac{\ell o}{p'Q}\left[\frac{k}{\Delta} - \frac{k(p^2-k^2)}{Q^2\Delta} + 4\right] \\ &- \frac{1}{p^2\sin^2\theta}\Bigg[\frac{2L}{pp'}\left(2\gamma^2-\gamma\gamma'-1-\frac{k}{\Delta}\right) \\ &- \frac{4\ell o}{p'Q}(\Delta-\gamma')^2 - \frac{2\ell(\Delta-\gamma')}{p'}\Bigg]\Bigg\}\end{aligned} \tag{2.15}$$

$$\begin{aligned}\frac{d^2\sigma_\parallel(E,\epsilon,\theta)}{d\epsilon d\Omega} = \frac{Z^2}{8\pi}\frac{r_o^2}{137}\frac{p'}{p}\frac{1}{\epsilon}\Bigg\{&\frac{8\sin^2\theta(2\gamma^2+1)}{p^2\Delta^4} - \frac{(5\gamma^2+2\gamma\gamma'+5)}{p^2\Delta^2} \\ &- \frac{(p^2-k^2)}{Q^2\Delta^2} + \frac{2(\gamma+\gamma')}{p^2\Delta} + \frac{L}{pp'}\Bigg[\frac{4\gamma\sin^2\theta(3k-p^2\gamma')}{p^2\Delta^4}\end{aligned} \tag{2.16}$$

$$+\frac{2\gamma^2(\gamma^2+\gamma'^2)-(9\gamma^2-4\gamma\gamma'+\gamma'^2)+2}{p^2\Delta^2}+\frac{k(\gamma^2+\gamma\gamma')}{p^2\Delta}\Bigg]$$

$$+\frac{\ell_o}{p'Q}\left[\frac{4}{\Delta^2}-\frac{7k}{\Delta}-\frac{k(p^2-k^2)}{Q^2\Delta}-4\right]-\frac{4\ell}{p'\Delta}$$

$$+\frac{1}{p^2\sin^2\theta}\left[\frac{2L}{pp'}\left(2\gamma^2-\gamma\gamma'-1-\frac{k}{\Delta}\right)\right.$$

$$\left.\left.-\frac{4\ell_o}{p'Q}(\Delta-\gamma')^2-\frac{2\ell(\Delta-\gamma')}{p'}\right]\right\}.$$

The notation here is the same as in equations (2.11) and (2.12). Notice the sum of these two equations are the same as equation (2.11). The minus sign indicated by an arrow in equation (2.15) was misprinted as a multiplication sign in Gluckstern and Hull (1953). (Gluckstern 1977, private communication.)

The degree of polarization is defined as

$$P_1(E,\epsilon,\theta)=\left[\frac{d^2\sigma_\perp(E,\epsilon,\theta)}{d\epsilon d\Omega}-\frac{d^2\sigma_\parallel(E,\epsilon,\theta)}{d\epsilon d\Omega}\right]\Bigg/\frac{d^2\sigma(E,\epsilon,\theta)}{d\epsilon d\Omega} \tag{2.17}$$

Because of the term containing the factor $1/(p^2\sin^2\theta)$, the above three equations are not valid when $\theta$ is very close to zero. However, $P_1$ approaches asymptotically to zero as $|\cos\theta|$ approaches to 1 until $(1-|\cos\theta|)\approx 10^{-3}\times(\gamma-1)^{-1}$; over this limit $P_1$ may be regarded to be zero. The degree of polarization defined by the above equation is plotted in Figure 2.4 for various electron energies and photon energies. As the figure shows, for $\epsilon/E \ll 1$ the polarization is perpendicular to the radiation plane, and for $\epsilon/E \lesssim 1$ the polarization is parallel to the radiation plane. For a beam of electrons with a steep energy spectrum, therefore, the polarization of the bremsstrahlung must be parallel to

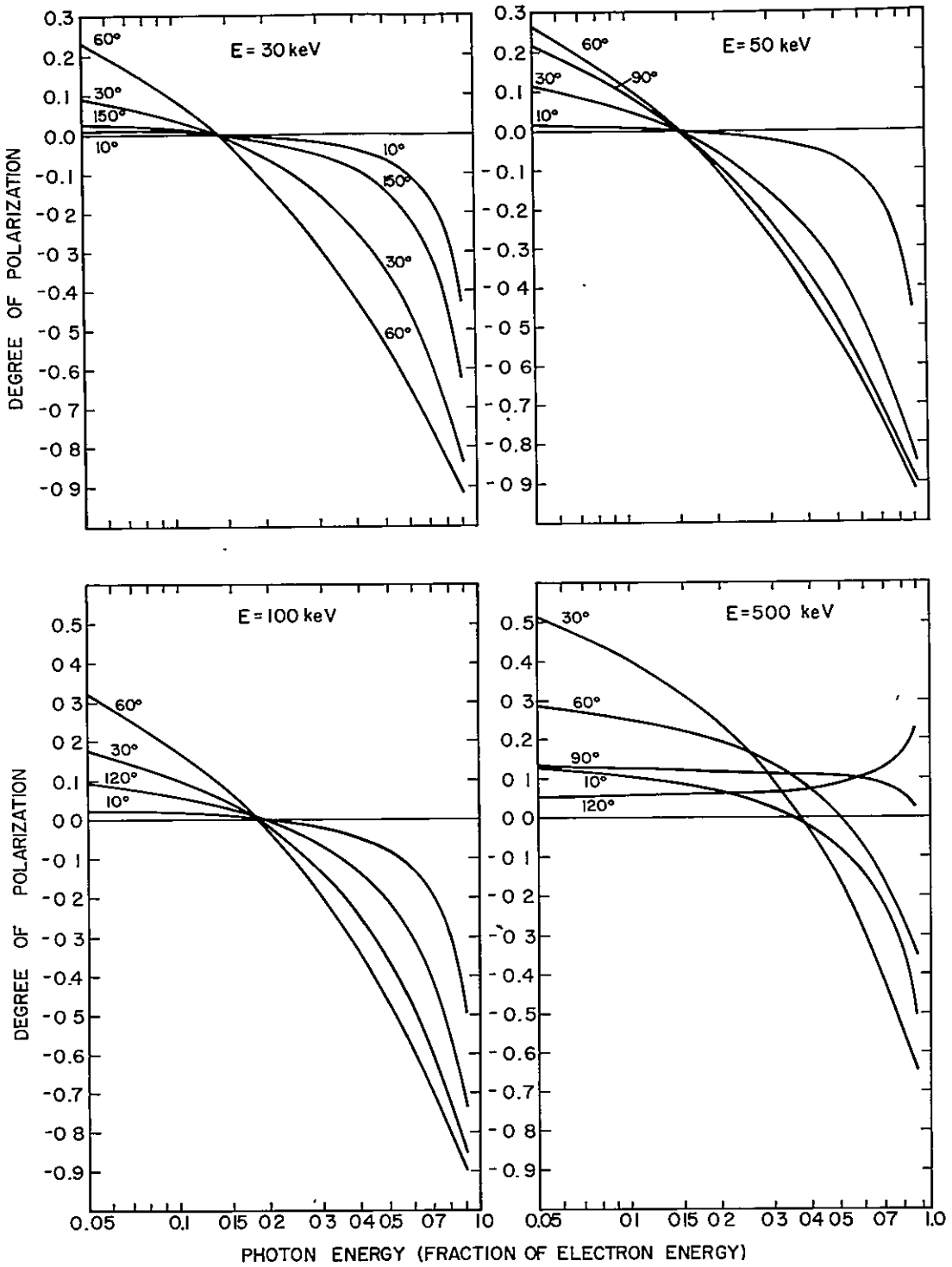


Figure 2.4. Degree of polarization of bremsstrahlung. The negative sign means the polarization parallel to the radiation plane, and the positive sign, perpendicular.

the radiation plane. A more detailed discussion of the polarization of bremsstrahlung hard X-rays is given in Chapters III and IV.

### C. Electron-Electron Bremsstrahlung

Bremsstrahlung is also produced in collisions of energetic electrons with the ambient electrons. For low electron energies the electron-electron quadrupole emission is negligible in comparison with the electron-proton dipole emission. However, as the kinetic energy of the electron approaches its rest mass energy, electron-electron bremsstrahlung (hereafter it will be abbreviated as "e-e bremsstrahlung") begins to be comparable to electron-proton bremsstrahlung ("e-p bremsstrahlung") (Maxon and Corman 1967, Akhiezer and Berestetskii 1965). Compared with the e-p bremsstrahlung processes, the e-e bremsstrahlung processes are extremely complicated because of recoil and exchange effects. Therefore, even though the e-e bremsstrahlung cross section differential in emission angle and in outgoing electron direction was first calculated by Hodes (1953) using lowest-order perturbation theory, a manageable form for the e-e bremsstrahlung cross section was not available until recently, except in the nonrelativistic and the extreme-relativistic limits (see Haug 1975 and references therein). In the mildly relativistic region, either the interpolation of the cross sections at these two extreme limits was used (Takakura 1967), or other assumptions were made (e.g., Bai and Ramaty 1976).

Until recently, solar hard X-rays have been observed mostly at energies below a few hundred keV where e-e bremsstrahlung can be neglected without a large error. The observation of the considerable flux of continuum radiation up to $\sim$7 MeV from the 1972 August 4 flare (Chupp et al. 1973) and the theoretical study of the observed continuum radiation (Bai and Ramaty 1976), however, showed us that the e-e bremsstrahlung contribution is not negligible.

Recently Haug (1975) has published a manageable formula for the bremsstrahlung cross section in the field of an electron. It was obtained by integrating analytically the differential cross section (Hodes 1953) over the angles of the outgoing electrons, without any approximations. The e-e bremsstrahlung cross section differential with respect to the photon energy and photon angles is given by (Haug 1975)

$$\frac{d^2\sigma_e}{d\epsilon d\Omega}(E, \epsilon, \theta) = \frac{r_o^2}{137\pi} \times \frac{\epsilon}{w\rho} \sqrt{\frac{\rho^2 - 4}{w^2 - 4}} \frac{1}{\pi} \int A d\Omega p_1' . \tag{2.18}$$

Here

$$w^2 = (\overline{p}_1 + \overline{p}_2)^2 , \tag{2.19}$$

and

$$\rho^2 = (\overline{p}_1' + \overline{p}_2')^2 , \tag{2.20}$$

where $\overline{p}_1$ and $\overline{p}_2$ represent the four-momenta of the two electrons before the collision, and $\overline{p}_1'$ and $\overline{p}_2'$, after the collision. The lengthy expression for $[(\rho^2 - 4)^{1/2}/\pi] \times \int A d\Omega p_1'$ is given in the Appendix of Haug (1975).

In the laboratory frame where one of the electron is at rest, equations (2.19) and (2.20) become

$$w^2 = 2(\gamma + 1), \tag{2.21}$$

$$\rho^2 = 2[\gamma + 1 - \epsilon/mc^2 \times (\gamma + 1 - p \cos\theta)] , \tag{2.22}$$

with notation as above. From equation (2.20), we see that the maximum photon energy occurs when $\rho^2 = 4$ and is given by

$$\epsilon_{max}(\gamma, \theta) = (\gamma - 1)mc^2/(\gamma + 1 - p\cos\theta). \tag{2.23}$$

The absolute maximum of $\epsilon$ occurs for the forward direction $\theta = 0°$,

$$\bar{\epsilon}_{max}(\gamma) = (\gamma - 1)mc^2/(\gamma + 1 - p) = E/(1 + \gamma - \sqrt{\gamma^2 - 1}). \tag{2.24}$$

As this equation shows, the ratio $\epsilon_{max}/E$ is a monotonically increasing function of E, approaching asymptotically to 1/2 as E becomes much less than $mc^2$ and to 1 as E becomes much larger than $mc^2$. In e-p bremsstrahlung, on the other hand, this ratio is always almost equal to 1 because the recoiling energy of the proton is negligible. This difference between e-e bremsstrahlung and e-p bremsstrahlung is a significant one. It makes the contribution from e-e bremsstrahlung less important in the nonrelativistic region than that from e-p bremsstrahlung contribution, in addition to the fact that the total e-e bremsstrahlung cross section is much smaller than the total e-p bremsstrahlung cross section at a given energy in this regime.

Equation (2.18) cannot be integrated analytically over photon angles, but because of the azimuthal symmetry about the incident direction it can be integrated numerically over the solid angle $d\Omega = 2\pi \sin\theta d\theta$. The characteristic behavior of equation (2.18) as a function of $\theta$ differs widely depending on E and $\epsilon$. For example, when $\epsilon \ll E \ll mc^2$, equation (2.18) is a very gently varying function in the whole range of $\theta$, from 0 to $2\pi$. When $\epsilon \lesssim \epsilon_{max}$ and $E \gtrsim mc^2$, it varies very rapidly with a small change in $\theta$, and has non-zero values in only very small range of $\theta$. Therefore, in practice, it is not easy to make a computer program which can integrate accurately over the solid angle for a wide range of electron energy, and it is tedious and wasteful to integrate equation (2.18) over the solid angle every time we need to calculate e-e bremsstrahlung from accelerated electrons with a certain spectrum.

We have found that a method of interpolation and extrapolation is very effective in overcoming the difficulty mentioned above. Table 2.1 shows the e-e bremsstrahlung cross sections at various electron energies E and various photon energies E. It is tabulated with two parameters, E and $\eta = \epsilon/\epsilon_{max}$ where $\epsilon_{max}$ is given in equation (2.24). Each of the curves in Figure 2.5 shows the cross section as a function of $\eta$ at a fixed energy. Figure 2.5 is obtained by interpolating the points plotted from Table 2.1. We see that the cross section is a smoothly varying function of $\eta$ at fixed electron energy E. If we plot the cross section as a function of E at fixed $\eta$, we also find that the cross section varies smoothly. Therefore, we can interpolate or extrapolate to find the cross section at an arbitrary value of E and at an arbitrary value of $\epsilon$, by using the values tabulated in Table 2.1 to an accuracy of a few percent. With this method, using Table 2.1, we can readily calculate the e-e bremsstrahlung production rate due to accelerated electrons with an arbitrary spectrum and with an isotropic distribution of momentum vectors.

D. Bremsstrahlung Rates due to Isotropic Electrons with Power-Law Spectra

The primary information available from hard X-ray data is the electron spectrum, from which the number and the energy content of the accelerated electrons can be deduced. Because the bremsstrahlung rate and spectrum are angle-dependent as we have seen in Section B, to deduce the electron spectrum more exactly we need to know the angular distribution of the momentum vectors of the accelerated electrons. However, because such knowledge is not usually available, and because the anisotropy of bremsstrahlung is not large in the nonrelativistic domain, accelerated electrons can be assumed to be isotropic without a danger of gross miscalculation.

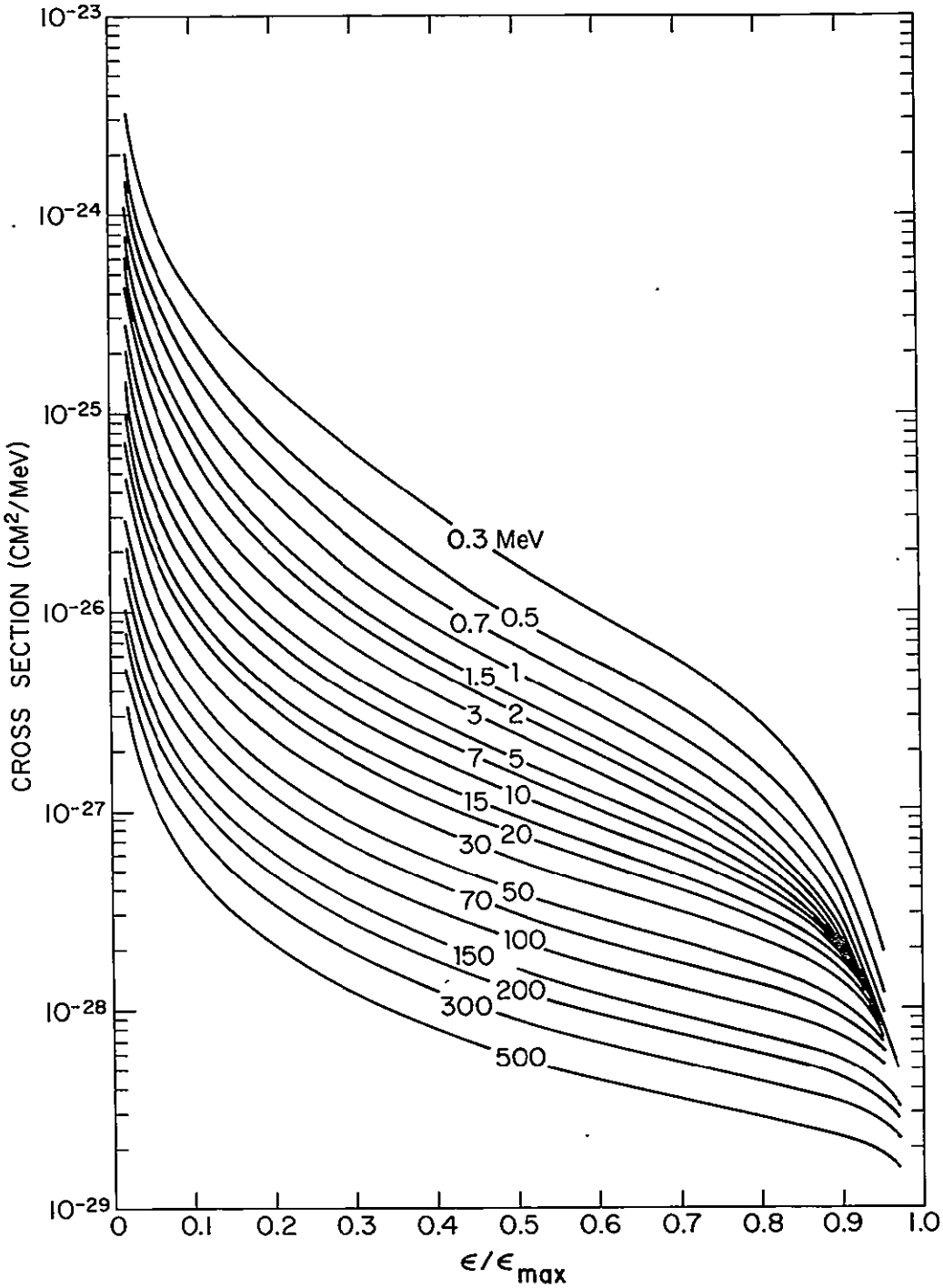


Figure 2.5. Electron-electron bremsstrahlung cross section integrated over the emission angle.

TABLE 2.1

Electron-Electron Bremsstrahlung Cross Section ($cm^2$/MeV).

| E(MeV) \ $\epsilon/\epsilon_{max}$ | 0.100E-01 | 0.200E-01 | 0.500E-01 | 0.100E 00 | 0.150E 00 | 0.200E 00 | 0.250E 00 | 0.300E 00 |
|---|---|---|---|---|---|---|---|---|
| 0.300E 00 | 0.738E-23 | 0.323E-23 | 0.103E-23 | 0.406E-24 | 0.223E-24 | 0.140E-24 | 0.945E-25 | 0.659E-25 |
| 0.500E 00 | 0.461E-23 | 0.200E-23 | 0.627E-24 | 0.240E-24 | 0.128E-24 | 0.785E-25 | 0.511E-25 | 0.341E-25 |
| 0.700E 00 | 0.344E-23 | 0.149E-23 | 0.459E-24 | 0.172E-24 | 0.905E-25 | 0.540E-25 | 0.341E-25 | 0.228E-25 |
| 0.100E 01 | 0.254E-23 | 0.109E-23 | 0.334E-24 | 0.123E-24 | 0.631E-25 | 0.366E-25 | 0.232E-25 | 0.159E-25 |
| 0.150E 01 | 0.182E-23 | 0.779E-24 | 0.235E-24 | 0.844E-25 | 0.420E-25 | 0.246E-25 | 0.151E-25 | 0.112E-25 |
| 0.200E 01 | 0.144E-23 | 0.613E-24 | 0.183E-24 | 0.645E-25 | 0.321E-25 | 0.193E-25 | 0.123E-25 | 0.906E-26 |
| 0.300E 01 | 0.102E-23 | 0.434E-24 | 0.128E-24 | 0.441E-25 | 0.228E-25 | 0.140E-25 | 0.950E-26 | 0.684E-26 |
| 0.500E 01 | 0.658E-24 | 0.277E-24 | 0.795E-25 | 0.282E-25 | 0.151E-25 | 0.958E-26 | 0.664E-26 | 0.435E-26 |
| 0.700E 01 | 0.487E-24 | 0.204E-24 | 0.575E-25 | 0.211E-25 | 0.116E-25 | 0.745E-26 | 0.522E-26 | 0.385E-26 |
| 0.100E 02 | 0.350E-24 | 0.146E-24 | 0.410E-25 | 0.156E-25 | 0.874E-26 | 0.559E-26 | 0.402E-26 | 0.300E-26 |
| 0.150E 02 | 0.238E-24 | 0.964E-25 | 0.282E-25 | 0.111E-25 | 0.631E-26 | 0.416E-26 | 0.297E-26 | 0.223E-26 |
| 0.200E 02 | 0.180E-24 | 0.718E-25 | 0.217E-25 | 0.868E-26 | 0.499E-26 | 0.331E-26 | 0.238E-26 | 0.180E-26 |
| 0.300E 02 | 0.118E-24 | 0.479E-25 | 0.150E-25 | 0.614E-26 | 0.357E-26 | 0.239E-26 | 0.173E-26 | 0.131E-26 |
| 0.500E 02 | 0.691E-25 | 0.291E-25 | 0.944E-26 | 0.395E-26 | 0.232E-26 | 0.157E-26 | 0.114E-26 | 0.874E-27 |
| 0.700E 02 | 0.489E-25 | 0.211E-25 | 0.697E-26 | 0.295E-26 | 0.175E-26 | 0.118E-26 | 0.866E-27 | 0.655E-27 |
| 0.100E 03 | 0.337E-25 | 0.150E-25 | 0.506E-26 | 0.216E-26 | 0.129E-26 | 0.876E-27 | 0.643E-27 | 0.495E-27 |
| 0.150E 03 | 0.225E-25 | 0.103E-25 | 0.351E-26 | 0.152E-26 | 0.907E-27 | 0.620E-27 | 0.456E-27 | 0.352E-27 |
| 0.200E 03 | 0.170E-25 | 0.782E-26 | 0.271E-26 | 0.118E-26 | 0.706E-27 | 0.483E-27 | 0.357E-27 | 0.276E-27 |
| 0.300E 03 | 0.116E-25 | 0.536E-26 | 0.188E-26 | 0.822E-27 | 0.495E-27 | 0.340E-27 | 0.251E-27 | 0.195E-27 |
| 0.500E 03 | 0.719E-26 | 0.334E-26 | 0.118E-26 | 0.522E-27 | 0.315E-27 | 0.217E-27 | 0.161E-27 | 0.125E-27 |

TABLE 2.1

(continued)

| E(MeV) \ E/E max | 0.350E 00 | 0.400E 00 | 0.450E 00 | 0.500E 00 | 0.550E 00 | 0.600E 00 | 0.650E 00 | 0.700E 00 |
|---|---|---|---|---|---|---|---|---|
| 0.300E 00 | 0.465E-25 | 0.327E-25 | 0.234E-25 | 0.172E-25 | 0.130E-25 | 0.100E-25 | 0.771E-25 | 0.585E-26 |
| 0.500E 00 | 0.235E-25 | 0.169E-25 | 0.125E-25 | 0.953E-26 | 0.737E-26 | 0.573E-26 | 0.442E-26 | 0.335E-26 |
| 0.700E 00 | 0.160E-25 | 0.118E-25 | 0.887E-26 | 0.683E-26 | 0.531E-26 | 0.414E-26 | 0.320E-26 | 0.243E-26 |
| 0.100E 01 | 0.114E-25 | 0.849E-26 | 0.648E-26 | 0.502E-26 | 0.393E-26 | 0.307E-26 | 0.233E-26 | 0.181E-26 |
| 0.150E 01 | 0.822E-26 | 0.620E-26 | 0.478E-26 | 0.373E-26 | 0.294E-26 | 0.231E-26 | 0.180E-26 | 0.139E-26 |
| 0.200E 01 | 0.669E-26 | 0.509E-26 | 0.395E-26 | 0.310E-26 | 0.246E-26 | 0.195E-26 | 0.153E-26 | 0.119E-26 |
| 0.300E 01 | 0.512E-26 | 0.393E-26 | 0.308E-26 | 0.245E-26 | 0.196E-26 | 0.157E-26 | 0.125E-26 | 0.985E-27 |
| 0.500E 01 | 0.368E-26 | 0.286E-26 | 0.227E-26 | 0.183E-26 | 0.149E-26 | 0.121E-26 | 0.984E-27 | 0.793E-27 |
| 0.700E 01 | 0.294E-26 | 0.231E-26 | 0.185E-26 | 0.150E-26 | 0.123E-26 | 0.102E-26 | 0.836E-27 | 0.684E-27 |
| 0.100E 02 | 0.229E-26 | 0.181E-26 | 0.147E-26 | 0.120E-26 | 0.997E-27 | 0.831E-27 | 0.694E-27 | 0.577E-27 |
| 0.150E 02 | 0.171E-26 | 0.137E-26 | 0.112E-26 | 0.923E-27 | 0.772E-27 | 0.652E-27 | 0.551E-27 | 0.455E-27 |
| 0.200E 02 | 0.138E-26 | 0.111E-26 | 0.909E-27 | 0.757E-27 | 0.637E-27 | 0.541E-27 | 0.461E-27 | 0.393E-27 |
| 0.300E 02 | 0.101E-26 | 0.818E-27 | 0.674E-27 | 0.566E-27 | 0.480E-27 | 0.410E-27 | 0.354E-27 | 0.305E-27 |
| 0.500E 02 | 0.675E-27 | 0.548E-27 | 0.456E-27 | 0.385E-27 | 0.329E-27 | 0.283E-27 | 0.247E-27 | 0.215E-27 |
| 0.700E 02 | 0.514E-27 | 0.420E-27 | 0.349E-27 | 0.295E-27 | 0.254E-27 | 0.220E-27 | 0.192E-27 | 0.169E-27 |
| 0.100E 03 | 0.383E-27 | 0.314E-27 | 0.262E-27 | 0.223E-27 | 0.191E-27 | 0.166E-27 | 0.145E-27 | 0.129E-27 |
| 0.150E 03 | 0.273E-27 | 0.224E-27 | 0.188E-27 | 0.160E-27 | 0.138E-27 | 0.120E-27 | 0.106E-27 | 0.942E-28 |
| 0.200E 03 | 0.214E-27 | 0.176E-27 | 0.147E-27 | 0.126E-27 | 0.109E-27 | 0.955E-28 | 0.841E-28 | 0.749E-28 |
| 0.300E 03 | 0.151E-27 | 0.124E-27 | 0.105E-27 | 0.896E-28 | 0.777E-28 | 0.683E-28 | 0.603E-28 | 0.539E-28 |
| 0.500E 03 | 0.974E-28 | 0.802E-28 | 0.676E-28 | 0.580E-28 | 0.504E-28 | 0.444E-28 | 0.395E-28 | 0.353E-28 |

PRECEDING PAGE BLANK NOT FILMED

TABLE 2.1

(continued)

| E(MeV) \ $\epsilon/\epsilon_{max}$ | 0.750E 00 | 0.800E 00 | 0.850E 00 | 0.900E 00 | 0.950E 00 | 0.970E 00 |
|---|---|---|---|---|---|---|
| 0.300E 00 | 0.428E-26 | 0.290E-26 | 0.173E-26 | 0.801E-27 | 0.195E-27 | 0.669E-28 |
| 0.500E 00 | 0.244E-26 | 0.166E-26 | 0.996E-27 | 0.471E-27 | 0.122E-27 | 0.438E-28 |
| 0.700E 00 | 0.177E-26 | 0.121E-26 | 0.737E-27 | 0.358E-27 | 0.959E-28 | 0.361E-28 |
| 0.100E 01 | 0.133E-26 | 0.921E-27 | 0.572E-27 | 0.286E-27 | 0.820E-28 | 0.316E-28 |
| 0.150E 01 | 0.103E-26 | 0.726E-27 | 0.463E-27 | 0.242E-27 | 0.739E-28 | 0.297E-28 |
| 0.200E 01 | 0.894E-27 | 0.639E-27 | 0.417E-27 | 0.224E-27 | 0.721E-28 | 0.297E-28 |
| 0.300E 01 | 0.756E-27 | 0.555E-27 | 0.374E-27 | 0.211E-27 | 0.732E-28 | 0.314E-28 |
| 0.500E 01 | 0.626E-27 | 0.476E-27 | 0.336E-27 | 0.203E-27 | 0.782E-28 | 0.357E-28 |
| 0.700E 01 | 0.550E-27 | 0.428E-27 | 0.312E-27 | 0.197E-27 | 0.820E-28 | 0.393E-28 |
| 0.100E 02 | 0.473E-27 | 0.377E-27 | 0.284E-27 | 0.188E-27 | 0.853E-28 | 0.433E-28 |
| 0.150E 02 | 0.388E-27 | 0.318E-27 | 0.248E-27 | 0.173E-27 | 0.863E-28 | 0.471E-28 |
| 0.200E 02 | 0.333E-27 | 0.276E-27 | 0.220E-27 | 0.159E-27 | 0.849E-28 | 0.488E-28 |
| 0.300E 02 | 0.262E-27 | 0.222E-27 | 0.182E-27 | 0.137E-27 | 0.798E-28 | 0.493E-28 |
| 0.500E 02 | 0.187E-27 | 0.162E-27 | 0.136E-27 | 0.108E-27 | 0.691E-28 | 0.465E-28 |
| 0.700E 02 | 0.148E-27 | 0.129E-27 | 0.110E-27 | 0.895E-28 | 0.606E-28 | 0.428E-28 |
| 0.100E 03 | 0.114E-27 | 0.100E-27 | 0.869E-28 | 0.721E-28 | 0.512E-28 | 0.379E-28 |
| 0.150E 03 | 0.839E-28 | 0.743E-28 | 0.652E-28 | 0.551E-28 | 0.411E-28 | 0.318E-28 |
| 0.200E 03 | 0.669E-28 | 0.596E-28 | 0.526E-28 | 0.450E-28 | 0.345E-28 | 0.275E-28 |
| 0.300E 03 | 0.484E-28 | 0.434E-28 | 0.385E-28 | 0.334E-28 | 0.264E-28 | 0.217E-28 |
| 0.500E 03 | 0.318E-28 | 0.287E-28 | 0.258E-28 | 0.226E-28 | 0.184E-28 | 0.156E-28 |

With the assumption of isotropy, we can calculate the instantaneous photon production rate per unit energy interval at photon energy $\epsilon$, by using

$$q(\epsilon) = \int_{\epsilon}^{\infty} dE\, c\beta \frac{d\sigma}{d\epsilon}(E, \epsilon) \int d\vec{x}\, n(\vec{x})\, N_x(E, \vec{x}), \tag{2.25}$$

where $n(\vec{x})$ is the ambient density at the position $\vec{x}$. $N_x(E, \vec{x})$ is the instantaneous number of accelerated electrons per unit volume at the position $\vec{x}$ per unit kinetic energy interval around E, $c\beta$ is the velocity of the electron, and $\frac{d\sigma}{d\epsilon}(E, \epsilon)$ is the bremsstrahlung cross section. Equation (2.25) can be simplified to

$$q(\epsilon) = n \int_{\epsilon}^{\infty} dE\, N(E) c\beta \frac{d\sigma}{d\epsilon}(E, \epsilon), \tag{2.26}$$

where n represents the average value of the ambient density weighted by the local number of accelerated electrons, and N(E) is the instantaneous number of accelerated electrons in the unit energy interval around E in the entire emitting region.

The energy spectra of solar hard X-rays follow a power law in the 20 to 100 keV interval. Flare associated electrons detected in interplanetary space, which might be representative of the accelerated electrons in the flare region, also have power-law spectra. Because accelerated electrons with power-law spectra produce hard X-rays with power-law spectra, one might expect that the accelerated electrons in the flare region have power-law energy spectra. Thus, it is important to calculate photon production rates due to accelerated electrons with power-law spectra.

Figure 2.6 shows the photon production rates due to e-p bremsstrahlung of accelerated electrons with power-law spectra. The ambient density n has been normalized to 1 $cm^{-3}$, and the number of accelerated electrons with energies greater than 20 keV, to 1. The production rates are multiplied by $(\epsilon/20\ \text{keV})^s$, where $\epsilon$ is the photon

energy and s is the spectral index of the accelerated electrons. The resultant photon spectra, q ($\epsilon$), indeed follow a power law in the 10 ~100 keV interval; they gradually flatten in the 100 ~1000 keV interval; and then in the 1 ~10 MeV interval they again follow a power law with smaller indexes than in the 10 ~ 100 keV interval.

Similarly, we have calculated the photon production rates due to e-e bremsstrahlung of the accelerated electrons with power law energy spectra, which are shown in Figure 2.7. Here also the ambient electron density $n_e$ is normalized to 1 $cm^{-3}$, and the number of the accelerated electrons with energies greater than 20 keV is normalized to 1, as in Figure 2.7. Compared with the results shown in Figure 2.6, the e-e bremsstrahlung contribution becomes important as the electron kinetic energy becomes greater than or comparable to the electron rest mass energy. The ratio between the e-e bremsstrahlung contribution and the e-p bremsstrahlung contribution at a given energy increases as the electron spectrum flattens. This is because $\epsilon_{max}$ for e-e bremsstrahlung is much smaller than E, while $\epsilon_{max}$ for e-p bremsstrahlung is almost the same as E. Therefore, more energetic electrons are needed to produce photons with a given energy through e-e bremsstrahlung than through e-p bremsstrahlung.

Total bremsstrahlung yields from accelerated electrons with power-law spectra in the fully ionized hydrogen plasma can be obtained by adding the results in Figures 2.6 and 2.7. The results are shown in Figure 2.8. Most astrophysical bremsstrahlung sources, including solar flares, can be well approximated by a hydrogen plasma. (However, for calculations of Chapter V, we take the photospheric abundances into account.) As the figure shows, the resultant photon spectra follow a power law in the 10 to 100 keV interval. In the 10 to 70 keV interval, where most of the solar hard X-rays are observed, the resultant photon spectra, q($\epsilon$), can be approximated as

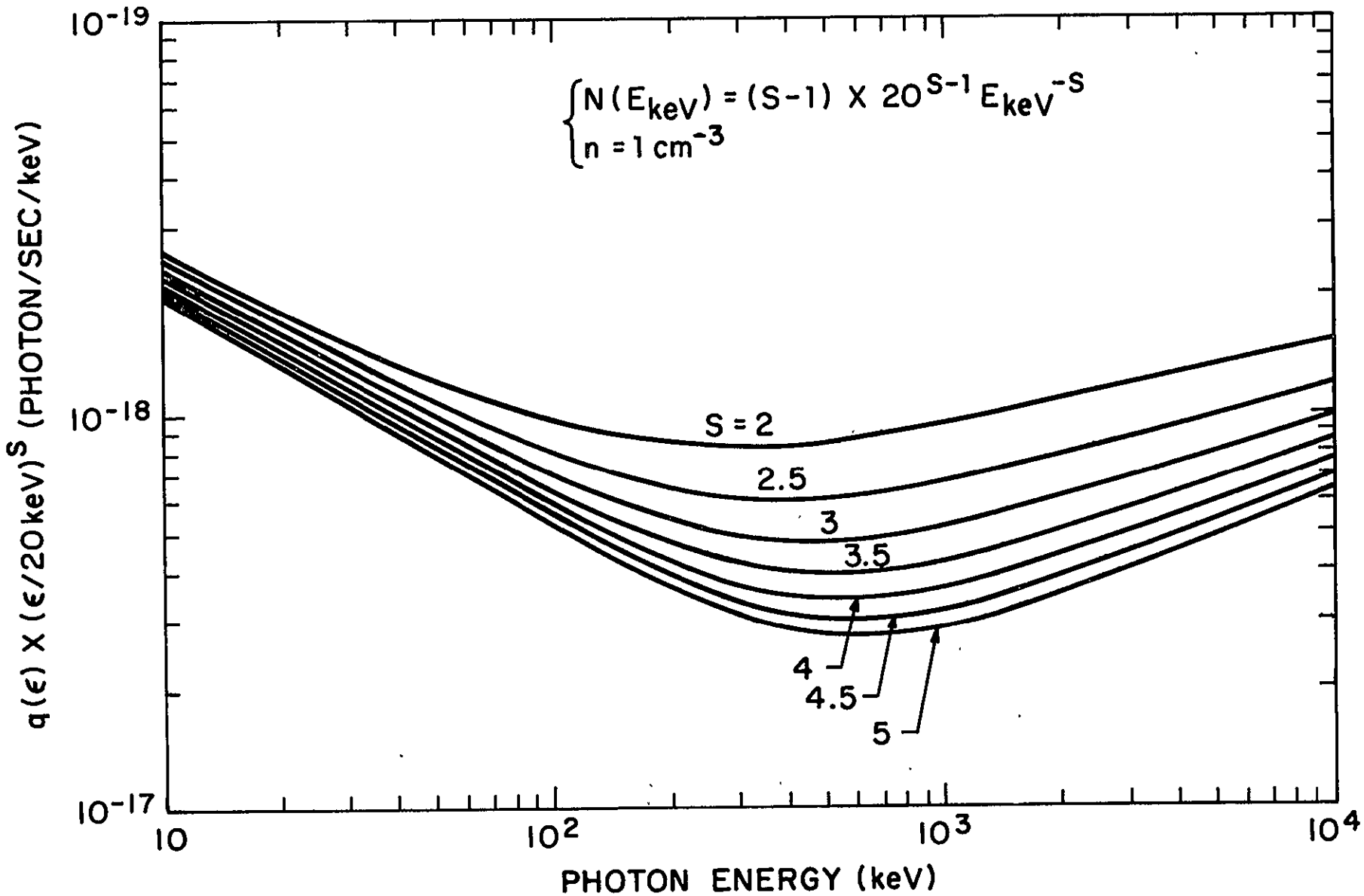


Figure 2.6. Photon production rates due to e-p bremsstrahlung of accelerated electrons with power-law spectra. The angular distribution of the momentum vectors of the electrons are assumed to be isotropic. s represents the power index.

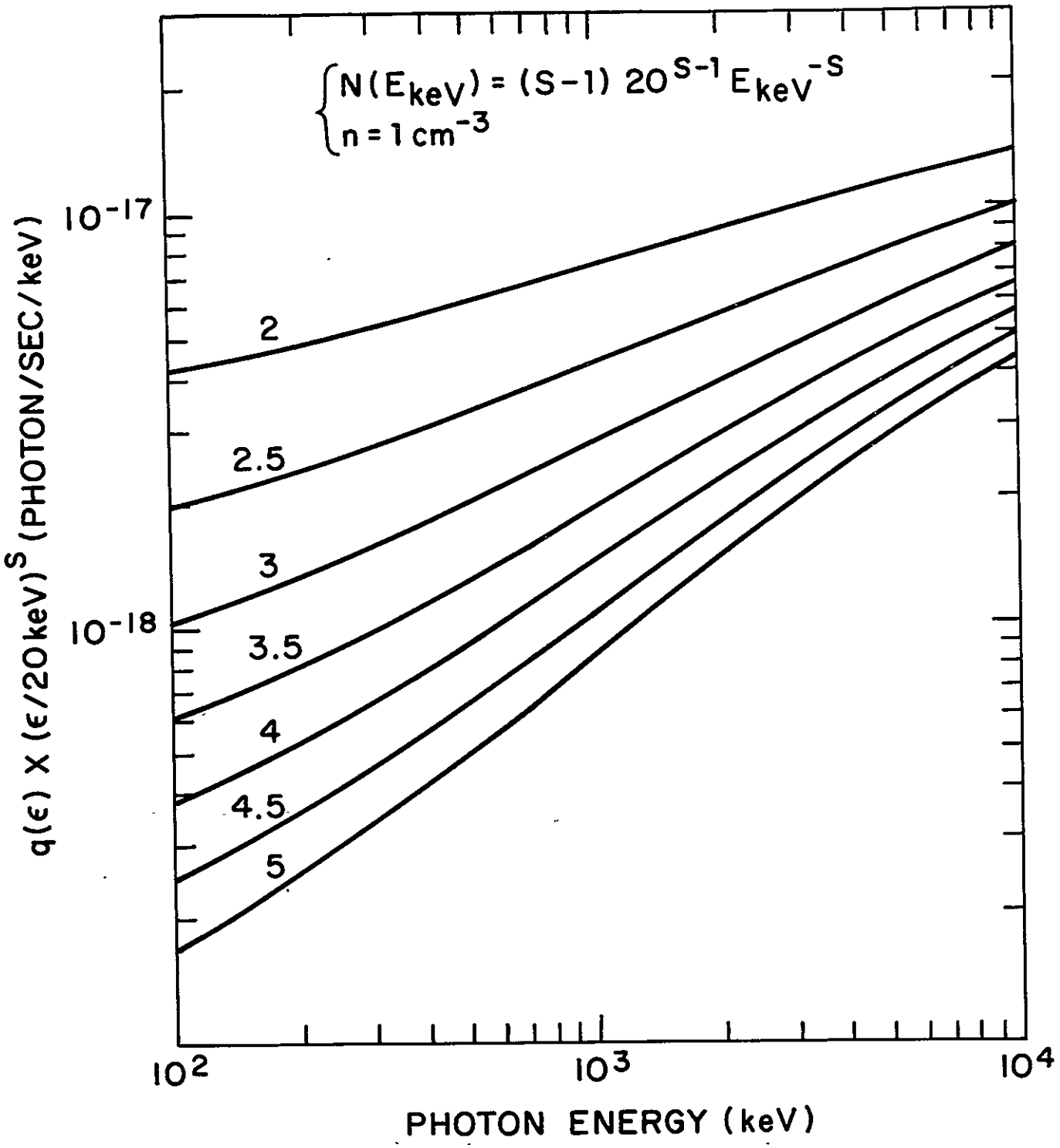


Figure 2.7. Photon production rates due to e-e bremsstrahlung of accelerated electrons with power-law spectra. The same assumptions are made as in Figure 2.6.

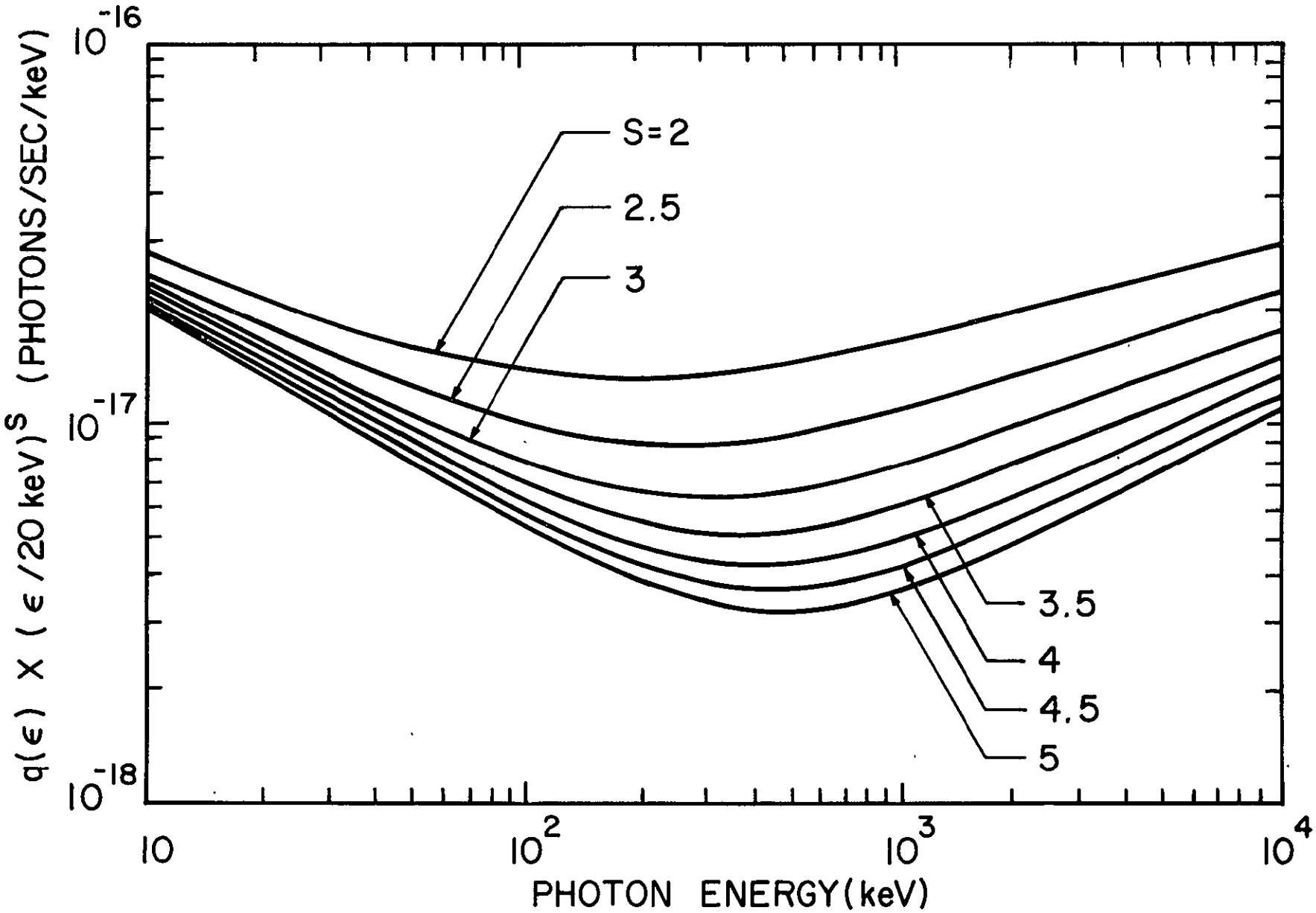


Figure 2.8. Total photon production rates obtained by adding up the results of Figures 2.6 and 2.7.

$$q(\epsilon) = 10^{-17}\, A_1(s) \left(\frac{\epsilon}{20\ \mathrm{keV}}\right)^{-\delta_1(s)} \text{(photons/sec/keV)}, \tag{2.27}$$

where $A_1$ and $\delta_1$ are plotted in Figure 2.9 as functions of s. As can be seen in Figure 2.9, $\delta_1 \simeq s + 0.5$, in agreement with the conventional wisdom.

By using an analytical method and the nonrelativistic Bethe-Heitler formula (Koch and Motz 1959, Equation 3BN.a) for the bremsstrahlung cross section, Brown (1971, 1975) obtained a relationship between solar hard X-ray spectra and accelerated electron spectra at the sun. He reported that the photon spectra are steeper by a unit power index than the electron flux spectra at the emitting region.. Since in the nonrelativistic region the electron flux spectrum is flatter than the electron number spectrum by one half power, his result is a good approximation. After converting units, we find that the flux at 20 keV of his result is similar to our result. The differences between our result and his are due partly to the e-e bremsstrahlung contribution taken into account in our result and partly to Brown's use of the approximate non-relativistic e-p bremsstrahlung cross-section formula.

In many astrophysical sources bremsstrahlung by relativistic electrons is important. Therefore, an expression for the relationship between the accelerated electron spectra and the bremsstrahlung spectra is useful. The bremsstrahlung spectra produced by accelerated electrons with the spectra,

$$N(E)dE = (s-1)E^{-s}\,dE, \tag{2.28}$$

can be expressed by

$$q(\epsilon) = 5 \times 10^{-17} A_2(s)\epsilon^{-\delta_2(s)} \text{(photons/sec/MeV)}, \tag{2.29}$$

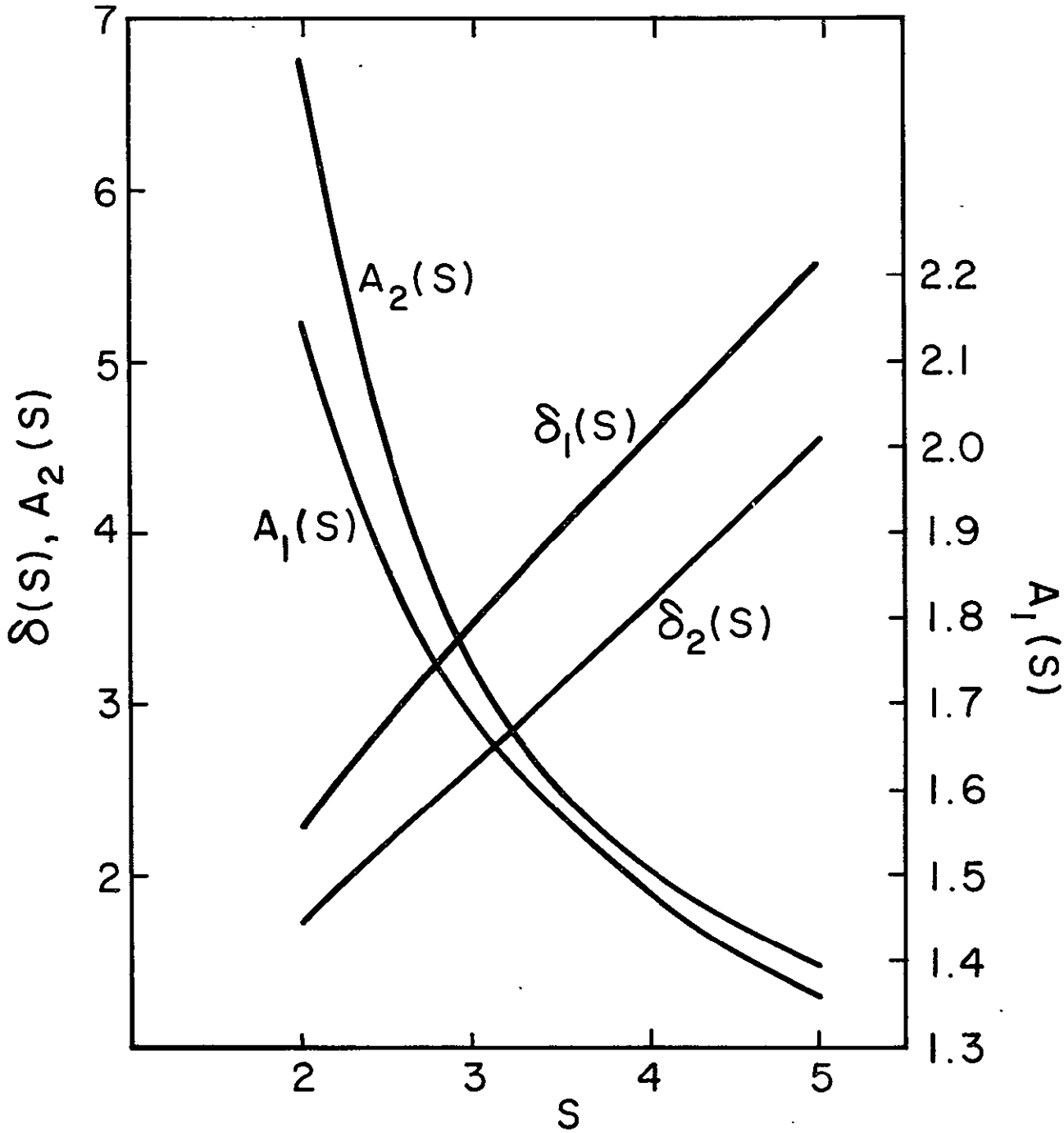


Figure 2.9. Plot of $A_1(s)$, $\delta_1(s)$, $A_2(s)$, and $\delta_2(s)$.

where E and $\epsilon$ are in MeV, and the ambient density is 1 $cm^{-3}$. $A_2(s)$ and $\delta_2(s)$ are also plotted in Figure 2.9. We see that $\delta_2 \simeq s - 0.4$.

# CHAPTER III

# A COHERENT STUDY OF POLARIZATION, COMPTON BACKSCATTER, ANISOTROPY, AND ALBEDO PATCH OF SOLAR HARD X-RAYS

## A. Introduction

As we have seen in Chapter II, hard X-rays from solar flares are mainly due to bremsstrahlung of accelerated electrons. Because bremsstrahlung is directional and it is also polarized, the study of the directionality of solar hard X-rays and/or the study of their polarization can lead to the knowledge on the angular distribution of the accelerated electrons in the emitting region. Such knowledge is essential in determining whether hard X-rays are due to thermal or nonthermal electrons.

Brown (1972) and Petrosian (1973) studied the anisotropy of hard X-rays due to electrons beaming down toward the photosphere, and they reported that for such anisotropic models a flare near the limb would be brighter by a factor of 5 or so than the flare with a similar intrinsic X-ray strength near the disk center. However, such a large limb brightening effect was not confirmed by observations (Kane 1974, Datlowe, Elcan, and Hudson 1974).

It was first pointed out by Korchak (1967) and by Elwert (1968) that the measurement of polarization of solar hard X-rays can also lead to the knowledge on the anisotropy of the accelerated electrons. A series of measurements by Tindo and his coworkers (Tindo et al. 1970, 1972a, 1972b, Tindo, Mandelstam, and Shuryghin 1973) and a measurement by Nakada, Neupert, and Thomas (1974) showed that solar hard X-rays are indeed polarized. Further calculations of polarization due to anisotropic distributions of accelerated electrons was performed by several authors for various cases: for soft X-rays by Elwert and Haug (1970), for hard X-rays due to electrons

with given pitch angle by Haug (1972), and for the thick-target by Brown (1972). In summary, these authors obtained the following result. Hard X-rays produced by accelerated electrons with their momentum vectors mainly in downward directions are partially polarized parallel to the plane containing the line of sight and the normal to the photosphere at the flare site, and the degree of polarization increases with the heliocentric angle of the flare, from zero at the disk center to the maximum polarization at the limb.

However, as pointed out by Tomblin (1972) and by Santangelo, Horstman and Horstman-Moretti (1973), photons in the energy range from 10 to 100 keV, when emitted down toward the photosphere, have a high probability of being reflected due to Compton scattering. As a result of this reflection, both the spectrum and the intensity of the X-rays are significantly modified, especially for anisotropic X-ray sources which radiate predominantly in the downward direction. Furthermore, the Compton scattering cross section is dependent upon the polarization of photons. Because, on one hand, the backscattered photon component influences the degree of polarization, while on the other hand, the reflectivity depends on the polarization, the anisotropy, the polarization, and the backscatter of solar hard X-rays should be studied together in a coherent fashion.

Until recently, however, the effect of the Compton backscatter was not taken into account in the studies of the anisotropy and the polarization of solar hard X-rays (Elwert and Haug 1970, Haug 1972, Brown 1972, Petrosian 1973), nor was the effect of the anisotropy (and the polarization) of the primary photon source taken into consideration in the study of the backscatter (Santangelo et al. 1973). Recently, Henoux (1975) considered the effect of the Compton backscatter on the anisotropy and the

polarization of solar hard X-rays. However, he used somewhat unrealistic anisotropic models in which electrons are spiraling down with given pitch angles 0°, 60°, and 90° for each case. We have recently learned, while this thesis was in preparation, that Langer and Petrosian (1977) have also treated a similar problem for beams of electrons directed vertically down toward the photosphere.

As discussed above, the Compton backscatter complicates the relationships between the anisotropy and the polarization of hard X-rays and the anisotropy of the accelerated electrons. This backscatter, however, may give extra information by reflecting the photons incident on the photosphere which could not be observed otherwise. If the size of the primary X-ray source is considerably smaller than its height, then in principle the primary source can be resolved from its albedo. When such resolution is possible, three independent measurements can give information on the height of the primary source and the anisotropy. These are the ratio between the number of primary X-rays and the number of reflected X-rays, the distribution of surface brightness of the albedo patch (the bright area on the photosphere from which X-rays are reflected), and, if the primary source is not at the disk center, the displacement of the projection of the source with respect to the centroid of the albedo patch. Brown, van Beek, and McClymont (1975) discussed the possibility of determining the height of the primary X-ray source from the size of the albedo patch. It is anticipated that such measurements could be performed by the Hard X-ray Imaging Spectrometer which will be included in the payload of NASA's Solar Maximum Mission. In their calculations, however, Brown et al. (1975) assumed that the reflection probability is independent of the incident direction of the photon. However, this assumption is not valid in general.

In this chapter we study the anisotropy, polarization, Compton backscatter, and albedo brightness distribution, and other related problems of solar hard X-rays in detail and coherently. In Section B we review the methods of representing the state of polarization by Stokes parameters and of expressing the Compton scattering cross section in matrix form. We further study how to calculate the Stokes parameters of primary X-rays due to anisotropic distributions of accelerated electrons, and we describe the Monte Carlo simulation used in this chapter. In Section C we discuss briefly the general properties of the Compton backscatter, and present the results of our Monte Carlo simulations for isotropic primary sources as well as anisotropic polarized primary sources. Here we discuss the directivity of the sum of photons due to the primary source and those due to the backscatter. We also discuss the characteristics of the energy spectra of the resultant hard X-rays, and compare the results with the observed OSO-7 data (Datlow et al. 1974).

In Section D, by taking the effect of Compton backscatter into account, we study the polarization of solar hard X-rays due to both isotropic, unpolarized, and anisotropic, polarized primary sources. In Section E, by calculating the differential reflectivity of a beam of photons for various incident angles, we study in detail the characteristics of the albedo patch, which is a bright X-ray patch on the photosphere created by the Compton backscatter. Information on the height of the primary source, the anisotropy, and polarization of primary hard X-rays might be obtained from detailed albedo measurements. In Section F we summarize our results and compare with other researchers' theoretical and observational results.

## B. Methods of Calculations

### 1. The Stokes Parameters and the Matrix Representation of the Compton Scattering Cross Section

Hard X-rays released down to the photosphere are either Compton scattered or absorbed by the photoelectric effect. The differential Compton cross section is given by (Klein and Nishina 1929)

$$\frac{d\sigma_c}{d\Omega}(\epsilon_o, \theta_s, \Theta) = \frac{1}{4} r_o^2 \left(\frac{\epsilon}{\epsilon_o}\right)^2 \left(\frac{\epsilon_o}{\epsilon} + \frac{\epsilon}{\epsilon_o} - 2 + 4\cos^2\Theta\right) \tag{3.1}$$

Here $\theta_s$ is the scattering angle, $\Theta$ is the angle between the directions of polarization of the initial photon and the final photon, $r_o = 2.82 \times 10^{-13}$ cm, and $\epsilon_o$ and $\epsilon$ are the initial and final photon energies related by

$$\epsilon = \epsilon_o/[1 + (\epsilon_o/mc^2)(1 - \cos\theta_s)], \tag{3.2}$$

where $mc^2$ is the electron rest mass energy.

The formula given by equation (3.1) is applicable only to a coherent beam with plane polarization or to a beam of photons whose exact distribution of polarization vectors is known. To deal with a beam of photons with an arbitrary distribution of polarization vectors, it is more advantageous to use the Stokes parameters, because they are directly measurable quantities and are additive for independent (noncoherent) emission fluxes. In the application of the Stokes parameters to a Compton scattering problem, it is convenient to write them in the form of a four-vector and to use the matrix representation of the Compton cross section. The matrix representation of the Compton cross section has been well reviewed by McMaster (1961).

The Stokes parameters are represented by a four vector,

$$\begin{pmatrix} I \\ P_1 \\ P_2 \\ P_3 \end{pmatrix} = \begin{pmatrix} I \\ \vec{P} \end{pmatrix} \tag{3.3}$$

Here I represents the beam intensity and is normalized to 1 throughout in this thesis; $P_1 = (I_\perp - I_{||})/I$ represents the degree of polarization measured with respect to a given reference plane; $P_2$ represents the degree of polarization measured with respect to a plane rotated around the direction of the propagation by 45° from the reference plane; and $P_3$ represents the state of circular polarization. For example, $\begin{pmatrix} 1 \\ 0 \\ 0 \\ 0 \end{pmatrix}$ represents an unpolarized beam, $\begin{pmatrix} 1 \\ \pm 1 \\ 0 \\ 0 \end{pmatrix}$ represent plane polarization perpendicular (parallel) to the reference plane, $\begin{pmatrix} 1 \\ 0 \\ \pm 1 \\ 0 \end{pmatrix}$ represent plane polarization perpendicular (parallel) to the plane obtained by rotating the reference plane by 45°, and $\begin{pmatrix} 1 \\ 0 \\ 0 \\ \pm 1 \end{pmatrix}$ represent left (right) circular polarization. Since photons with circular polarization carry angular momentum, bremsstrahlung photons produced by unpolarized electrons have no circular polarization. Since we consider only unpolarized electron beams, we neglect circular polarization in this thesis. The Stokes parameters can, therefore, be written as a three-vector, $\begin{pmatrix} 1 \\ P_1 \\ P_2 \end{pmatrix}$.

Since the Stokes parameters are coordinate dependent, there exists a rotation matrix $\underline{\underline{M}}$ for the Stokes parameters (McMaster 1961):

$$\underline{\underline{M}} = \begin{pmatrix} 1 & 0 & 0 \\ 0 & \cos 2\phi & \sin 2\phi \\ 0 & -\sin 2\phi & \cos 2\phi \end{pmatrix}, \tag{3.4}$$

where $\phi$ is the angle of rotation around the direction of the propagation. Note that $\underline{\underline{M}}$ is a unit matrix when $\phi = \pi$, as it should be.

The matrix representation of the Klein-Nishina formula is given by (McMaster 1961)

$$\underline{\underline{T}} = \frac{1}{2} r_o^2 \left(\frac{\epsilon}{\epsilon_o}\right)^2 \begin{pmatrix} \frac{\epsilon_o}{\epsilon} + \frac{\epsilon}{\epsilon_o} - \sin^2\theta_s & \sin^2\theta_s & 0 \\ \sin^2\theta_s & 1+\cos^2\theta_s & 0 \\ 0 & 0 & \cos 2\theta_s \end{pmatrix}, \tag{3.5}$$

where the scattering plane is the reference plane for the Stokes parameters to which this formula is applied. When a beam of photons characterized by the Stokes parameters $\begin{pmatrix} 1 \\ P_1 \\ P_2 \end{pmatrix}$ with respect to a given reference plane is Compton scattered along the direction $(\theta_s, \phi_s)$, the Stokes parameters after the scattering are obtained in the following manner. First, apply a rotation matrix to find the Stokes parameters with respect to the scattering plane; then apply the Compton scattering matrix. The Stokes parameters after the scattering are then given by

$$\begin{pmatrix} 1 \\ P_1' \\ P_2' \end{pmatrix} \sim \underline{\underline{T}} \begin{pmatrix} 1 & 0 & 0 \\ 0 & \cos 2\phi_s & \sin 2\phi_s \\ 0 & -\sin 2\phi_s & \cos 2\phi_s \end{pmatrix} \begin{pmatrix} 1 \\ P_1 \\ P_2 \end{pmatrix}$$

$$\sim \begin{pmatrix} \frac{\epsilon_o}{\epsilon} + \frac{\epsilon}{\epsilon_o} - \sin^2\theta_s & \sin^2\theta_s & 0 \\ \sin^2\theta_s & 1+\cos^2\theta_s & 0 \\ 0 & 0 & 2\cos\theta_s \end{pmatrix} \begin{pmatrix} 1 \\ P_1 \cos 2\phi_s + P_2 \sin 2\phi_s \\ P_2 \cos 2\phi_s - P_1 \sin 2\phi_s \end{pmatrix}.$$

$$\sim \begin{pmatrix} \frac{\epsilon_o}{\epsilon} + \frac{\epsilon}{\epsilon_o} - \sin^2\theta_s + \sin^2\theta_s\,(P_1 \cos 2\phi_s + P_2 \sin 2\phi_s) \\ \sin^2\theta_s + (1+\cos^2\theta_s)(P_1 \cos 2\phi_s + P_2 \sin 2\phi_s) \\ 2\cos\theta_s (P_2 \cos 2\phi_s - P_1 \sin 2\phi_s) \end{pmatrix}, \tag{3.6}$$

where $\phi_s$ is the azimuthal angle of the scattering plane measured with respect to the reference plane.

The Stokes parameters after the scattering given by equation (3.6) are measured with respect to the scattering plane. However, the scattering plane is not a unique plane to be used as a reference plane. If the distribution of the accelerated electrons (and consequently that of the hard X-rays) is symmetric around the normal to the photosphere, the plane containing the normal and the direction of the photon propagation defines a unique plane, with respect to which we can calculate the Stokes parameters of the photon flux propagating along that direction. Because this plane is normal to the photosphere, let us call it the normal plane hereafter.

The angle between the scattering plane and the normal plane of the photon after the scattering, $\alpha$, is given by (Appendix A)

$$\cos\alpha = -(\cos\theta_1 \sin\theta_s + \sin\theta_1 \cos\theta_s \cos\phi_s)/\sin\theta_2, \tag{3.7}$$

$$\sin\alpha = \sin\theta_1 \sin\phi_s/\sin\theta_2, \tag{3.8}$$

where $\theta_1$ is the polar angle of the photon ensemble before the scattering, $(\theta_s, \phi_s)$ are the scattering angles, and $\theta_2$ is the polar angle of the photon ensemble after the scattering, which is given by

$$\cos\theta_2 = \cos\theta_1 \cos\theta_s - \sin\theta_1 \sin\theta_s \cos\phi_s. \tag{3.9}$$

Thus, the Stokes parameters with respect to the normal plane after the scattering is given by

$$\begin{pmatrix} 1 \\ P_1'' \\ P_2'' \end{pmatrix} = \begin{pmatrix} 1 & 0 & 0 \\ 0 & \cos 2\alpha & \sin 2\alpha \\ 0 & -\sin 2\alpha & \cos 2\alpha \end{pmatrix} \begin{pmatrix} 1 \\ P_1' \\ P_2' \end{pmatrix}, \tag{3.10}$$

where $\alpha$ is given by equations (3.7) through (3.9), and $P_1'$ and $P_2'$ are given by equation (3.6).

The Compton scattering cross section for a polarized beam is given by

$$\frac{d\sigma}{d\Omega}(\theta_s, \phi_s) = (1 \quad 0 \quad 0) \cdot \underline{\underline{T}} \begin{pmatrix} 1 & 0 & 0 \\ 0 & \cos 2\phi_s & \sin 2\phi_s \\ 0 & -\sin 2\phi_s & \cos 2\phi_s \end{pmatrix} \begin{pmatrix} 1 \\ P_1 \\ P_2 \end{pmatrix}$$

$$= \frac{1}{2} r_0^2 \left(\frac{\epsilon}{\epsilon_o}\right)^2 \left\{ \frac{\epsilon}{\epsilon_o} + \frac{\epsilon_o}{\epsilon} - \sin^2 \theta_s (1 - P_1 \cos 2\phi_s - P_2 \sin 2\phi_s) \right\}. \tag{3.11}$$

where $\phi_s$ is the angle between the scattering plane and the reference plane for the Stokes parameters. For an unpolarized beam, this formula becomes

$$\frac{d\sigma_c}{d\Omega}(\epsilon_o, \theta_s) = \frac{1}{2} r_o^2 \left\{ \left(\frac{\epsilon}{\epsilon_o}\right)^3 + \frac{\epsilon}{\epsilon_o} - \left(\frac{\epsilon}{\epsilon_o}\right)^2 \sin^2 \theta_s \right\}. \tag{3.12}$$

This cross section formula is also the same as equation (3.11) averaged over $\phi_s$. This cross section is plotted in Figure 3.1 as a function of $\theta_s$ for several values of $\epsilon_o$. The total Compton cross section is

$$\sigma_c(\epsilon_o) = 2\pi r_o^2 \left\{ \frac{1+\alpha}{\alpha^2} \left[ \frac{2(1+\alpha)}{1+2\alpha} - \frac{\ln(1+2\alpha)}{\alpha} \right] \right.$$

$$\left. + \frac{\ln(1+2\alpha)}{2\alpha} - \frac{1+3\alpha}{(1+2\alpha)^2} \right\}, \tag{3.13}$$

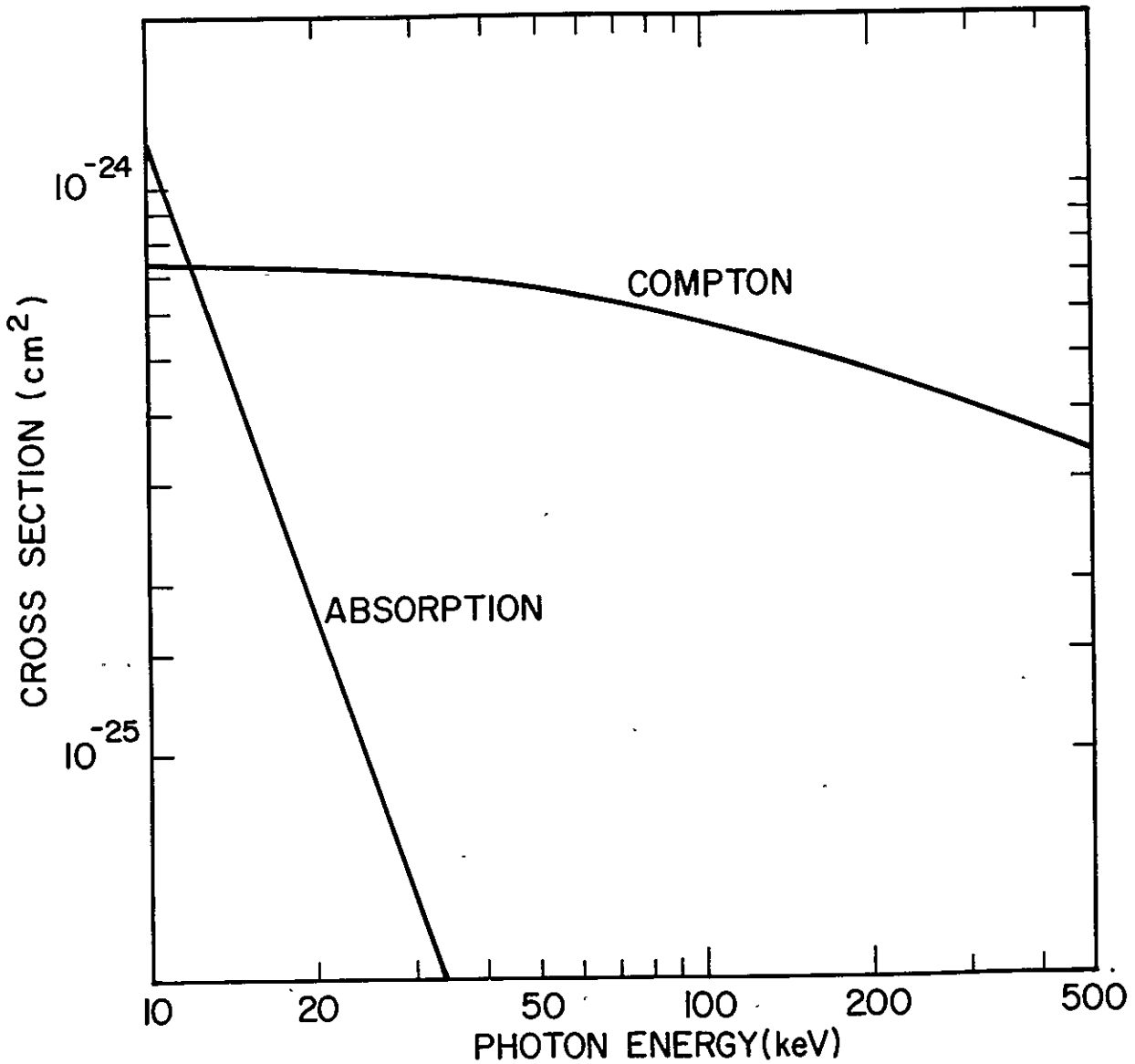


Figure 3.1. Differential Compton cross section of unpolarized radiation, for several values of $\epsilon_o/mc^2$. The curve for $\epsilon_o/mc^2 = 0$ corresponds to the Thompson cross section.

where $\alpha = \epsilon_o/mc^2$. In our calculation we multiply this cross section by 1.15 to take into account the effects of He and heavier elements.

We use the photoelectric absorption cross section, $\sigma_a$, given by Fireman (1974). At the energies of interest ($\gtrsim$10 keV), this cross section depends mainly on the abundance of heavy elements such as O, Fe, and Ni. Fireman (1974) used the photospheric abundances given by Withbroe (1971). The following analytical form is a good approximation to the extrapolation of his result to energies $\gtrsim$10 keV:

$$\sigma_a(\epsilon_o) = 7.2 \times 10^{-22}\ \epsilon_o^{-2.78}\ (\mathrm{cm}^2/\text{H-atom}), \tag{3.14}$$

where $\epsilon_o$ is in keV. This cross section asymptotically approaches to the form $\epsilon_o^{-3}$ as energy increases; however, equation (3.14) is a better approximation in the regime where the absorption is important. This absorption cross section and the total Compton cross section are plotted in Figure 3.2 as functions of the photon energy.

2. Calculation of the Stokes Parameters of the Bremsstrahlung Hard X-Rays due to Anisotropic Electrons

As we have seen, the Compton cross section depends on the degree of polarization. Therefore, to calculate the backscatter, we need to know the degree of polarization of primary hard X-rays and to follow the polarization throughout the scattering process. Because for the integral reflectivity the azimuthal dependence of the Compton cross section given by equation (3.11) is averaged over various incident and outgoing directions, the integral reflectivity is not much affected by neglecting the polarization dependence. However, the angular dependence of the reflectivity (the differential reflectivity) and especially the albedo brightness distribution are expected to be affected by the polarization dependence of the Compton cross section.

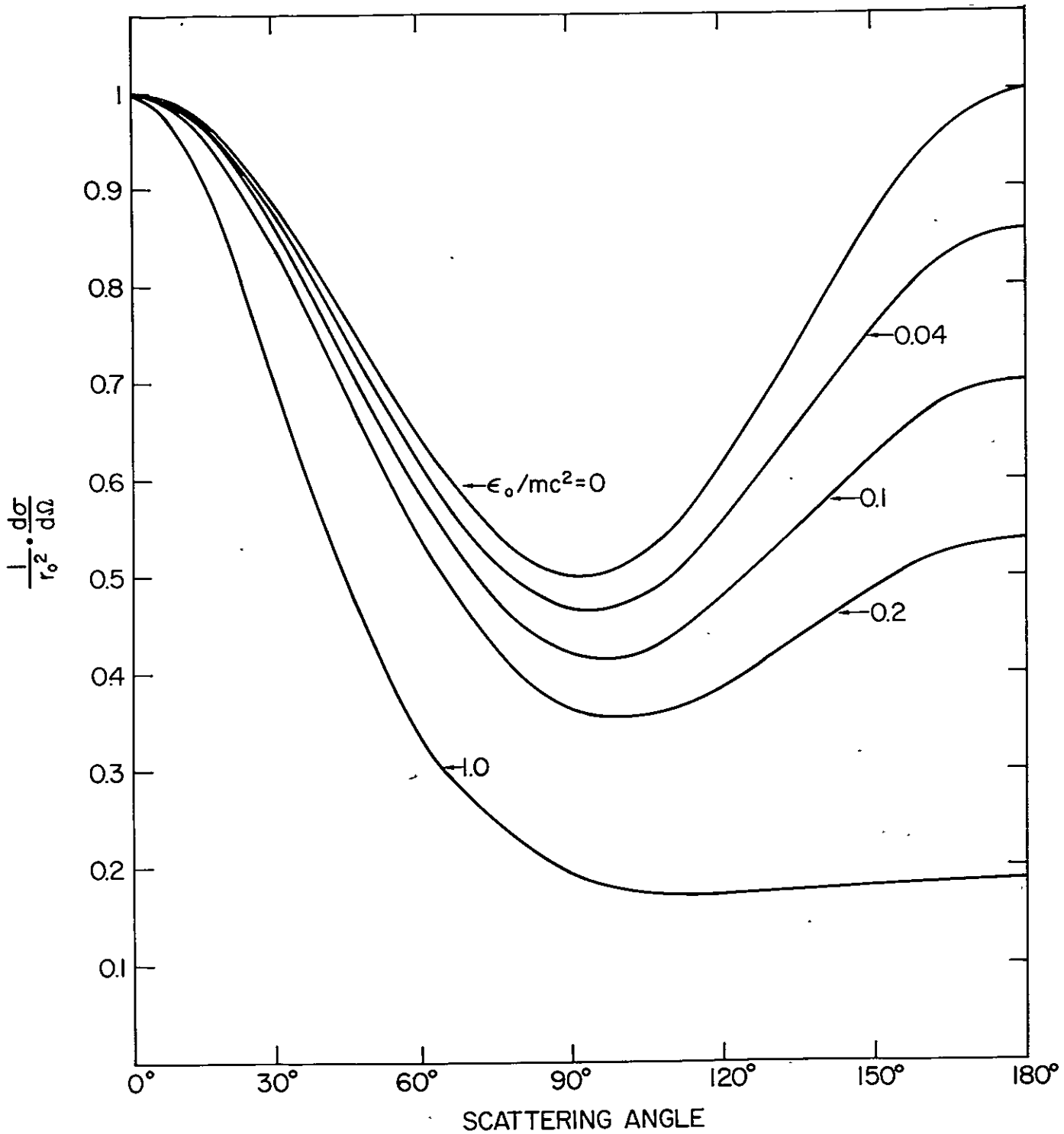


Figure 3.2. Photoelectric absorption cross section and total Compton cross section.

The degree of polarization of bremsstrahlung due to a beam of monoenergetic electrons is given by

$$P_1(\epsilon, \theta) = \left[ \frac{d\sigma_\perp}{d\Omega}(E, \epsilon, \theta) - \frac{d\sigma_{||}}{d\Omega}(E, \epsilon, \theta) \right] \Big/ \frac{d\sigma}{d\Omega}(E, \epsilon, \theta), \tag{3.15}$$

where $\frac{d^2\sigma_\perp}{d\epsilon d\Omega}$ and $\frac{d^2\sigma_{||}}{d\epsilon d\Omega}$ are given by equations (2.15) and (2.16), E is the energy of the electron, $\epsilon$ is the photon energy, and $\theta$ is the angle of emission measured relative to the beam direction. Here the polarization is measured with respect to the radiation plane which contains the beam direction and the direction of photon propagation. When the momentum vectors of the accelerated electrons have a certain distribution, the radiation plane is not a unique plane with respect to which we measure the Stokes parameters. If the angular distribution of the electron momentum vectors are symmetric around the normal to the photosphere (as will be the case if the guiding magnetic field lines are perpendicular to the photosphere), the normal plane, as we mentioned earlier, is a unique reference plane for the Stokes parameters.

The bremsstrahlung produced by the electrons with a distribution function of the momentum vectors,

$$g(\theta, \phi) \equiv g(\theta) \tag{3.16}$$

is given by

$$Q(\epsilon, \theta) = n \int_{\epsilon}^{\infty} dE \int_{-1}^{+1} d(\cos\theta_o) \int_0^{2\pi} d\phi_o g(\theta_o) \frac{d^2\sigma(E, \epsilon, \theta')}{d\epsilon d\Omega'} N(E) v(E), \tag{3.17}$$

Here N(E) is the instantaneous differential electron number, n is the ambient density, v(E) is the electron velocity, $\theta$ is the angle between the line of sight and the normal to

the photosphere, $(\theta_o, \phi_o)$ is the polar coordinate of the momentum vector of the electron in the system whose Z-axis is the normal to the photosphere, $\theta'$ is the angle between the line of sight and the momentum vector of the electron, and it is given by

$$\cos\theta' = \cos\theta \cos\theta_o + \sin\theta \sin\theta_o \cos\phi_o. \tag{3.18}$$

And $\frac{d^2\sigma}{d\epsilon d\Omega'}(E, \epsilon, \theta')$ is the differential bremsstrahlung cross section.

To calculate the Stokes parameters $(1, P_1, P_2)$ due to such an electron distribution, we need to find the Stokes parameters with respect to the normal plane of the bremsstrahlung by an electron beam at a given direction and integrate over the electron direction. It can be shown that one of the Stokes parameters with respect to the normal plane is given by (e.g., Haug 1972)

$$P_1(\epsilon, \theta) = \left\{ \int_{\epsilon}^{\infty} dE \int_{-1}^{+1} d(\cos\theta_o) \int_{0}^{2\pi} d\phi_o g(\theta_o) \cos 2\alpha \left[ \frac{d^2\sigma_{\perp}(E, \epsilon, \theta)}{d\epsilon d\Omega} - \frac{d^2\sigma_{\parallel}(E, \epsilon, \theta)}{d\epsilon d\Omega} \right] N(E) v(E) \right\} \Big/ Q(\epsilon, \theta), \tag{3.19}$$

where $Q(\epsilon, \theta)$ is given by equation (3.17), $\theta'$ is given by equation (3.18) and $\alpha$ is the angle between the radiation plane and the normal plane, which is given by

$$\cos\alpha = (\cos\theta \sin\theta_o \cos\phi_o - \sin\theta \cos\theta_o)/\sin\theta'. \tag{3.20}$$

Another Stokes parameter, $P_2(\epsilon, \theta)$, is equal to zero because of the symmetry around the normal plane.

## 3. A Monte Carlo Simulation

We evaluate the backscattering of primary photons by using a Monte Carlo simulation (see Appendix B for its explanation). Since we use the Stokes parameters which characterize an ensemble of photons, the unit of the photon flux is not an individual photon but a photon ensemble characterized by the Stokes parameters. In determining whether the absorption or Compton scattering take place, we treat this photon ensemble as if it were an individual photon. Such a treatment increases the accuracy of the calculated polarization.

For linearly polarized photon beams, we can use an individual photon approach, by regarding the photon beam to consist of an unpolarized beam and a completely polarized beam, by choosing the polarization vector of each individual photon accordingly and by using the cross section given by equation (3.1) (Langer and Petrosian 1977). However, this approach is less advantageous than the approach using the Stokes parameters. In the latter approach, for a given photon beam the degree of polarization of the photons scattered along a given direction is exactly determined by the ensemble average given by equation (3.6). On the other hand, the degree of polarization calculated by the former approach is determined statistically and consequently contains a statistical error.

We choose the incident direction of the photon in accordance with the angular distribution of a source function $Q(\epsilon_o,\theta_o,\phi_o)$, where $\theta_o$ and $\phi_o$ are the polar and azimuthal angles of the photon in a system whose Z-axis is perpendicular to the photosphere. Photons with $\theta_o < 90°$ move away from the sun. We choose the initial energy of the photon, $\epsilon_o$ , such that photons are uniformly distributed in log $\epsilon_o$ space, and we then take into account the energy spectrum of the primary X-rays by assigning each

photon a weighted number proportional to its energy and the differential photon intensity at this energy. This procedure is more advantageous for two reasons than the direct generation of photons with a desired energy spectrum. First, in the latter procedure the photon count statistics decreases rapidly with increasing energy, while with the present method the photon count statistics remains similar in each logarithmically spaced energy bin. Second, with the present method we can get the results corresponding to initial photons with various energy spectra with only one computer run by simply assigning the appropriate weighting factors to each photon for various spectra.

Upon choosing the energy and the incident direction of the initial photon, the Stokes parameters of the photon ensemble are determined: For isotropic sources $P_1 = P_2 = 0$, and for anisotropic sources they are given by the result calculated by using equation (3.19).

The Compton scattering takes place at a columnar depth of about $10^{24}$ $cm^{-2}$, where the density is about $10^{17} cm^{-3}$ (e.g., Gingerrich et al. 1971) and the mean free path of the photon is of the order of $10^7$ cm. Because this depth is much larger than the chromospheric and photospheric irregularities, and because the height of the X-ray source is much smaller than one solar radius, throughout this thesis we assume that the photosphere is plane-stratified.

Since multiple scattering occurs, other than the initial incident direction and the initial photon energy, we need several parameters to characterize the photon: the present direction of propagation, the present energy, the present Stokes parameters, and the vertical depth at which the previous scattering took place. Since the position

of the photon interaction is expressed by the columnar depth, our calculation is independent of the solar atmospheric model, as far as the plane-stratified photosphere is assumed.

We choose the path length for the Compton scattering (in units of the hydrogen number per $cm^2$), $X_s$, and the path length for absorption, $X_a$, according to the cross sections given by equations (3.13) and (3.14), respectively. If $X_a < X_s$, the photon is absorbed. If $X_a > X_s$, the photon makes a Compton scattering. The scattering angles $(\theta_s, \phi_s)$ are chosen according to equation (3.11). The direction of the photon after the scattering is given by $(\theta_2, \phi_2)$, where

$$\cos\theta_2 = \cos\theta_1 \cos\theta_s - \sin\theta_1 \sin\theta_s \cos\phi_s, \tag{3.21}$$

$$\cos\phi_2 = (\cos\theta_1 \cos\phi_1 \sin\theta_s \cos\phi_s - \sin\phi_1 \sin\theta_s \sin\phi_s + \sin\theta_1 \cos\phi_1 \cos\theta_s)/\sin\theta_2, \tag{3.22}$$

$$\sin\phi_2 = (\cos\theta_1 \sin\phi_1 \sin\theta_s \cos\phi_s + \cos\phi_1 \sin\theta_s \sin\phi_s + \sin\theta_1 \sin\phi_1 \cos\theta_s)/\sin\theta_2. \tag{3.23}$$

Here $(\theta_1, \phi_1)$ are the direction of the photon before the collision. The energy of the photon after the scattering is given by equation (3.2). The vertical columnar depth at which the next interaction takes place is

$$X' = X - X_i \cos\theta_2 \tag{3.24}$$

where X is the vertical depth of the present scattering point, $X_i$ is the interaction path length, and $\cos\theta_2$ is given by equation (3.21). If $X'$ becomes a negative quantity for both absorption and Compton scattering, this means that the photon escapes from the photosphere.

We follow all the photons until they escape or are absorbed. Then, we collect the reflected photons according to their final energies, $\epsilon$, and the directions of motion, $(\theta, \phi)$, thereby defining a source function $Q'(\epsilon, \theta, \phi)$. The energy bins are logarithmically divided from 10 keV to 500 keV, and the angular bins are ten equally divided solid angle intervals. We generate enough photons so that in most of the bins the number of photons in one bin is larger than 100. In most cases except where the reflectivity is very small (such as $\theta \simeq 90°$, or very low energy bins or very high energy bins), the number of photons is several hundred. Therefore, one standard deviation error of the Poissonian statistics is about a few percent. We further reduce the magnitudes of the errors by fitting the calculated results with smooth curves both in energy space and in angular space.

## C. Backscatter, Anisotropy, and Spectral Characteristics of Solar Hard X-Rays

### 1. General Properties of Backscatter

To investigate the general properties of Compton scattering processes before undertaking complicated calculations, we deal with isotropically distributed monoenergetic photons with $\epsilon_0$ = 15 keV, 30 keV, 50 keV, and 100 keV, respectively. Twenty-seven per cent of the initial photons with $\epsilon_0$ = 15 keV are found to escape from the photosphere; 50%, with $\epsilon_0$ = 30 keV; 62%, with $\epsilon_0$ = 50 keV; and 68%, with $\epsilon_0$ = 100 keV. These escaped photons are classified according to their numbers of collisions and their final energies.

Figure 3.3 shows the distribution of the escaped photons as functions of number of collisions; Figure 3.4, as functions of final energy. At low energies the absorption is large and multiple scatterings are less important, because the absorption cross

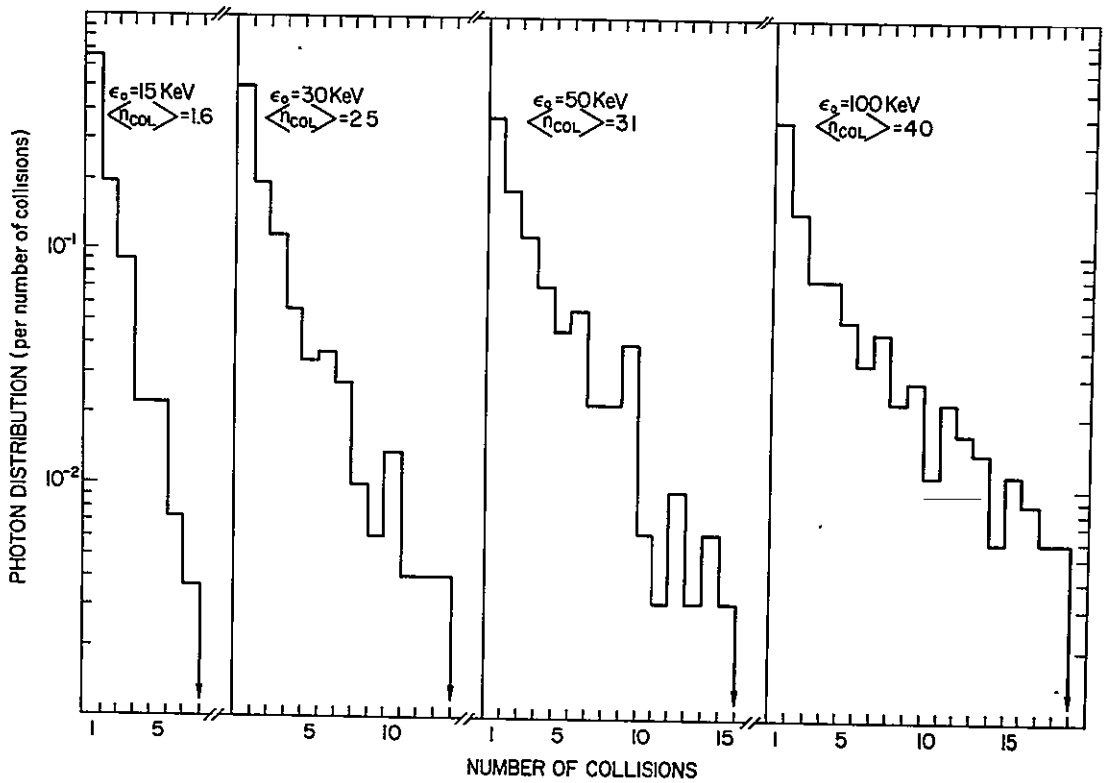


Figure 3.3. Distribution of photons escaped from the photosphere as a function of the number of collisions.

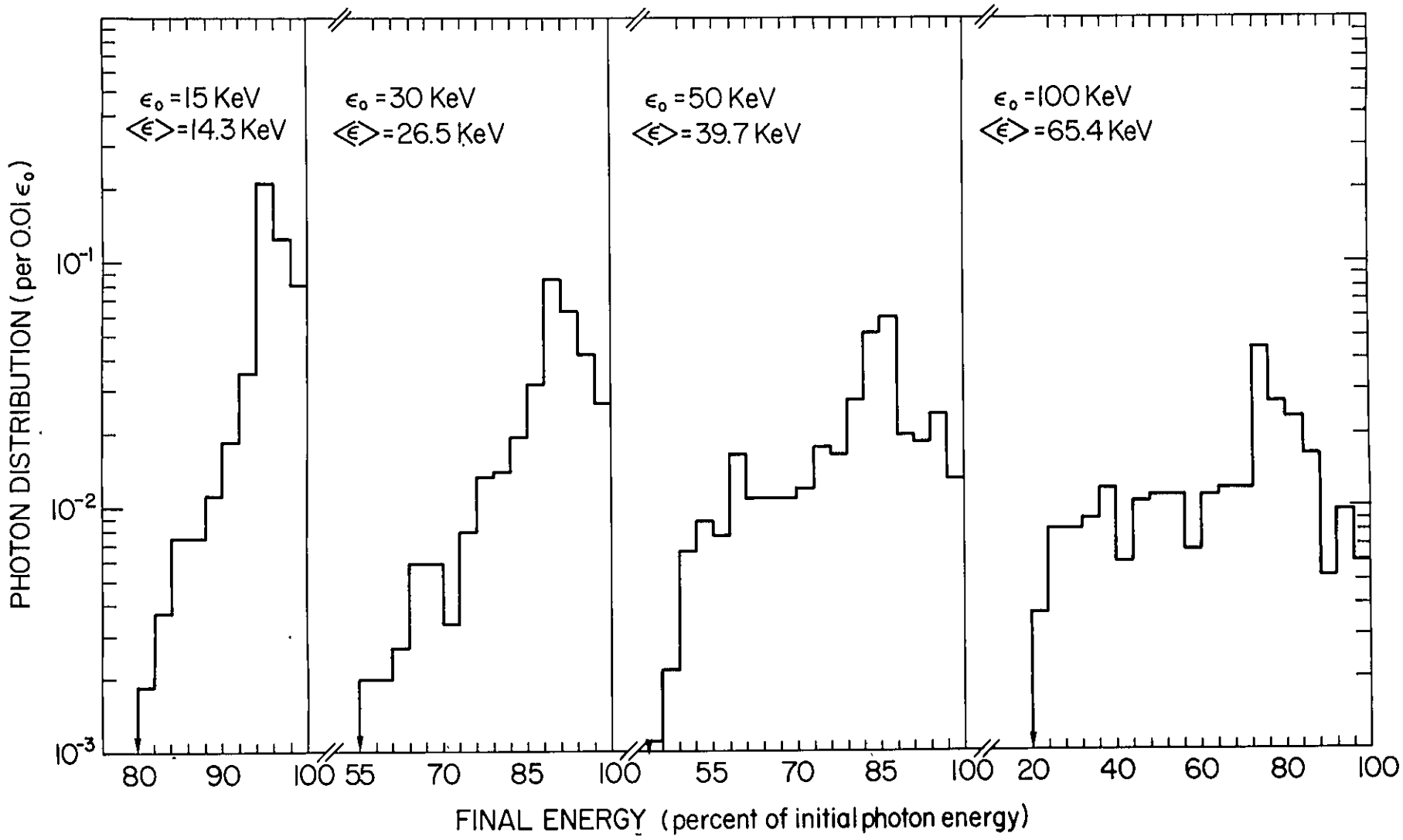


Figure 3.4. Distribution of photons escaped from the photosphere as a function of final energy.

section is larger at low energies than at higher energies. Because the total Compton cross section is smaller at higher energies than at lower energies, and because the differential cross section is large at small $\theta_s$, higher energy photons go deeper into the photosphere and undergo many scatterings. Because of the multiple scatterings and because of large recoil energy of the colliding electron, higher energy photons lose significant fractions of their initial energies. Also because of multiple scatterings and because of energy degradation toward the region where the absorption cross section is larger, about one third of photons with $\epsilon_o$ = 50 keV and 100 keV are absorbed even though at these energies absorption cross section is negligibly small.

## 2. The Albedo of Isotropic Sources

For the calculations of this section, we use isotropic and unpolarized primary photon sources. We consider power-law sources given by

$$Q(\epsilon) = A\epsilon^{-s} \text{ (photons sr}^{-1}\text{ sec}^{-1}\text{ keV}^{-1}), \tag{3.26}$$

and optically thin thermal sources given by (e.g., Holt 1974)

$$\begin{aligned} Q(\epsilon) = {} & 2.41 \times 10^{-16}\, g(T, \epsilon) Z^2 n_e n_i V \\ & \times (kT)^{-3/2} (\epsilon/kT)^{-1} \exp(-\epsilon/kT) \left(\frac{\text{photons}}{\text{sr-sec-keV}}\right), \end{aligned} \tag{3.27}$$

where $\epsilon$ and kT are in keV, Z is the atomic number of the medium, $n_e$ and $n_i$ are the electron and ion densities, V is the volume of the emitting source, and $g(T, \epsilon)$ is the Gaunt factor (Karzas and Latter 1961).

The observed photon spectrum consists of the sum of the initial photons and the reflected photons: $Q_T(\epsilon, \theta, \phi) = Q(\epsilon, \theta, \phi) + Q'(\epsilon, \theta, \phi)$, where $Q'(\epsilon, \theta, \phi)$ is the reflected photon spectrum. Notice here that the initial energies of the reflected photons

observed at the energy $\epsilon$ must be larger than $\epsilon$. We define the differential reflectivity for an isotropic source as

$$R(\epsilon, \theta, \phi) = Q'(\epsilon, \theta, \phi)/Q(\epsilon) \tag{3.28}$$

With this definition, the observed photon spectrum is expressed as $Q_T(\epsilon, \theta, \phi) = [1 + R(\epsilon, \theta, \phi)]\, Q(\epsilon)$. The integral reflectivity is given by

$$\bar{R}(\epsilon) = (2\pi)^{-1} \int_0^{2\pi} d\varphi \int_0^1 d(\cos\theta)\, R(\epsilon, \theta, \varphi). \tag{3.29}$$

Figure 3.5 shows the integral reflectivities of isotropic sources with power-law and thermal spectra. As can be seen, the reflectivity is maximum around 30 keV. The integral reflectivity is determined by three effects. The first is absorption due to the photoelectric effect. At lower energies the reflectivity is reduced mainly because of absorption. However, even at $\epsilon_0 = 100$ keV, one third of the incident photons are absorbed as was mentioned earlier. The second is energy degradation. At higher energies the reflectivity decreases due mainly to this effect, and because of this fact the reflectivity at higher energies is larger for flatter spectra. The third effect is the compression in energy space which is caused by the fact that the energy degradation becomes larger with the increase of energy. This effect makes the reflectivity larger, and because of this effect the integral reflectivity at 30 keV for s = 2 is larger than 0.5 even though only 50% of the photons incident with $\epsilon_0 = 30$ keV escape from the photosphere.

Figure 3.6 shows the differential reflectivity for three values of $\theta$ and three incident photon spectra. (Here $\theta$ is the polar angle of the reflected photon in the point of view of the source, and is the heliocentric angle of the source in the point of view

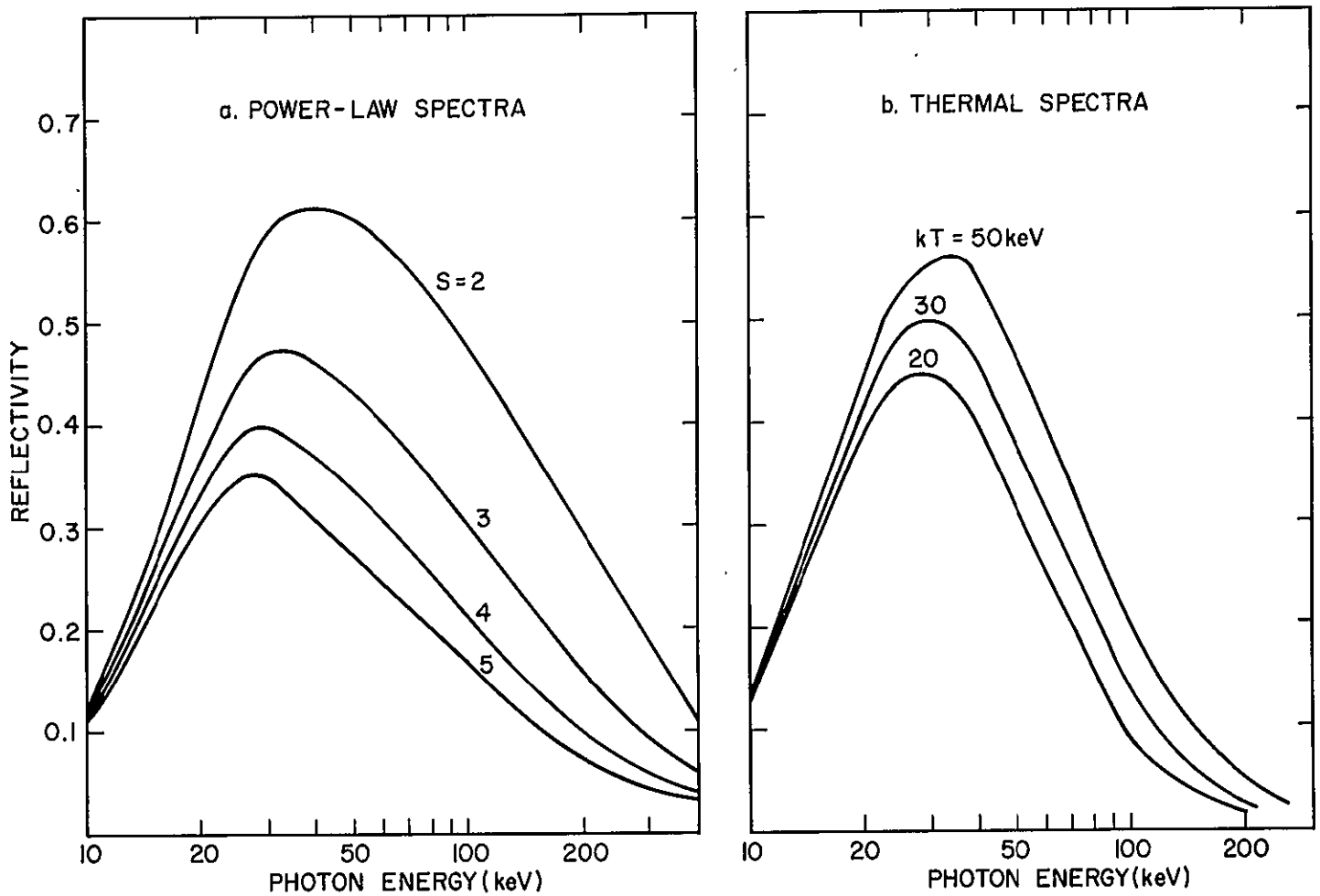


Figure 3.5. Integral reflectivities of isotropic X-ray sources. The reflectivity is defined in equations 3.28 and 3.29.

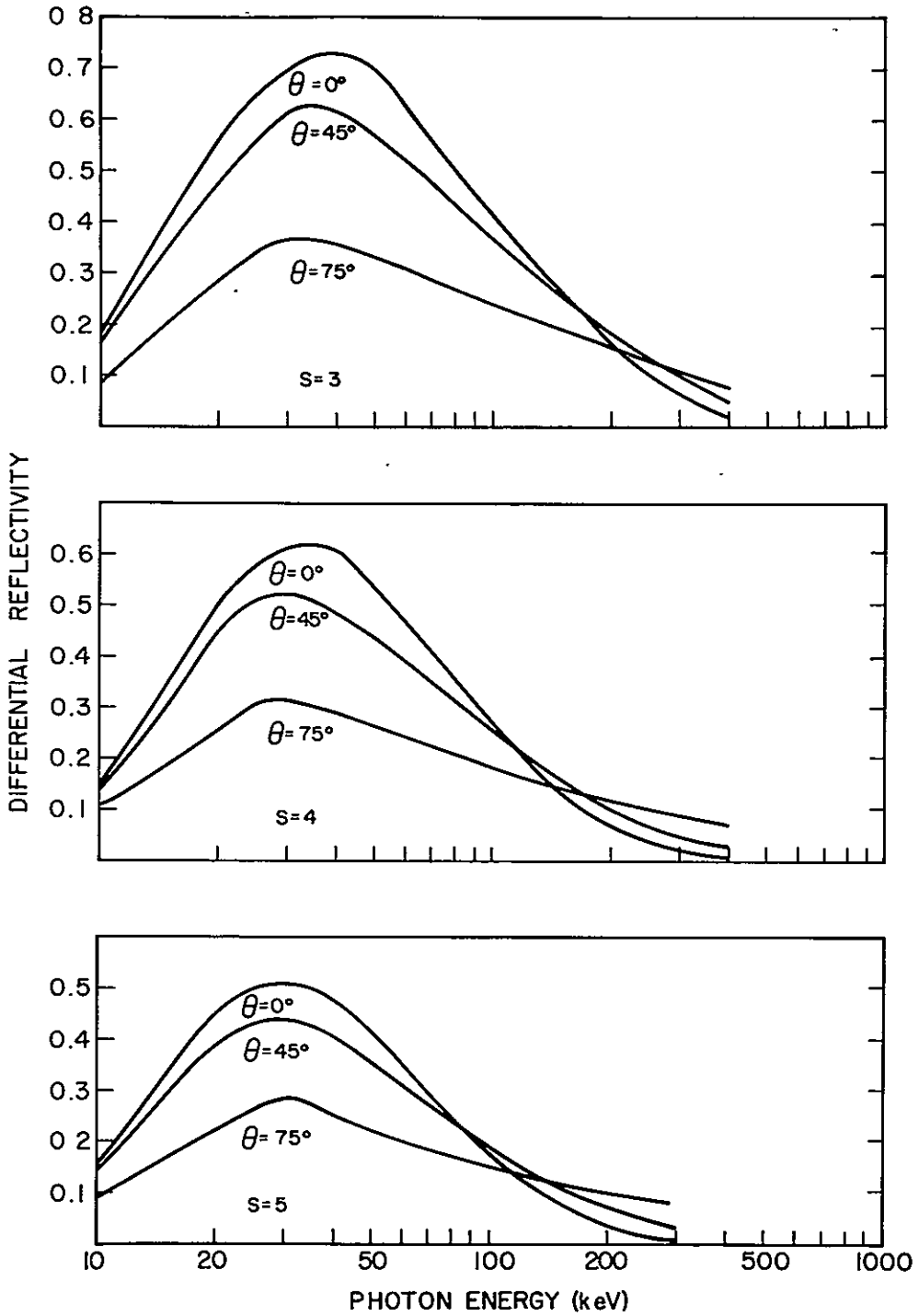


Figure 3.6. Differential reflectivities of isotropic sources with power-law spectra.

of the observer.) As can be seen, below $\sim 250$ keV the reflectivity is larger at smaller values of $\theta$, because the amount of matter traversed is smaller in these cases. The trend is reversed at higher energies, because at these energies the cross section for large angle scattering is small.

The idea that solar hard X-rays are produced by hot thermal electrons began to gather new interest recently (Colgate, Audouze and Fowler 1977). In Figure 3.7 we show the total (primary and reflected) photon spectrum of thermal X-ray sources for kT = 20 and 30 keV and two directions of observation. As can be seen, even though the total spectra are somewhat steeper than the primary spectra, they can be approximated by single power laws only in narrow energy ranges.

## 3. Anisotropic Sources

For the anisotropic sources, we assume that X-rays are produced by accelerated electrons with momentum vectors uniformly distributed in a cone of 30° half opening angle centered around the downward vertical vector. The distribution function of the momentum vectors of such electrons is

$$g(\theta') = \begin{cases} 1/[2\pi(1 - \cos 30^\circ)] & \text{for } 150^\circ \leq \theta' \leq 180^\circ \\ 0 & \text{otherwise,} \end{cases} \tag{3.30}$$

where $\theta'$ is the polar angle measured from the normal to the plane-stratified photosphere. Though a unidirectional beam of electrons is easier to deal with, we introduce the finite dispersion of the velocity vectors of the electrons for the following reasons: (1) The electrons will have finite pitch angles. (2) The magnetic field lines guiding the electrons are not expected to be exactly straight or vertical. (3) As discussed by Brown (1972), collisions of the electrons with ambient particles cause the dispersion of the pitch angles. We also assume that the instantaneous electron energy spectra are power laws with power-indexes 2.5 and 3.5.

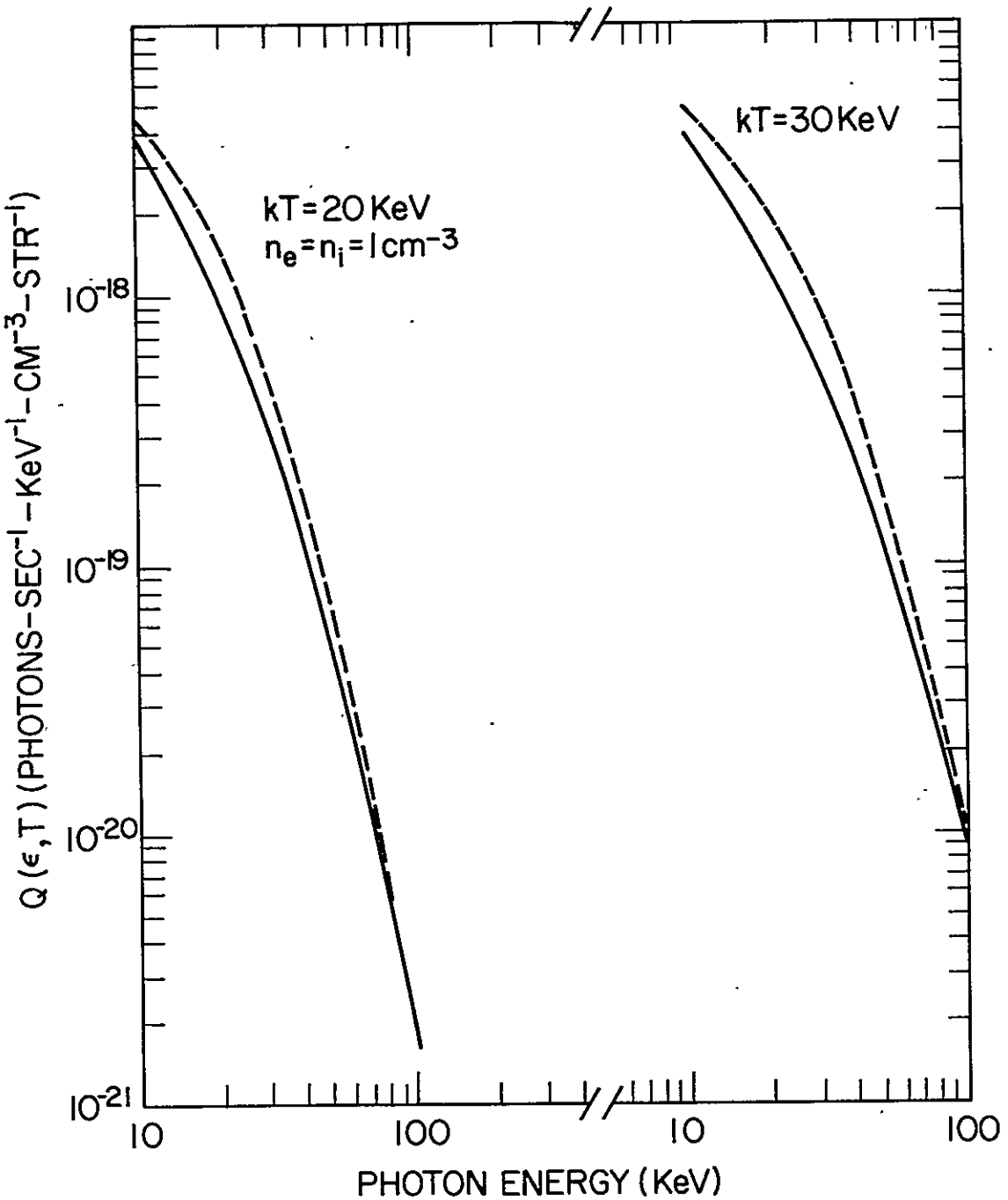


Figure 3.7. Photon spectra due to a thermal hydrogen plasma with $n_e = n_i = 1$ cm$^{-3}$, and kT = 20 keV and kT = 30 keV. The resultant spectra (including the reflected component) seen at $\theta = 0°$ are shown by the dashed lines. The solid lines indicate the original spectrum.

Using the equations (3.17), and using equation (2.11) for the differential cross section (non-screened), equation (3.30) for the distribution function, and $N(E) \sim E^{-2.5}$ for the electron spectrum, we calculate the X-ray production rate, $Q(\epsilon, \theta)$, for various values of $\epsilon$ and $\theta$. Similarly we also calculate the degree of polarization, $P_1(\epsilon, \theta)$, by using equations (3.19), (2.15) and (2.16). The degree of polarization is plotted in Figure 3.8, and the X-ray production rates are shown by solid lines in Figure 3.9. In this figure, 90° corresponds to X-ray emission from the solar limb and 0° to emission from the disk center. Without the reflection of the X-rays, there would be a large limb brightening and a slight limb flattening of the photon spectra. Similar results were obtained by Brown (1972) and by Petrosian (1973).

Using the Monte Carlo simulation described in the preceding section, we calculate the backscatter of the photons whose polarization and spectrum and angular distribution are shown in Figures 3.8 and 3.9, respectively. The dashed lines in Figure 3.9 show the resultant total photon production rates including the primary and reflected sources. Similar calculations were performed for the electron spectrum $N(E) \sim E^{-3.5}$. The results are shown in Figures 3.10 and 3.11, similarly to Figures 3.8 and 3.9.

As can be seen in Figures 3.8 and 3.10, for the anisotropic model we use, the degree of polarization of the primary X-rays is very large, especially at low photon energies and near 90°. The degree of polarization of the hard X-rays observed near the earth, however, will be modified due to the dominant backscattered component. The degree of polarization including the backscattered component will be studied in the next section.

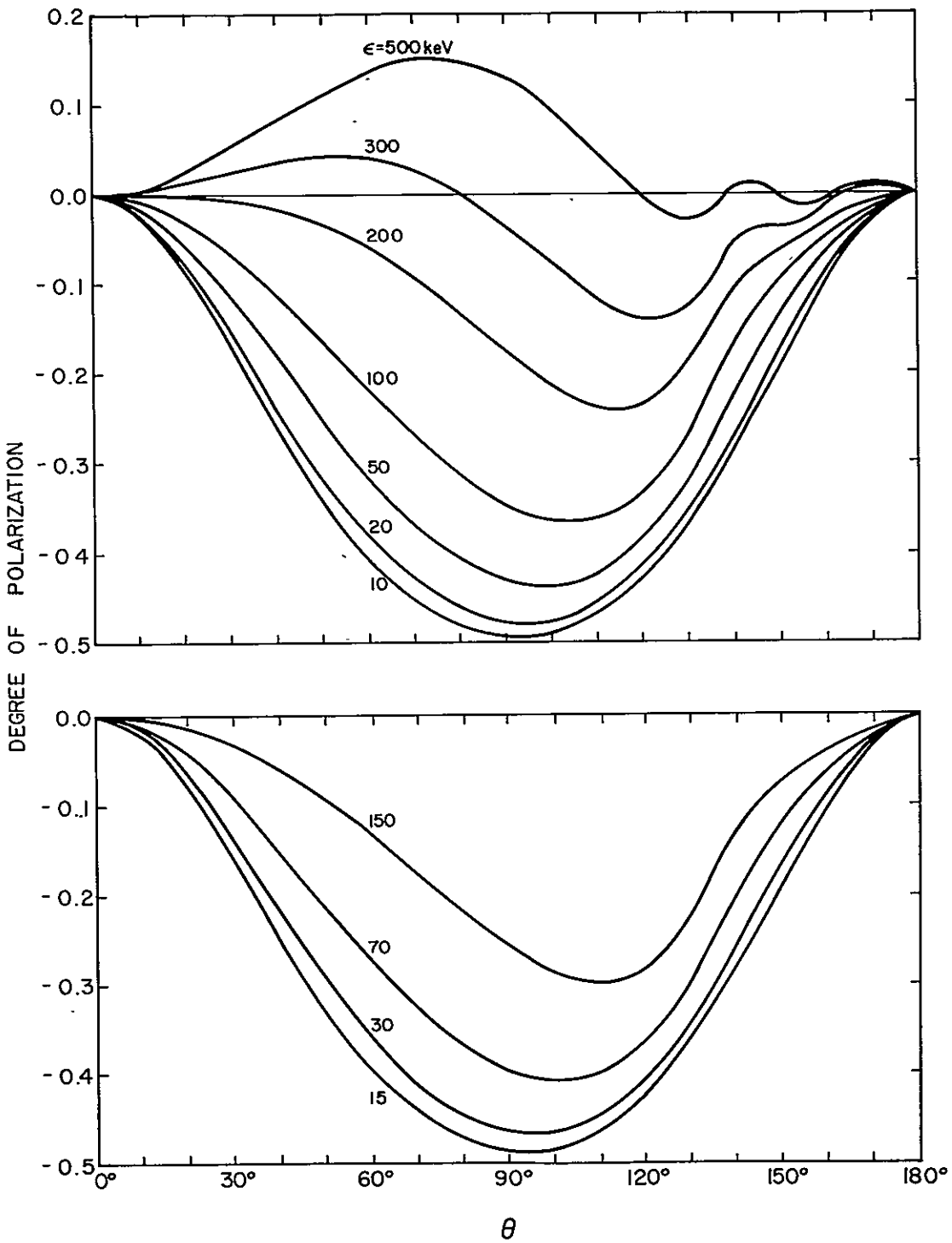


Figure 3.8. The degree of polarization of primary hard X-rays due to the accelerated electrons moving toward the photosphere with velocity vectors uniformly distributed in a cone with half opening angle 30° and centered at the vertical to the photosphere. The spectrum of the accelerated electrons is $E^{-2.5}$. The negative values mean that the direction of polarization is along the normal plane.

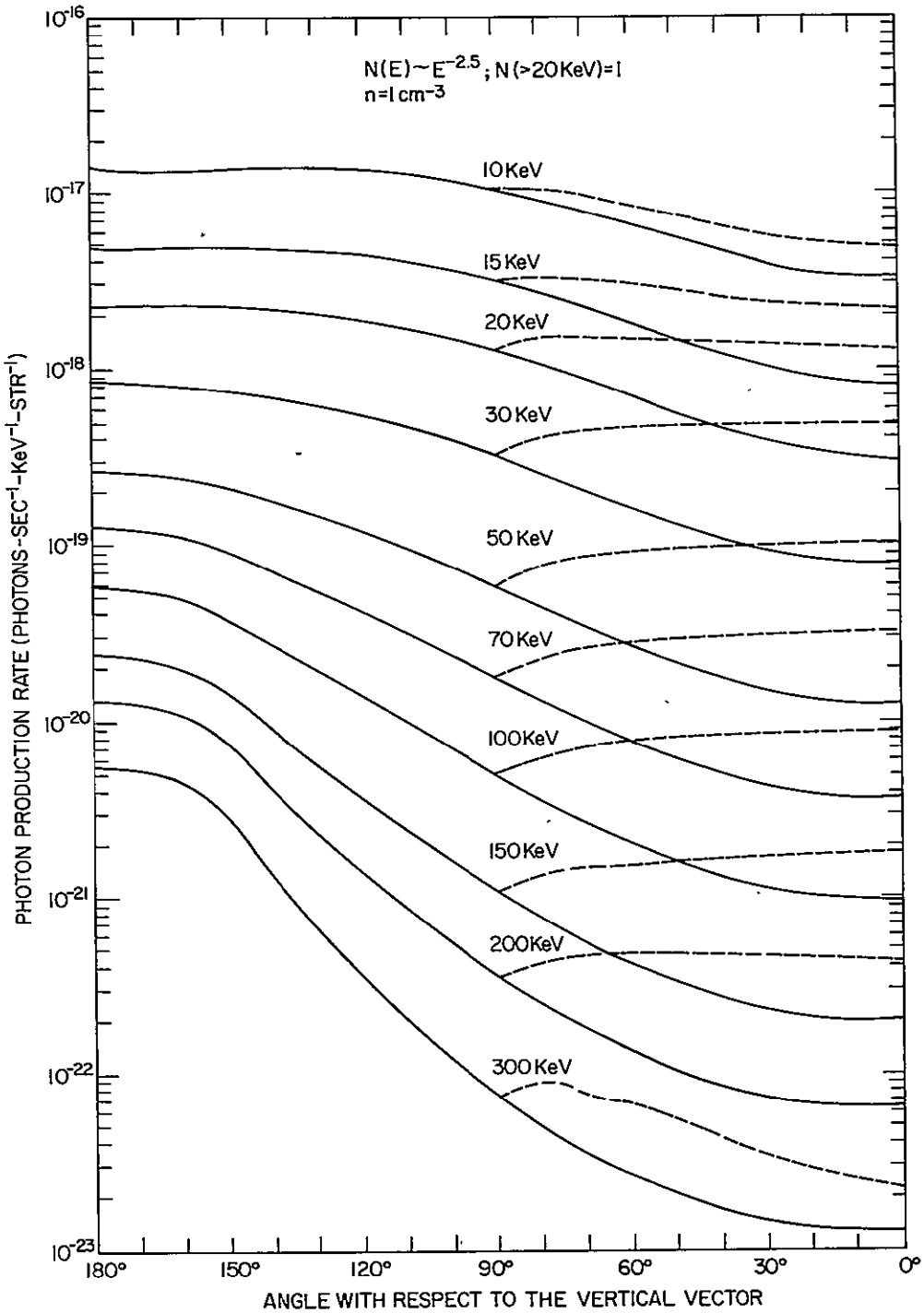


Figure 3.9. Primary X-ray intensities due to the same electrons as in the above. The solid lines represent primary photon intensities and the dashed lines represent the sum of the primary and reflected photons.

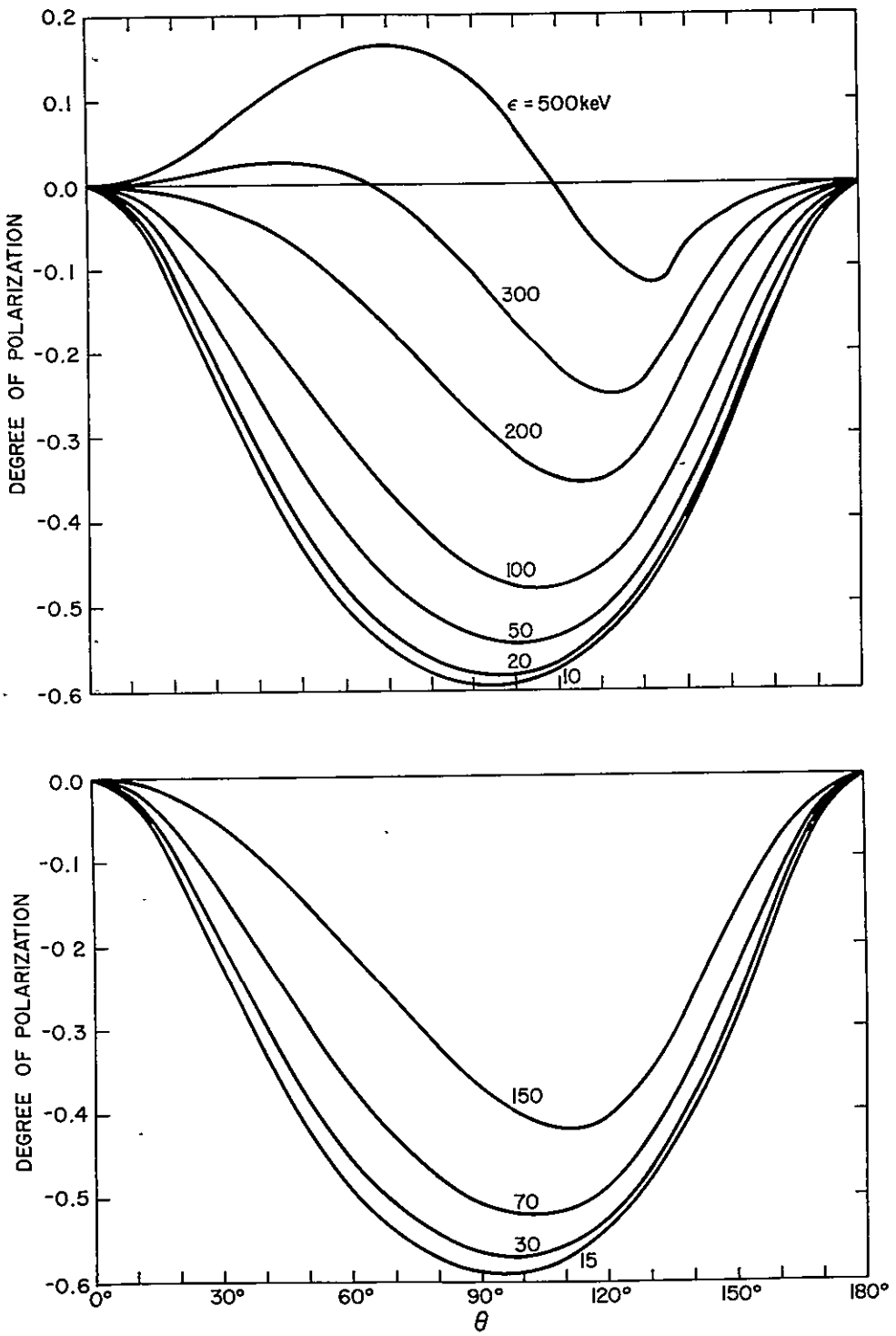


Figure 3.10. Same as Figure 3.8, except that the electron spectrum is $E^{-3.5}$.

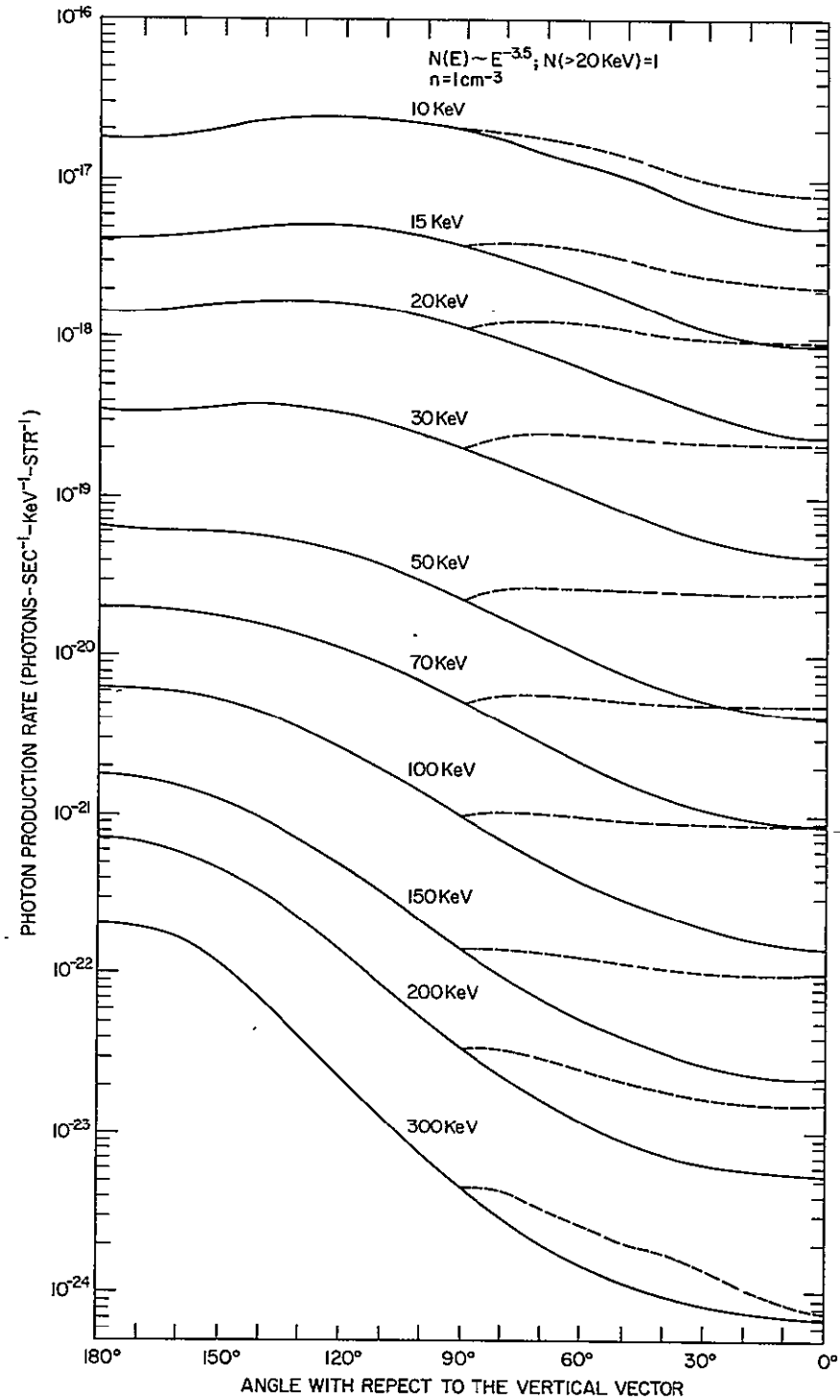


Figure 3.11. Same as Figure 3.9, except that the electron spectrum is $E^{-3.5}$ .

As can be seen in Figures 3.9 and 3.11, the limb brightening effect has almost disappeared except at very low energies or at very high energies where the reflectivity is small (Figure 3.5). Henoux (1975) also reported similar results. Therefore, the anisotropic model in which electrons are moving toward the photosphere is not contradictory to the observational results of Datlowe et al. (1974, 1977) when the reflected component is properly taken into account. Therefore, the lack of limb brightening effect does not rule out the possibility that the accelerated electrons move predominantly down towards the photosphere; this interpretation is contradictory to that of Datlowe et al. (1974, 1977).

Figure 3.12 shows the photon spectra due to anisotropic sources, taken from Figures 3.9 and 3.11 for several observation angles. Even though over the entire energy range the photon spectra deviate from power laws, in the 15 to 50 keV they can be reasonably well approximated by a single power law. Similar approximations can be made for the isotropic power-law sources. The resultant spectral indexes for this energy range are shown in Table 3.1. As can be seen, for the isotropic sources, the spectral index does not change appreciably with heliocentric angle because reflection is not the dominant source of photons in this case. On the other hand, for the anisotropic sources the photon spectrum steepens as the heliocentric angle increases, a fact that can account for the result of Datlowe et al. (1974) who found that the average spectral index (in the 17 to 45 keV range) of limb flares is larger by about 0.5 than that of disk flares.

Another characteristic of the spectra shown in Figure 3.12 is that for flares near the disk center the spectra steepen as energy increases, but this character is less pronounced for limb flares (see Table 3.2). Therefore, if the accelerated

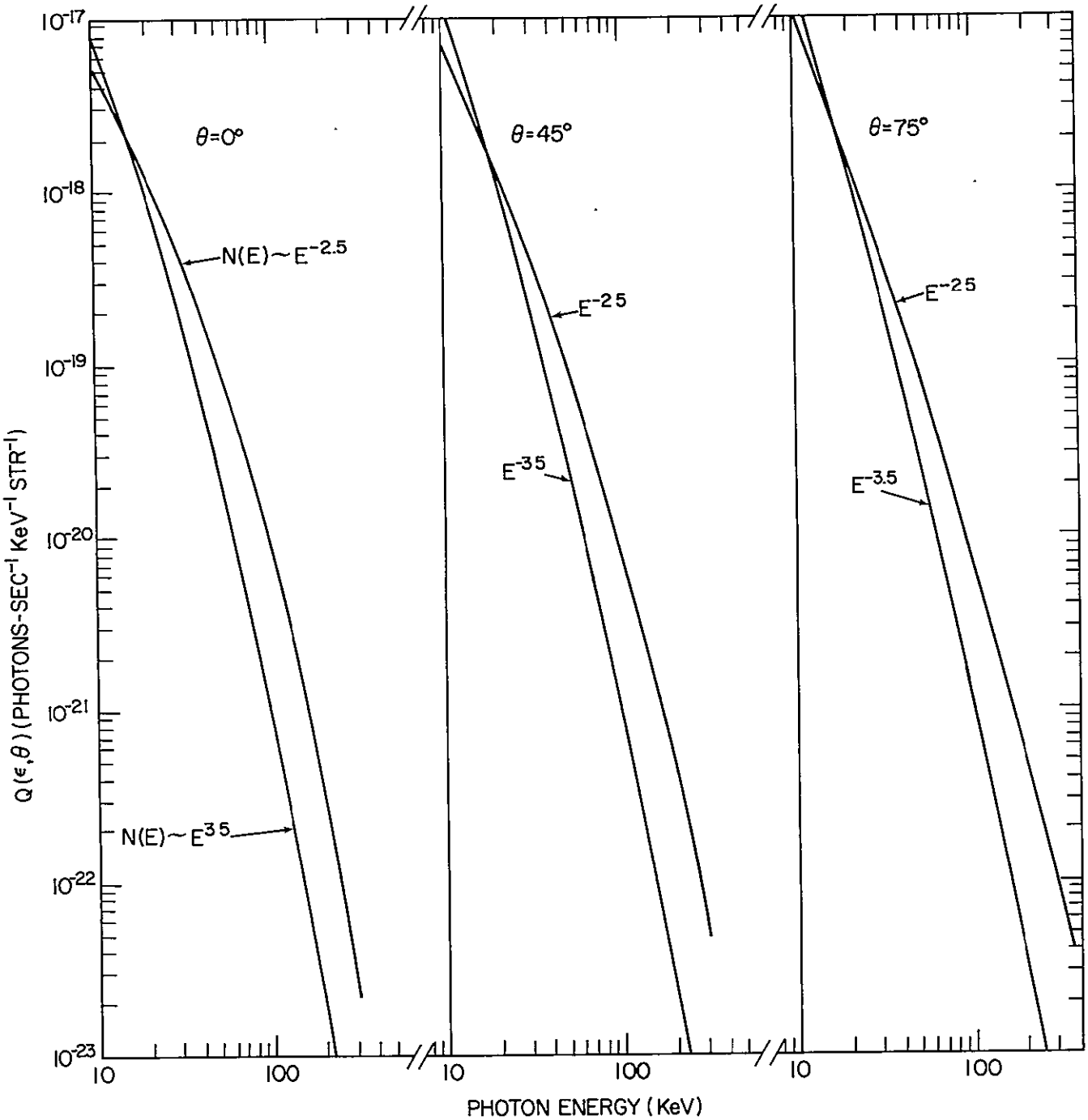


Figure 3.12. Photon spectra taken from the results of Figures 3.9 and 3.11; $\theta$ is the angle between the direction of observation and the normal to the photosphere.

Table 3.1

Spectral Indexes of Photon Spectra in the Range from 15 keV to 50 keV

(a) Isotropic Photon Sources with Power-law Spectra

| Original Photon Spectral Index | $\theta$ 0° | 45° | 75° |
|---|---|---|---|
| 2 | 1.76 | 1.78 | 1.88 |
| 3 | 2.84 | 2.87 | 2.94 |
| 4 | 3.94 | 3.96 | 3.95 |
| 5 | 4.99 | 4.97 | 4.97 |

(b) Anisotropic Sources

| Spectral Index of the Electrons | $\theta$ 0° | | 45° | | 75° | |
|---|---|---|---|---|---|---|
| | No Reflection | Reflection | No Reflection | Reflection | No Reflection | Reflection |
| 2.5 | 3.48 | 2.56 | 3.52 | 2.77 | 3.40 | 3.05 |
| 3.5 | 4.44 | 3.73 | 4.49 | 3.95 | 4.39 | 4.11 |

Table 3.2

Spectral Indexes of Photon Spectra in the Range from 100 to 300 keV for the Anisotropic Cases

| Spectral Index of the Electrons | $\theta$ | | |
|---|---|---|---|
| | 0° | 45° | 75° |
| 2.5 | 5.40 | 4.65 | 3.95 |
| 3.5 | 6.44 | 5.61 | 5.12 |

electrons in flares move predominantly downward, the spectra measured at energies $\gtrsim 100$ keV will show a limb flattening in contrast to the spectra measured at energies $\lesssim 50$ keV. This may be tested in future experiments. If the steepening of the spectrum at energies $\gtrsim 100$ keV is larger for flares near the disk center than for flares near the limb, it can be regarded as a supporting evidence for the anisotropic model. The spectral characteristics up to 300 keV will be available from the measurements of the Hard X-ray spectrometer (Frost 1976) which is going to be included in the payload of NASA's SMM.

## D. Compton Backscatter and Polarization

As we have seen in Section C, for the anisotropic model in which accelerated electrons move downward, the backscattered component dominates the observed flux except flares very close to the limb. For an isotropic source, the backscattered component constitutes a small fraction of the observed flux. However, the backscattered photons are polarized due to the polarization dependence of the Compton scattering cross section. Therefore, in calculation of the polarization of solar hard X-rays, we have to take the effect of the backscatter on the polarization into account properly. In calculations of the polarization until now, however, the effect of Compton backscatter was not considered except by Henoux (1975) and by Langer and Petrosian (1977).

Even though in the calculations of the preceding section the polarization of the photon was followed throughout the scattering process, the polarization of the backscattered photons was not recorded. To calculate the degree of polarization of the backscattered photons, we need better count statistics. Using the Monte Carlo simulation described in Section B, we have calculated the degree of polarization due to the Compton backscatter of isotropic monoenergetic photon sources with $\epsilon_0 = 15$ keV

and $\epsilon_0$ = 30 keV, by generating 4 $\times 10^4$ photon ensembles for each case. Here we use monoenergetic sources in order not to worry about the effect of energy degradation and the spectral dependence of the reflectivity. Figure 3.13 shows the result. Here the polarization is parallel to the normal plane. The dashed lines represent the degree of polarization of the reflected photons only, and the solid lines represent the degree of polarization of the sum of the reflected and the primary photons. The dotted line shows the degree of polarization of the single-scattered photons only, which can be calculated analytically (Appendix C). This result is consistent with the result of the Monte Carlo simulation.

As can be seen in this figure, the degree of polarization of the sum of the reflected and the primary unpolarized photons is less than 4%. This result is consistent with the result by Henoux (1975) and Beigman (1973). In contradiction to the above result, Brown, McClymont, and McLean (1974) argued that the polarization due to an isotropic unpolarized primary source might be quite large because of the backscattered component; however, they did not perform an actual calculation.

Figure 3.14 shows the degree of polarization due to backscatter of an anisotropic primary source, whose angular distribution function and degree of polarization are given in Figure 3.10 and Figure 3.11, respectively. Here the polarization is also parallel to the normal plane. The dashed lines show the degree of polarization of the photon flux due to the primary source only and that due to the scattered photons only, respectively. The solid lines show the degree of polarization of the sum of the primary photons and the reflected photons. For this evaluation, we use the relative contribution of the reflected photons and that of the primary photons shown in Figure 3.9. As can be seen, for such an anisotropic model, the degree of

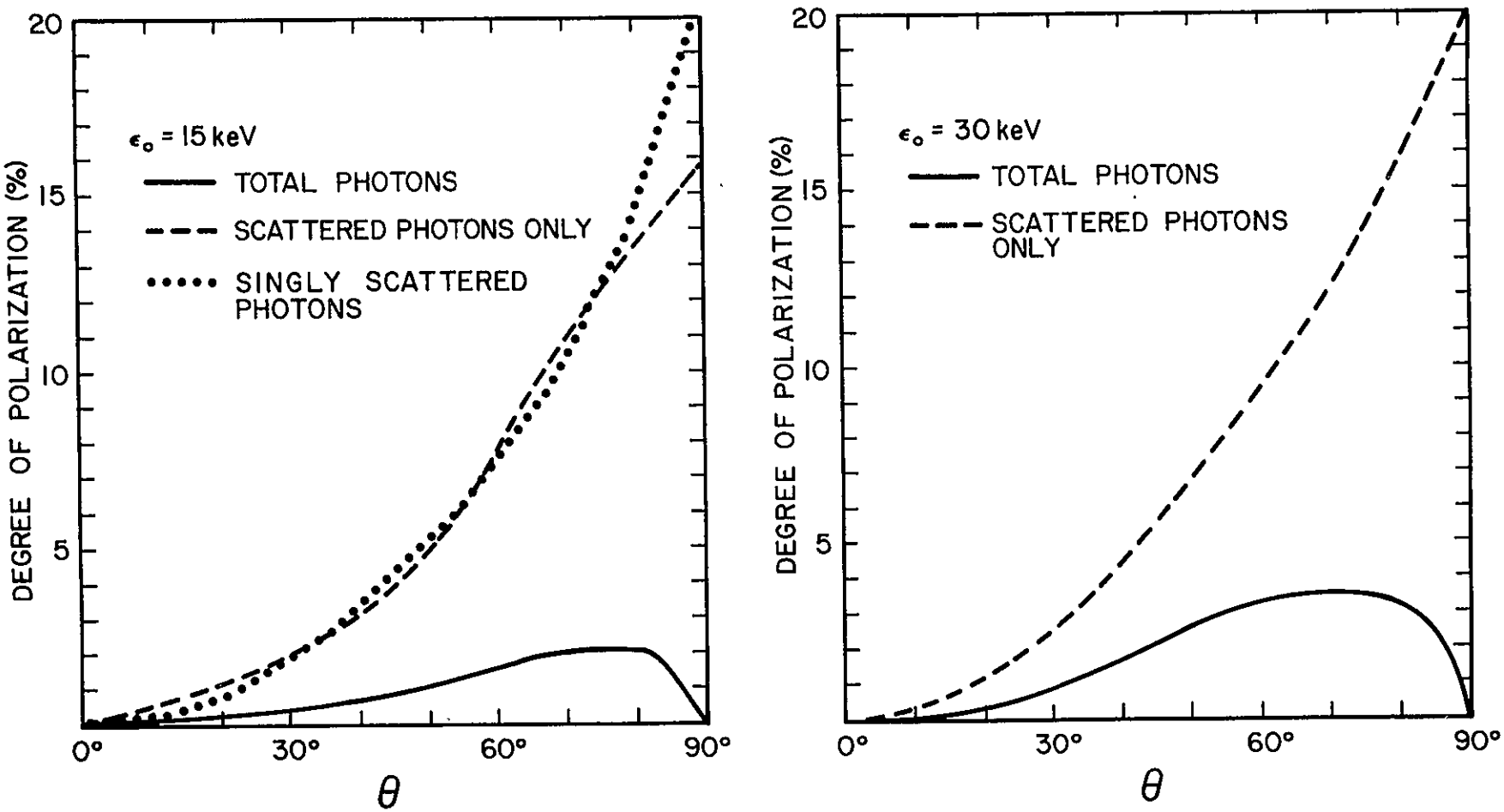


Figure 3.13. Degree of polarization due to Compton backscatter of unpolarized isotropic primary photons. The dashed lines represent the degree of polarization of the scattered photons only, and the solid lines represent the degree of polarization of the sum of the primary and reflected photons. The direction of polarization is along the normal plane.

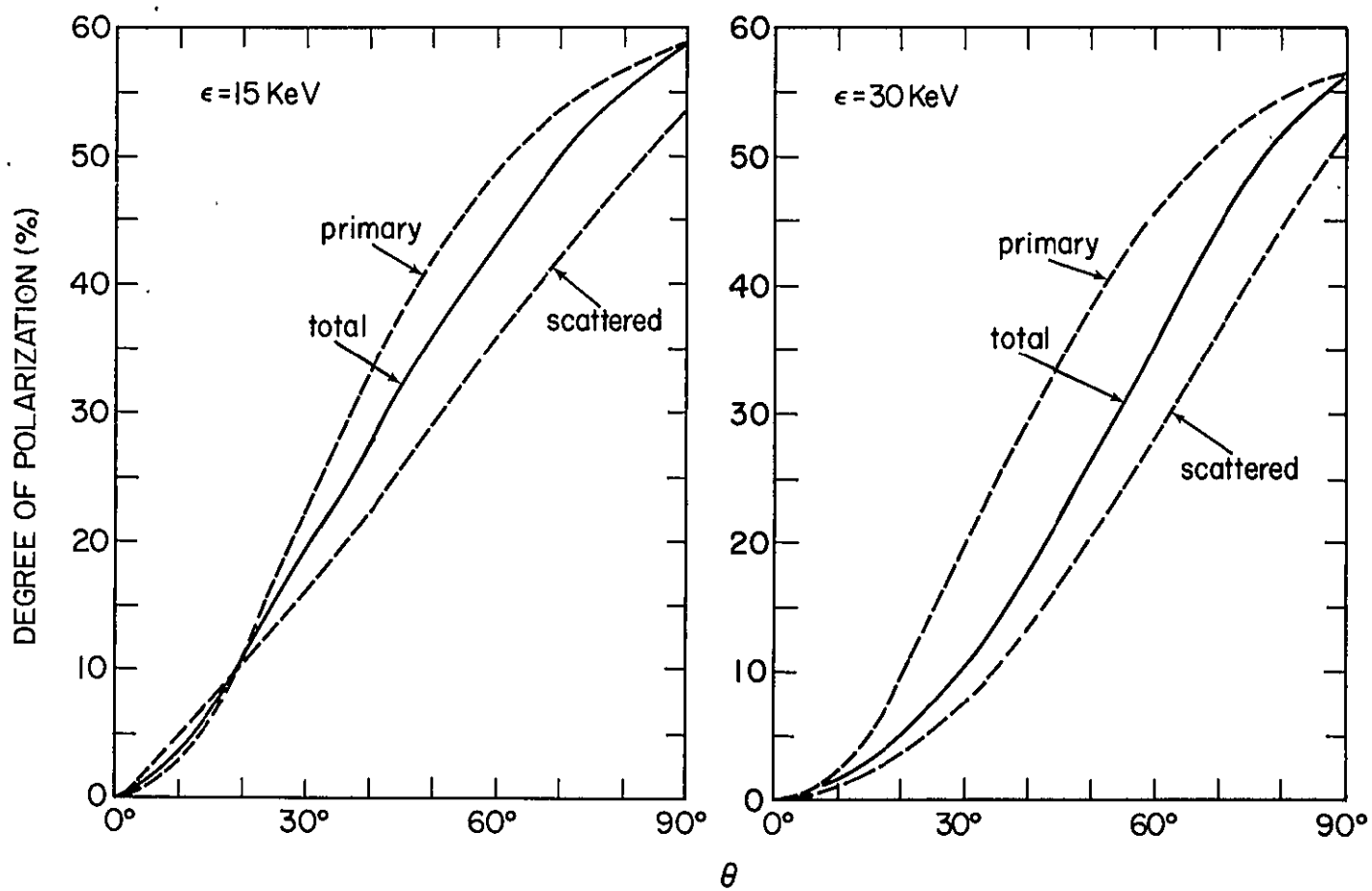


Figure 3.14. Degree of polarization of photons due to anisotropic electrons, where the angular distribution of the electrons is

$$g(\theta) = \begin{cases} \text{const} & \text{for} \quad 150^\circ < \theta < 180^\circ \\ 0 & \text{for} \quad \theta < 150^\circ. \end{cases}$$

polarization is very large for flares far from the disk center. It is about 60% at $\theta = 90°$, and decreases monotonically to zero at $\theta = 0°$.

To see the effect of the angular dispersion of the momentum vectors of the accelerated electrons producing hard X-rays, we made a similar calculation for an anisotropic model where the electron momentum vectors are distributed uniformly in a cone with half-opening angle 60° centered around the vertically downward direction. The result is shown in Figure 3.15. Here the degree of polarization is less than the result in Figure 3.14, as expected because of a larger dispersion of the momentum vectors. However, in this case also, the degree of polarization is substantial. Note that the similarities of the degree of polarization for two energies (Figures 3.13 through 3.15) justifies the calculation of polarization using mono-energetic sources.

## E. Characteristics of the Albedo Patch

The Compton scattering by the photosphere backscatters a large fraction of the incident photons above 10 keV, which could not be observed otherwise. Thus, the backscattered photons, if they are resolved from the primary photons, can give extra information on the properties of the primary X-ray source. Easiest of all, we can get information on the degree of the anisotropy of the primary source by comparing the number of photons directly coming from the bright primary source and that from the nebulous albedo patch. If the height of the primary source is larger than its size, such information can be easily obtained from measurements by instruments with spatial resolution smaller than the size of the primary source. If the albedo brightness distribution is measured in detail, we can get more detailed information on the angular distribution of the primary X-ray emission and also on the height of the primary source.

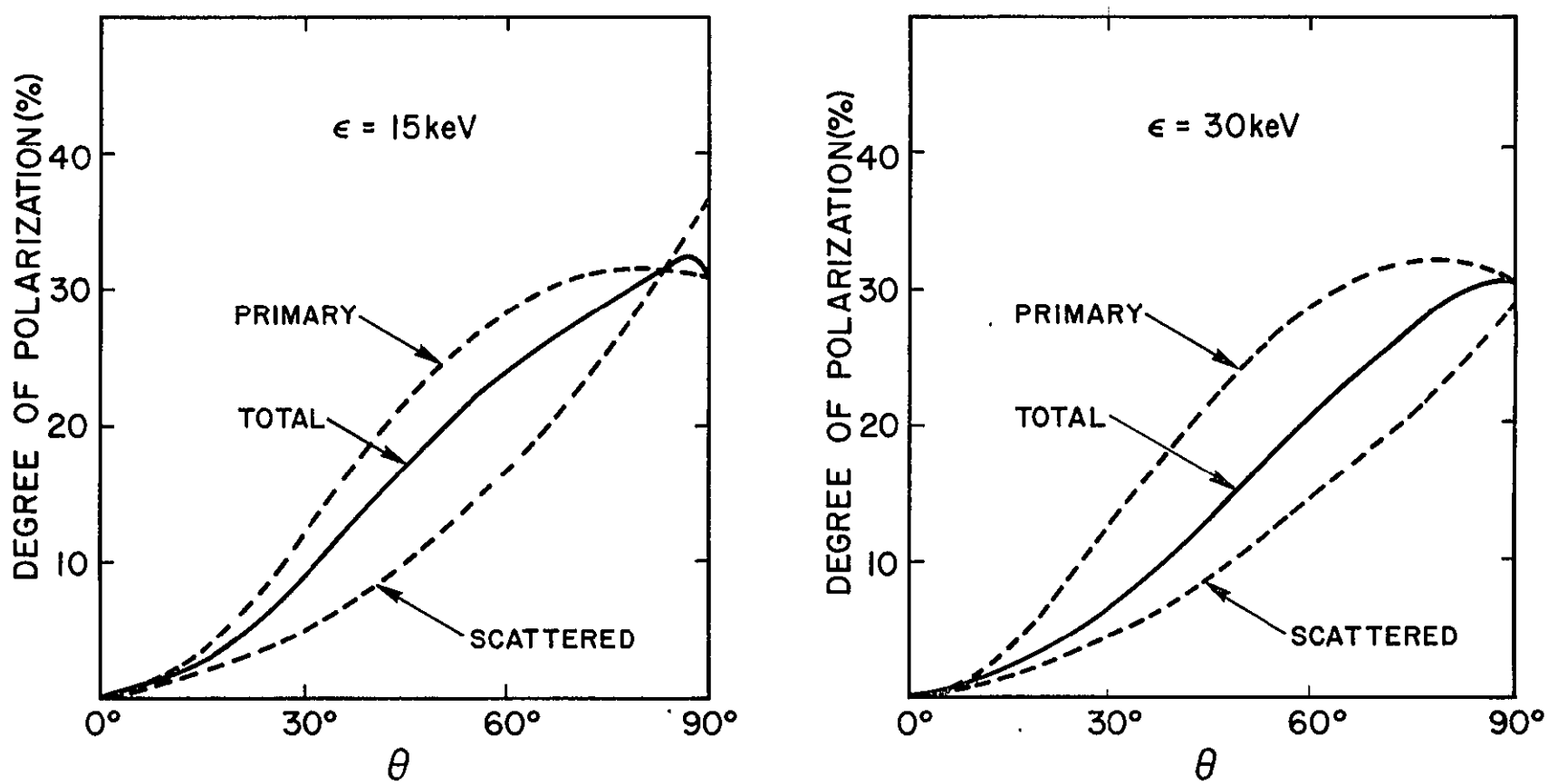


Figure 3.15. Same as Figure 3.14, except that

$$g(\theta) = \begin{cases} \text{const} & \text{for} \quad 120^\circ < \theta < 180^\circ \\ 0 & \text{for} \quad \theta < 120^\circ. \end{cases}$$

In this section we investigate the characteristics of the albedo patch, which is a bright X-ray patch on the photosphere created by the Compton backscatter. In this section we assume that the primary source is a point source. An extended primary source can be regarded as a superposition of many point sources, and in principle the albedo brightness distribution of an extended source can be obtained from the result for a point source. A more detailed discussion on extended sources is given in the next chapter.

The surface brightness of the albedo patch (measured in photons $sr^{-1}$ $cm^{-2}$ $sec^{-1}$) observed at an angle $\theta$ in the energy interval from $\epsilon_1$ to $\epsilon_2$ is proportional to the number of photons incident upon unit area and their probability of reflection (for the geometry, see Figure 3.16):

$$I(\epsilon_1 \sim \epsilon_2, \theta, \ell, \phi) = \overline{Q}(\epsilon_1 \sim \epsilon_2, \theta_o, \phi) \left\{2\pi h^2 \left[(\ell/h)^2 + 1\right]^{3/2}\right\}^{-1} \cdot R(\epsilon_1 \sim \epsilon_2, \theta_o, \theta, \phi). \tag{3.31}$$

Here the first factor, $\overline{Q}(\epsilon_1 \sim \epsilon_2, \theta_o, \phi)$, represents the angular distribution of the incident photons in the energy interval $\epsilon_1 \sim \epsilon_2$, the second factor relates a unit solid angle to the area on the photosphere where h is the height of the source and $\ell = -h \tan \theta_o$, and $R(\epsilon_1 \sim \epsilon_2, \theta_o, \theta, \phi)$ is the differential reflectivity of a beam of photons. It is defined as

$$R(\epsilon_1 \sim \epsilon_2, \theta_o, \theta, \phi) = \frac{2\pi \int_{\epsilon_1}^{\epsilon_2} d\epsilon Q'(\epsilon, \theta, \phi)}{\int_{\epsilon_1}^{\epsilon_2} d\epsilon Q_{\theta_o}(\epsilon)} \tag{3.32}$$

where $Q_{\theta_o}(\epsilon)$ represents a beam of primary photons incident at $\theta_o$, and $Q'(\epsilon, \theta, \phi)$ is the photon source due to reflection. Equation (3.31) implicitly assumes that the photon

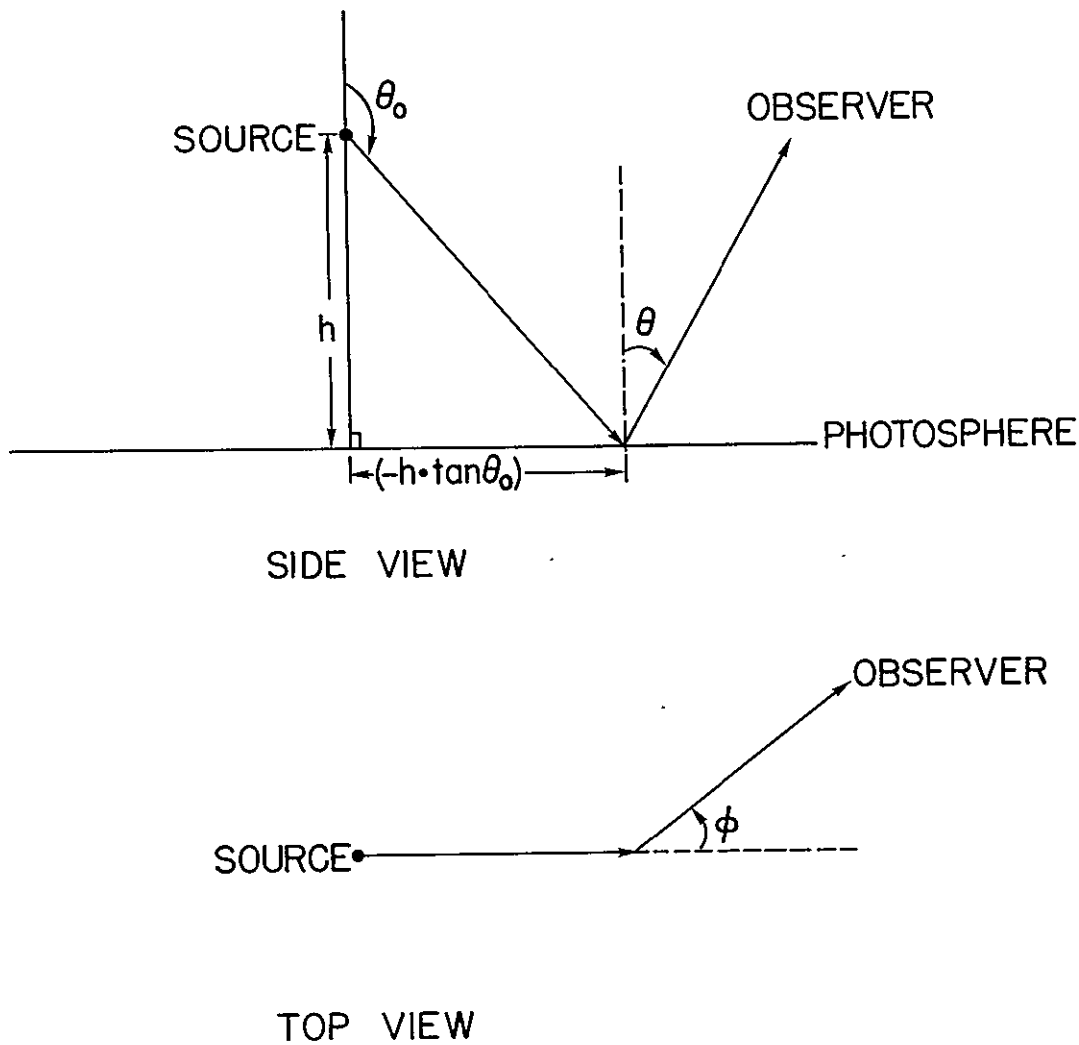


Figure 3.16. A schematic drawing of the geometry of the scattering. The angle $\theta$ is the angle of observation, and it is also the heliocentric angle of the flare in the geocentric point of view.

enters and escapes from the photosphere at the same position. This assumption is generally valid because the height of the X-ray source is believed to be much larger than the mean free path of the photon in the photosphere, which is only about $10^7$ cm.

Through the second factor in equation (3.31), h affects the brightness distribution of the albedo patch. Thus, by measuring the albedo brightness distribtion, we might be able to deduce h. This was first pointed out by Brown et al. (1975); however, in their calculation it was assumed that the reflection probability was constant. As will be shown, because it depends on the directions of the incident and outgoing photons and also on the polarization, this fact should be taken into account for a better deduction of h.

Before we calculate $R(\epsilon_1 \sim \epsilon_2, \theta_o, \theta, \phi)$ by a Monte Carlo simulation, let us analyze the probability for a photon with energy $\epsilon_o$ incident upon the photosphere along the direction $(\theta_o, \theta^o)$ to be reflected per unit solid angle around the direction $(\theta, \phi)$. This probability is closely related to $R(\epsilon_1 \sim \epsilon_2, \theta_o, \theta, \phi)$. The value of the reflection probability, P, is determined by the combined effects of the angular dependence of the Compton scattering cross section and the probability for escape determined by the amount of material traversed before and after the scattering process. To investigate these effects, we decompose P into $P^i$, where the superscript i represents the number of collisions made before the escape. Then the dominant term, $P^1$, can be expressed analytically (Appendix C):

$$P(\epsilon_o, \theta_o, \theta, \phi) = \sum_{i=1}^{\infty} P^i(\epsilon_o, \theta_o, \theta, \phi)$$

$$= \frac{1}{\sigma_c(\epsilon_o) + \sigma_a(\epsilon_o)} \cdot \frac{d\sigma_c}{d\Omega}(\epsilon_o, \theta_s(\theta_o, \theta, \phi)) \frac{1}{1 + \frac{(-\cos\theta_o)}{\cos\theta}} + \sum_{i=2}^{\infty} P^i, \qquad (3.33)$$

where

$$\cos\theta_s = \cos\theta_o \cos\theta + \sin\theta_o \sin\theta \cos\phi. \tag{3.34}$$

As can be seen, the angular dependence of $P^1$ consists of two factors, which are plotted in Figure 3.17 as functions of $\theta_o$ for three values of $\theta$. The factor, $1/(1 - \cos\theta_o/\cos\theta)$, which is due to the probability for escape, is shown by solid lines. Physical interpretations of this figure are as follows. For example, for a given observation angle $\theta$, P increases as $\theta_o$ decreases from vertical incidence ($\theta_o = 180°$), mainly because less material is traversed by the escaping photons when $\theta_o$ is small than when $\theta_o$ is large. For a given $\theta_o$ (>90°), P decreases as $\theta$ increases from $\theta = 0°$ (vertical escape) because also in this case increasingly larger amounts of material are traversed by the escaping photons. Another angle-dependent factor, the second factor, in the expression for $P^1$ in the above equation is due to the Compton cross section. Using the Thompson cross section for an unpolarized beam of photons, we plot it in this figure as dashed lines. Mainly because of this factor, P depends on $\phi$. And through this factor, the state of polarization of the primary source strongly affects the albedo brightness distribution.

Because the X-ray emission of the anisotropic primary source considered in this thesis is partially polarized along the normal plane, such X-ray emission can be regarded to consist of an unpolarized emission and a completely plane-polarized emission. Thus, it would be convenient to have calculations of the differential reflectivity of a completely unpolarized beam of photons and also of a completely plane-polarized beam of photons, for various beam directions. From such results the differential reflectivity of a beam of photons with an arbitrary degree of polarization can be obtained.

Because the highest two energy bins of the Hard X-ray Imaging Spectrometer, which are suitable for the albedo measurements, are from 16 to 22 keV and from 22

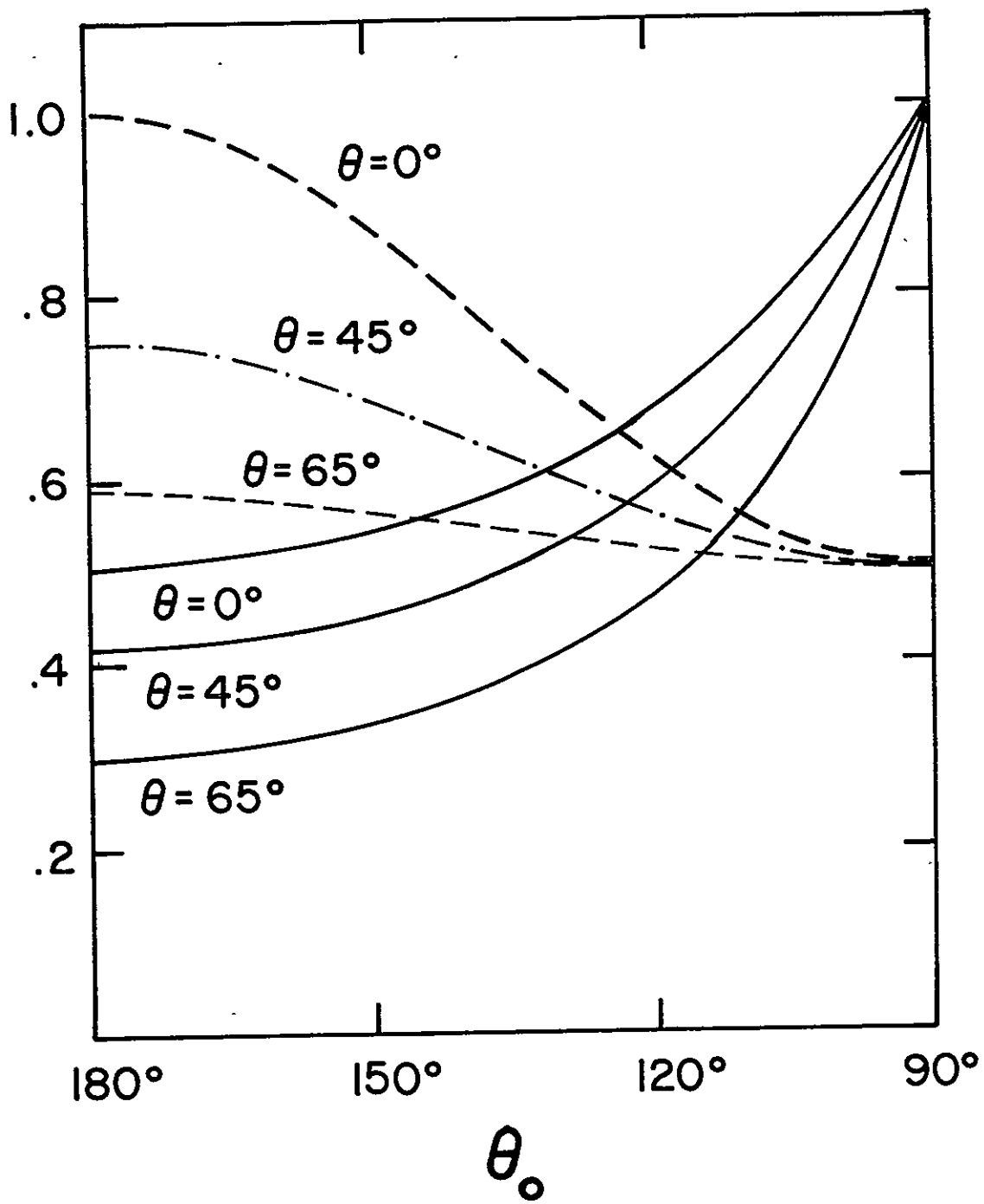


Figure 3.17. The plotting of $f_1(\theta, \theta_o, \phi) = 1/(1 - \cos\theta_o/\cos\theta)$ and $f_2(\theta, \theta_o, \phi) = \left(\frac{4\pi}{\sigma_T}\right)\frac{d\sigma_T}{d\Omega}(\theta_s(\theta, \theta_o, \phi))$ for $\phi = \frac{\pi}{2}$. The solid lines represent $f_1$ and the dashed lines represent $f_2$. The product of these two functions $f_1 f_2$ is proportional to the scattering probability due to a single scattering.

keV to 30 keV, we calculate the differential reflectivity in these energy intervals, for various beam directions ($\theta_o = 180°$, $170°$, $160°$, . . ., $100°$) and for the two states of polarization. We calculate for three power-law spectra of the incident beams ($\epsilon^{-3}$, $\epsilon^{-4}$, and $\epsilon^{-5}$), and we fit the results for the spectrum $\epsilon^{-3}$ with smooth curves in Figures 3.18 through 3.21. (The results for the other spectra show similar properties as in these figures.)

The major characteristics of the differential reflectivity of an unpolarized beam as a function of the beam direction are easily noticed from Figures 3.18 and 3.19, and are summarized as follows: (1) for $\theta \simeq 0°$ (flares at the disk center), the differential reflectivity decreases slowly as the beam direction $\theta_o$ decreases from $180°$ to $90°$. (2) For large values of $\theta$ (flares away from the disk center), the differential reflectivity increases as the beam direction $\theta_o$ decreases. The net effects of these characteristics are as follows: For flares near the disk center, the scale size of the albedo patch will be smaller than that obtained by assuming that the reflectivity is independent of the incident direction; on the other hand, for flares away from the disk center ($\theta \gtrsim 35°$), the scale size of the albedo patch will be larger.

The differential reflectivity of a completely polarized beam of photons (the Stokes parameters with respect to the normal plane are $P_1 = -1$, $P_2 = 0$) are shown in Figures 3.20 and 3.21. From the comparison of these figures with Figures 3.18 and 3.19, the differences are self-evident. These differences are due to the fact that, for the Stokes parameters $P_1 = -1$, $P_2 = 0$, the scattering cross section is largest at $\phi = 90°$ or $270°$ and is smallest at $\phi = 0°$ or $180°$, at a given scattering angle $\theta_s$ (see equation 3.11). The reason why the reflection probability at $\phi = 180°$ is generally much larger than at $\phi = 0°$ is as follows. From the geometry of the problem, for given

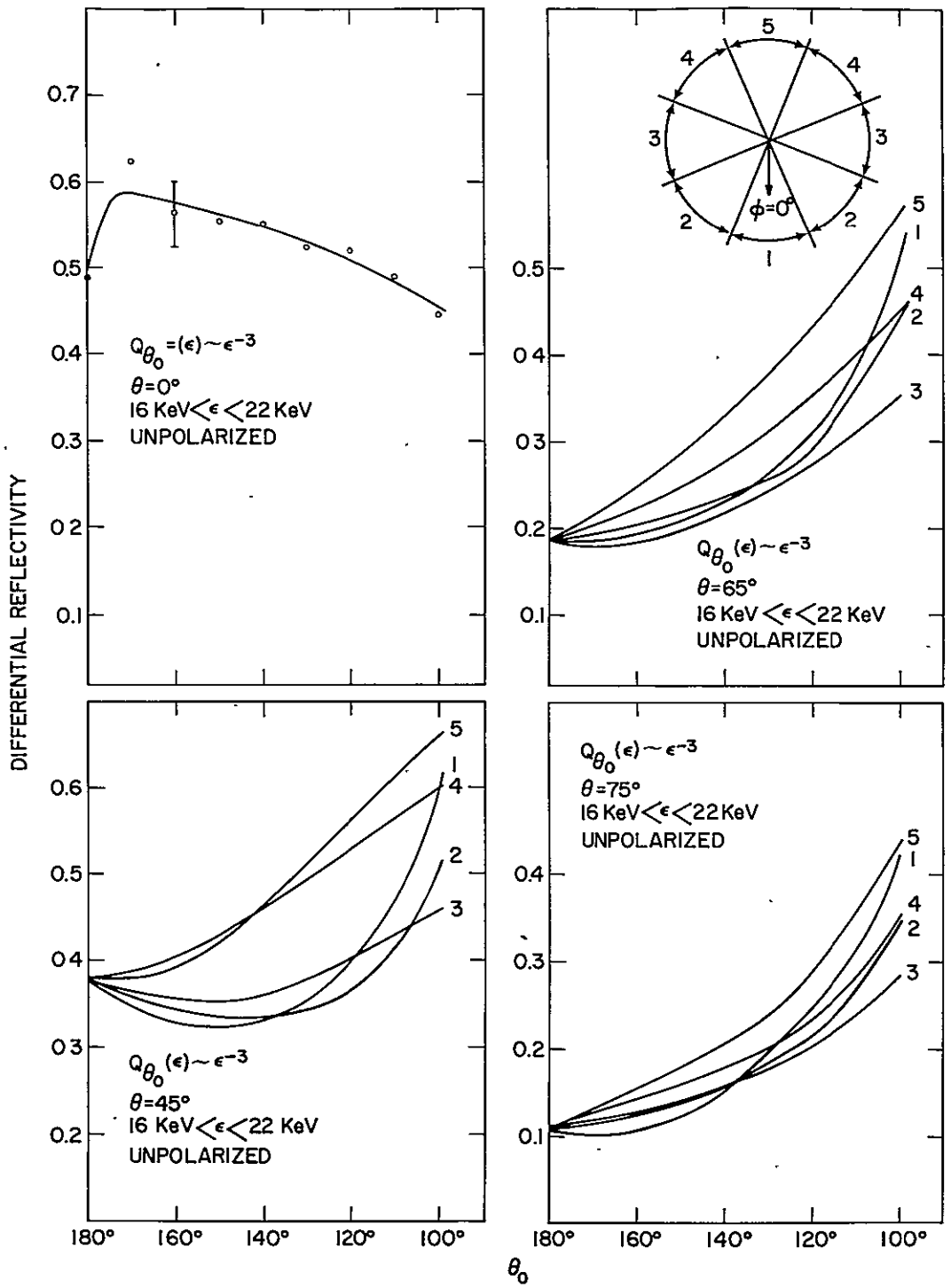


Figure 3.18. The differential reflectivity of an unpolarized beam as a function of the beam direction. It is measured in the interval from 16 to 22 keV, and the spectrum of the incident beam is $\epsilon^{-3}$. The error bar in the upper-left panel represents a typical one-sigma error, and open circles represent the results of the Monte Carlo simulation.

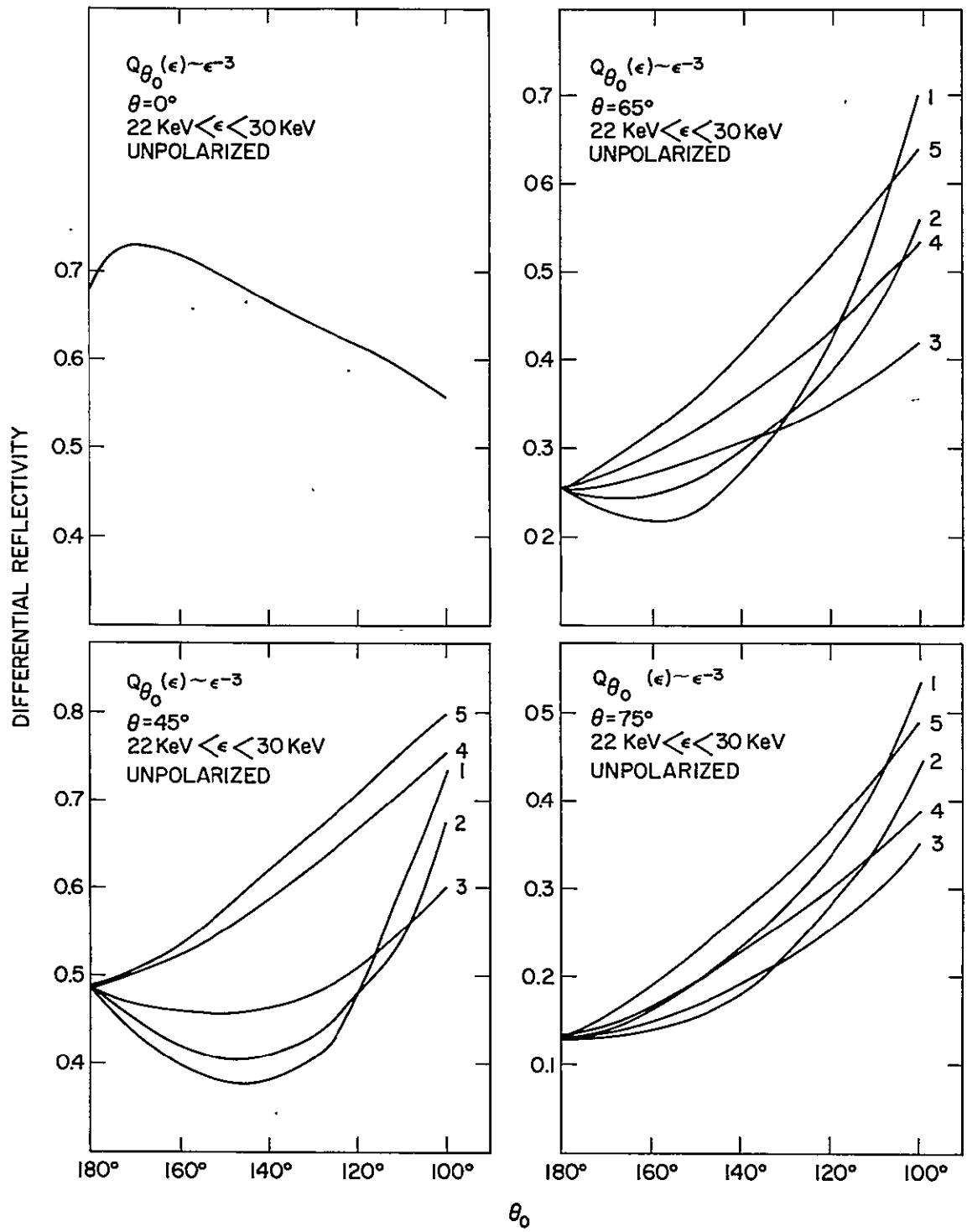


Figure 3.19. Same as the above Figure, except the energy interval is from 22 keV to 30 keV.

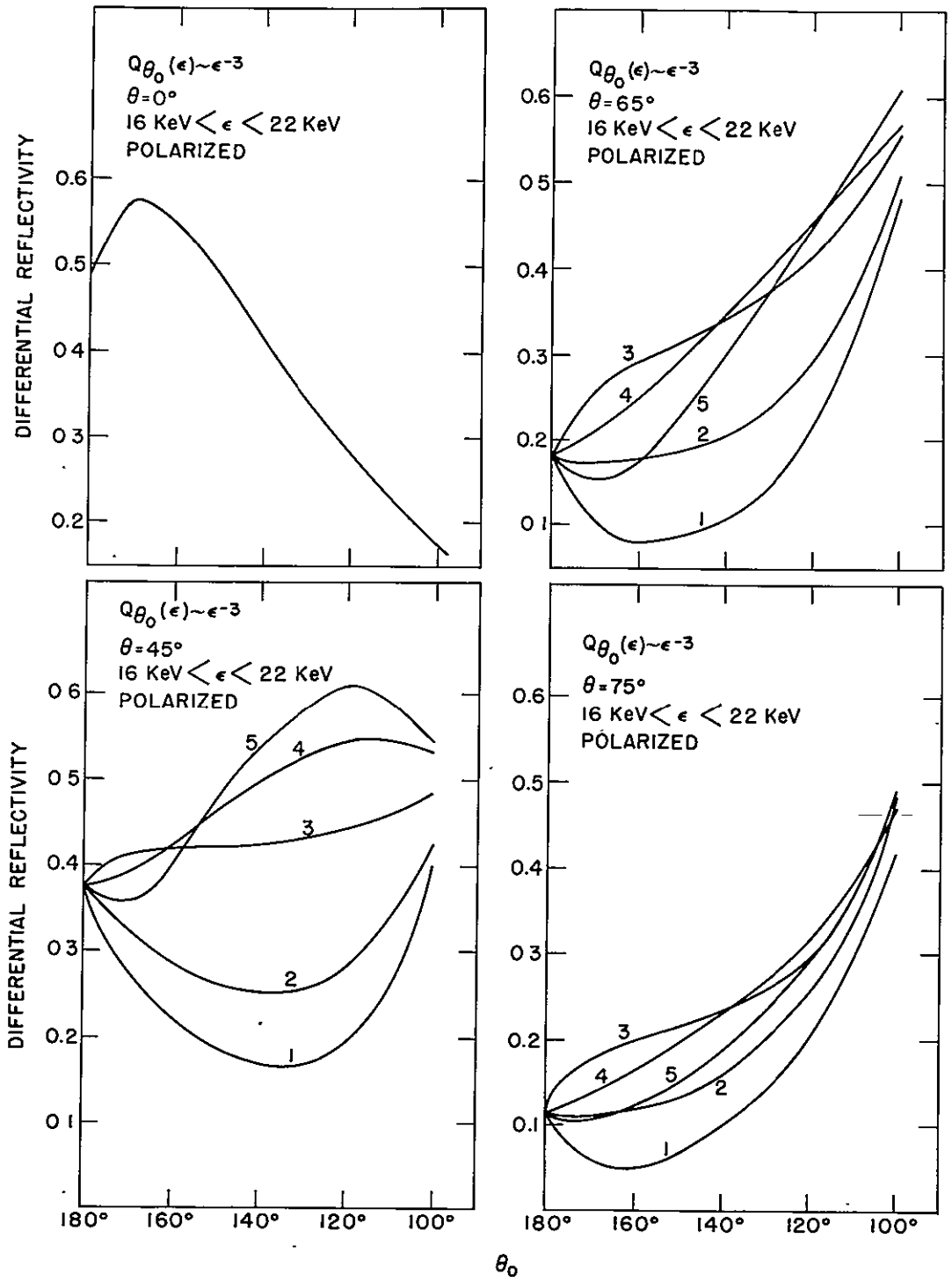


Figure 3.20. The differential reflectivity of a completely polarized beam as a function of the beam direction. The energy interval is from 16 to 22 keV, and the incident photon spectrum is $\epsilon^{-3}$.

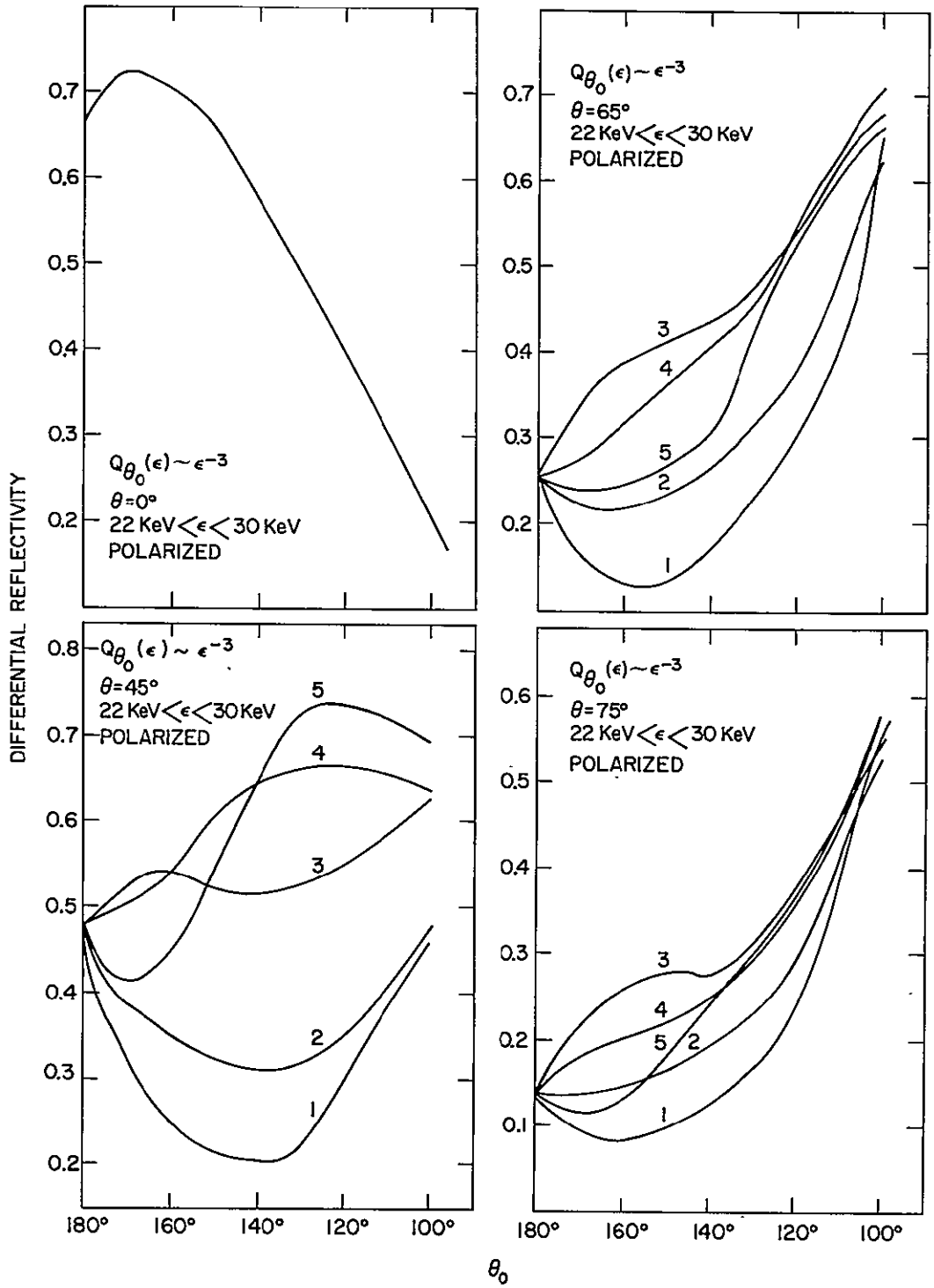


Figure 3.21. Same as the above Figure, except that the energy interval is from 22 to 30 keV.

$\theta$ and $\theta_o$, $\sin\theta_s$ is smaller when $\phi = 180°$ then when $\phi = 0°$; thus the effect of polarization on the scattering cross section is small when $\phi = 180°$.

The isobrightness contours of the albedo patch are drawn for several cases in Figure 3.22 with the scale in units of the height h. Starting from the center, the albedo brightness drops by a factor 1/2 from one contour to the next. For the anisotropic source used in this figure, we assume that the photon spectrum is $\epsilon^{-3}$ regardless of the incident direction, and that the degree of polarization is the same as the degree of polarization of 20 keV photons shown in Figure 3.8. For the anisotropic source for this figure, we also assume that the photon flux is constant in the downward hemisphere. As can be seen, the albedo patch due to the polarized primary source near disk center is slightly smaller than that due to the unpolarized primary source with the same condition. In addition to the effect of polarization, the anisotropic distribution of the primary X-rays affects the albedo brightness distribution. However, for $\epsilon \lesssim 20$ keV the photon flux incident upon the photosphere is more or less constant independent of the incident angle (see Figures 3.9 and 3.11). From Figure 3.22 d, we notice that the albedo brightness of the polarized primary source away from the disk center is quite asymetric about the upward-downward reflection. The surface brightness drops faster in the downward directions ($0° < \phi < 90°$ and $270° < \phi < 360°$) than in the upward directions ($90° < \phi < 270°$). For example, for $\phi = 0°$ the surface brightness at 3h is 1/32 of that at the centroid of the patch, whereas for $\phi = 180°$ it is about 1/20. Thus, from the shape of the albedo brightness contours, we may be able to learn about the state of polarization of the primary X-ray emission. (See Chapter IV.) Together with the information on the anisotropy of the X-ray emission obtained from the comparison of the number of direct photons and the number of the reflected photons, we may be able to have better

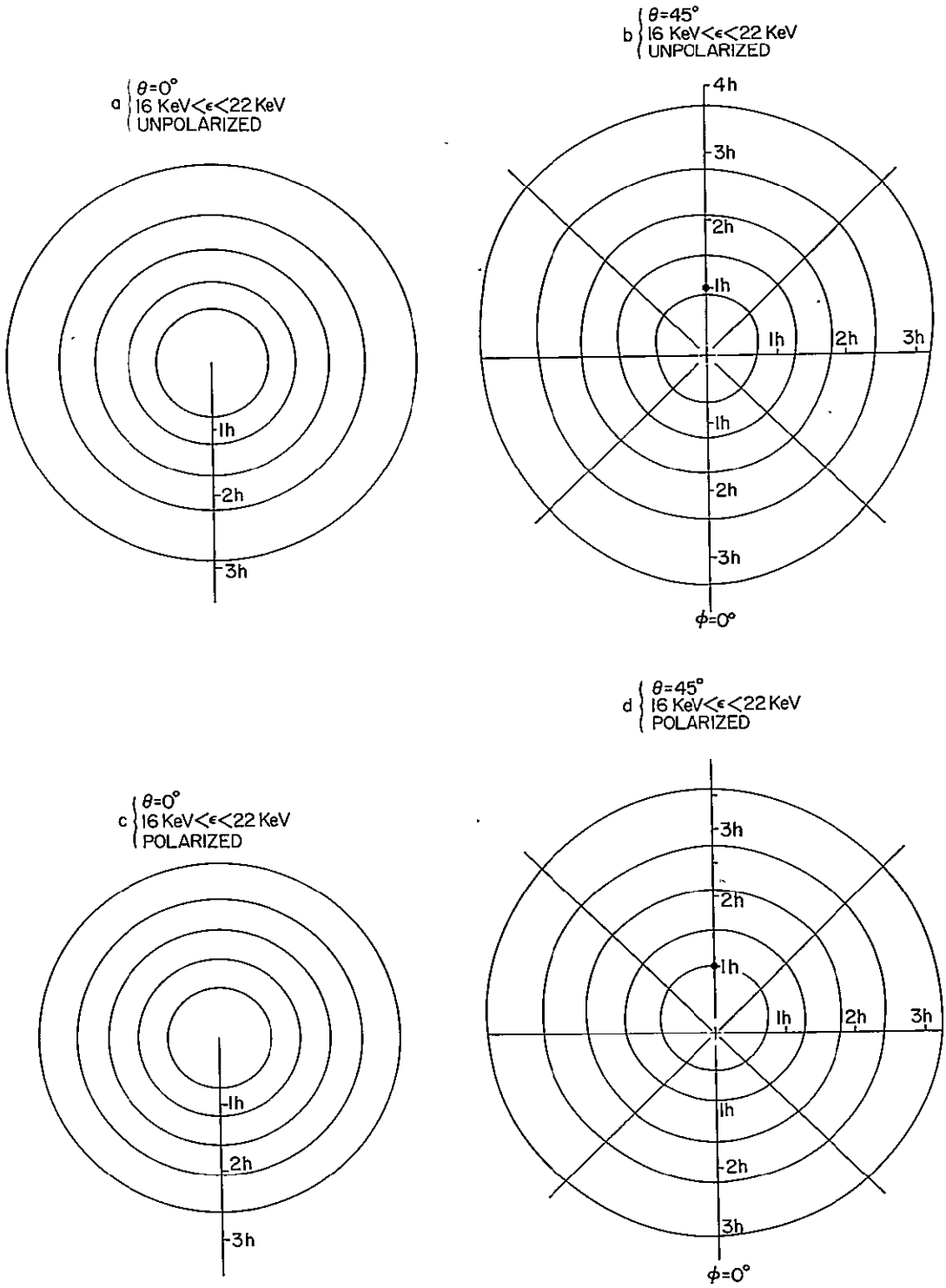


Figure 3.22. Isobrightness contours of the albedo patch for various cases. Starting from the center brightness drops by a factor 1/2 from one contour to the next.

understanding of the anisotropy of the accelerated electrons producing hard X-rays in the flare region.

Black dots (•) in the figure represent the projection on the albedo patch of the primary X-ray source along the line of sight, and the cross marks (+) in the figure represent the centroid of the albedo patch. The distance between these two is h tan $\theta$. Thus, the measurement of this distance can also give information on the height of the primary source.

## F. Discussion and Summary

To check the correctness of our calculations, we compare our results with calculations of other researchers, wherever similar calculations are available. Agreements are generally good, and the differences can be easily attributed to the differences in the assumptions. We also compare our Monte Carlo results with the approximate analytical results, whenever they can be easily obtained with simple approximations. The results obtained by both methods are in good agreements, and the differences can be accounted for by the approximations made for the analytical calculations.

The researchers who have calculated the polarization of solar hard X-rays until now have not reported that there exists a misprint in one of the formulas for the polarization cross sections by Gluckstern and Hull (1953). (Gluckstern 1977, private communication; see Section II. B.) The error in the calculations of polarization caused by overlooking this misprint is of the order of 10%. Since we use the corrected formula, our results are more accurate in this sense.

Though a quite significant fraction of photons incident upon the photosphere with energy $\gtrsim$15 keV are backscattered, for isotropic sources, the effect on the photon spectrum due to the backscatter is not easily observable. For anisotropic sources

which emit hard X-rays predominantly toward the photosphere, the effects of the backscatter is significant. Because of the backscatter, the large limb brightening effect, which would be expected otherwise for such anisotropic sources, is cancelled. For such anisotropic sources, the observed photon spectrum in the 15 to 50 keV range steepens as the flare location moves toward the limb. Such a limb steepening and the lack of limb brightening effect are compatible with the data of Datlowe et al. (1974). For such anisotropic models, the spectrum above 100 keV is steeper than the spectrum at lower energies, particularly for flares near the disk center. Langer and Petrosian (1977) reported similar results. However, they assumed that accelerated electrons are strictly beamed. We used electrons with power-law energy spectra, whereas they used electrons with power-law flux spectra. Thus, the steepening of the resultant photon spectra above 100 keV is larger in their results than in ours.

Because of the different assumptions, the results of Langer and Petrosian (1977) cannot be directly compared with ours. However, the photon spectra they reported seem to be too flat. They parameterized the electron flux spectra with $\delta$ as follows: $\frac{dJ(E)}{dE} \sim E^{-\delta-1}$ (Petrosian 1973, Langer and Petrosian 1977). As the relationship between the electron spectra and the photon spectra measured in the 20 to 100 keV range for flares near the disk center, Langer and Petrosian (1977) give the following: $q(\epsilon) \sim \epsilon^{-3.20}$ for $\delta = 3$; $q(\epsilon) \sim \epsilon^{-4.46}$ for $\delta = 4$. In the nonrelativistic electron energy region, according to their notation, $\delta = 3$ corresponds to the electron spectrum $\frac{dN(E)}{dE} \sim E^{-4.5}$; $\delta = 4$, $\frac{dN(E)}{dE} \sim E^{-5.5}$. On the other hand, according to our result, the relationship between the electron spectra and the photon spectra measured in the 20 to 100 keV range for disk flares is as follows: $q(\epsilon) \sim \epsilon^{-3.11}$ for $\frac{dN(E)}{dE} \sim E^{-2.5}$; $q(\epsilon) \sim \epsilon^{-4.32}$ for $\frac{dN(E)}{dE} \sim E^{-3.5}$. Therefore, it seems that they parameterized the electron flux spectra erroneously. If

corresponded to the electron flux spectrum $\frac{dJ}{dE}(E) \sim E^{-(\delta-1)}$ instead of $\frac{dJ(E)}{dE} \sim E^{-\delta-1}$, their result would be compatible with ours.

Though the backscattered photons are dominant for the anisotropic sources considered in this chapter, the degree of polarization of the total photon flux (primary flux plus reflected flux) at 15 keV or 30 keV follows the pattern of the degree of polarization of the primary flux alone. It is zero at the disk center and monotonically increases to the large maximum at the limb. On the other hand, for isotropic, unpolarized primary sources, the degree of polarization of the total flux is less than 4% even at the maximum. Thus, the measurements of polarization can be a powerful probe for the anisotropy of the accelerated electrons. The measurements by Tindo and his coworkers, though they are somewhat tentative in nature, show quite large degrees of polarization, which cannot be attributed to the backscatter of the isotropic, unpolarized primary source. Nakada et al. (1974) also reported the measurements of finite polarization. These measurements indicate that the X-rays with energy $\gtrsim$15 keV are very likely to be produced by anisotropic (nonthermal) electrons. This matter is discussed in more detail in the next chapter.

Provided that the surface brightness of the albedo patch is measured in detail, the ratio between primary and reflected photon fluxes, the size of the albedo patch, and the displacement of the primary X-ray source from the centroid of the patch, can give information on the anisotropy and height of X-ray source. In favorable cases, detailed albedo measurements can also give information on the polarization of the primary X-rays incident upon the photosphere. An extended source can be regarded as a superposition of many point sources; however, for extended sources, it will be more difficult to extract such information. A more detailed discussion is given in the next chapter.

# CHAPTER IV

# DATA-ORIENTED DISCUSSIONS ON THE HEIGHT AND THE ANISOTROPY OF THE SOLAR HARD X-RAY SOURCE AND ON THE POLARIZATION OF SOLAR HARD X-RAYS

## A. Introduction

In Chapter III we have investigated the theoretical relationship between the brightness distribution function of the albedo patch and the height and the anisotropy of the X-ray source, and the relationship between the degree of polarization of hard X-rays and the anisotropy of the X-ray source. Preliminary data on the polarization already exist (Tindo et al. 1970, 1972a, 1972b, 1973, Nakada, Newpert, and Thomas 1974), and the data on the brightness distribution of the X-ray albedo patch will be available from the Hard X-ray Imaging Spectrometer, which will be included in the payload of SMM. In this chapter, by performing data-oriented discussions, we investigate the kind of data expected from the Hard X-Ray Imaging Spectrometer and the kind of information that can be deduced from them. We also investigate the implications of polarization data.

The Hard X-Ray Imaging Spectrometer is being developed in the Space Research Laboratory, Utrecht, and its characteristics are described by de Jager (1976). Here we give a few of its characteristics relevant to our discussion. It consists of 1024 mini proportional counters (mpc) arranged in a two-dimensional pattern of 32 rows and 32 columns. Each mpc is a small detector with spatial resolution of 8 X 8 arcsec square (FWHM) and an effective detector area of 0.1 $cm^2$. The axes of the mpc's are arranged to make angles of 8 arcsec between the neighboring pairs in two mutually

perpendicular directions; thereby the instrument can produce two-dimensional pictures with a total field of view 4.3 X 4.3 arcmin square, with each mpc serving as an image element. The six energy bands of the instrument are 3.5 ~ 5.5 ~ 8.5 ~ 12 ~ 16 ~ 22 ~ 30 keV. The background count rate is less than 0.01 count/sec/mpc, and the efficiency at the 16 to 22 keV band is about 0.5 (van Beek 1977, private communication).

With good count statistics, the measurements in the highest two energy bands are most likely to give valuable information on the height of the hard X-ray source. The reflectivity is very high in the 22 ~ 30 keV energy band, and the disadvantage of the smaller reflectivity in the 16 ~ 22 keV energy band is well compensated by the higher flux of the primary photons in this energy band. Therefore, the albedo measurements in these two energy bands can give good count statistics, and consequently can lead to the knowledge on the height of the X-ray source. In the 12 ~ 16 keV energy band, the radiation from hot thermal plasma may dominate. Therefore, in this chapter we investigate the albedo brightness distribution measured in the energy bands from 16 to 22 keV and from 22 to 30 keV.

The polarimeters used by Tindo and his coworkers and by Nakada and his coworkers basically utilize the fact that the Compton cross section of the polarized X-ray beam is dependent on the azimuthal angle of the scattering (equation 3.11). The polarimeter consists of six counters separated by 60° from each other around the axis of the Beryllium scatterer. Thus the comparison of the counting rates of the six counters can in principle give information on the degree and the direction of the polarization.

In Section B, by calculating the counts registered in the mpc's of the Hard X-Ray Imaging Spectrometer, due to idealized sources, we discuss the range of the height

of the X-ray source that can be deduced by using this instrument. In Section C we discuss in detail how to measure the anisotropy of the primary X-ray source. In Section D we discuss and interpret on the data on the polarization.

B. Determination of the Height

In order for us to deduce, h, the height of the X-ray source from the photon counts registered in the mini proportional counters of the Hard X-ray Imaging Spectrometer, first of all, the number of mpc's with significant counts should be large enough. For a given X-ray source, the number of mpc's with significant counts depends on h. As h becomes smaller, the photon counts become concentrated in a smaller number of mpc's, while as h becomes larger, the surface brightness of the albedo patch becomes lower, and consequently the count registered in each mpc becomes smaller. These two effects give the lower and upper limits on the range of height that can be deduced by using this instrument.

The limits also come from other effects. If h is so large that the total field of view of the instrument can cover only a small fraction of the albedo patch, then the uncertainty of the deduced h becomes too large. If h is so small that the albedo photon count in one mpc comprises too large a fraction of the total albedo photon count, the uncertainty of the deduced h also becomes too large.

In this section, by calculating the counts registered in mpc's of the Hard X-ray Imaging Spectrometer for various values of h, we are going to discuss the range of h that can be deduced by using this instrument. For simplicity we make the following idealizations: (1) The instrumental response function of the mpc is constant for a point source within the 8 x 8 arcsec square centered around the axis of the mpc,

regardless of the position within this square, and is zero for a point source outside this square. This idealization gives a strict one-to-one correspondence between the mpc and the rectangular area on the photosphere. (2) The primary X-ray source is a point source. (3) The instrument is positioned such that the centroid of the albedo patch is at the center of the field of view of one of its mpc's and that one of the axes of the array is made parallel to the line joining the disk center and the primary source. (4) The primary source is isotropic, and its spectrum is $\epsilon^{-3}$, and the flux in the 16 to 22 keV interval is $3.2 \times 10^{29}$ photons/(sr-sec) (except for Figure 4.4).

1. Sources at the Disk Center

Because the differential reflectivity in the energy range from 16 to 22 keV is 0.47 for the spectrum $\epsilon^{-3}$, when $\theta = 0°$, the total intensity in this energy range measured at the earth due to the above-mentioned source is ~2000 photons/(sec-cm$^2$). This is a quite strong X-ray source, when compared with ~3000 photons/(sec-cm$^2$) in this energy range calculated from an extrapolation of the measurement of the August 4, 1972 flare by van Beek et al. (1973). Several such strong X-ray events may occur during the next solar maximum.

The count of photons in the 16 to 22 keV interval, registered in 60 seconds in each mpc of the Hard X-ray Imaging Spectrometer, can be calculated by using the differential reflectivity for $\theta = 0°$ shown in Figure 3.18. (Here notice that 60 seconds is the time scale of the durations of the spiky hard X-ray bursts of the August 4, 1972 flare.) Figure 4.1 shows the result for h = d, where d is the perpendicular distance at 1 AU corresponding to the angular resolution of the image element. Similarly Figure 4.2 shows the result for h = 4d. From these figures we see that in both cases

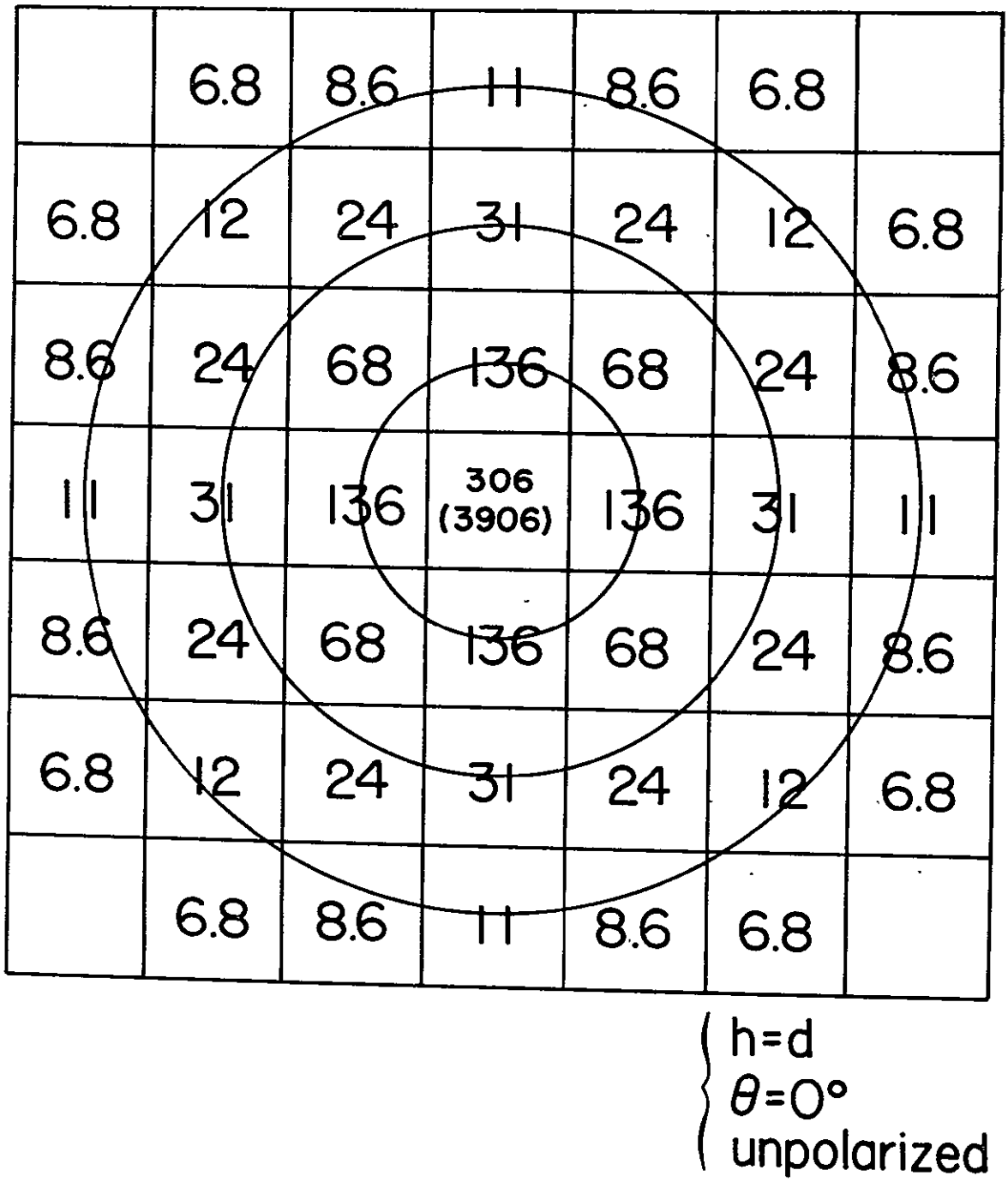


Figure 4.1. Calculated albedo photon counts registered in the mpc's of the Hard X-ray Imaging Spectrometer, for an isotropic source at $\theta = 0°$ and h = d. Idealizations made for this calculation are described in the text. The large number in the parenthesis is due to the primary source.

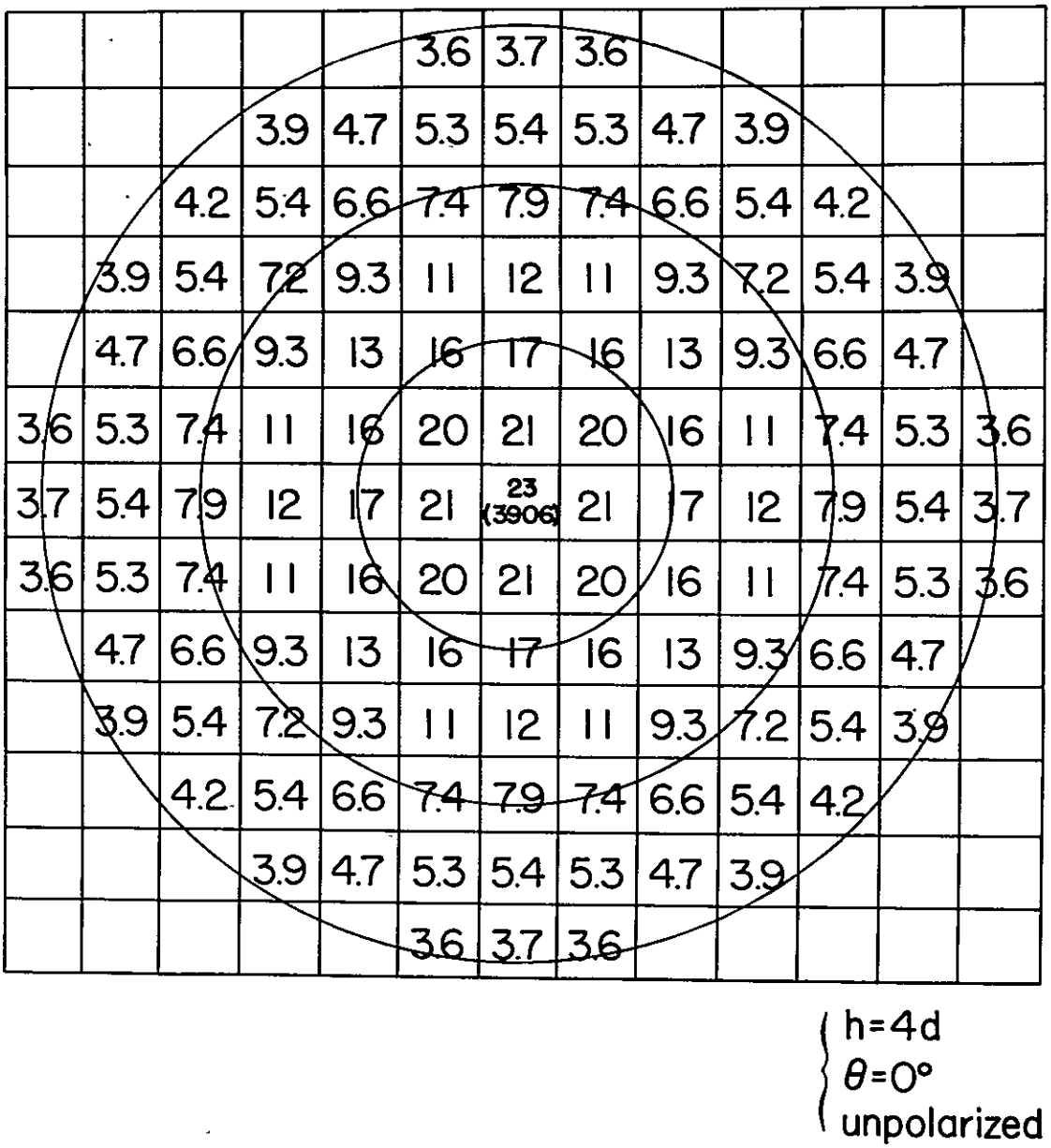


Figure 4.2. Calculated albedo photon counts, for an isotropic source at $\theta = 0°$ and $h = 4d$.

the number of mpc's which register significant counts is large enough to deduce the height of the source by use of such counts. Notice here the count due to the primary source is conspicuous.

If h = 0.5 d, the counts registered in neighboring four (2 X 2) mpc's in Figure 4.1 will be registered in one mpc. By grouping neighboring four mpc's and adding the counts in these four mpc's, we find the number of image elements with significant counts ($\gtrsim 5$) is about 30 for the case h = 0.5 d. If he becomes smaller than 0.5 d, not only the number of mpc's with significant counts decreases but also the albedo photon count registered in the mpc covering the centroid of the albedo patch becomes larger than about one third of the total albedo photon counts. Therefore, about 0.5 d is the lower limit of h that can be deduced by using this instrument.

If h is 16 d, then the counts registered in each mpc will be about 1/16 of those shown in Figure 4.2, which is of the order of 1. However, in such a case, by summing up the counts in neighboring 16(4 X 4) mpc's, we can get as good count statistics as shown in Figure 4.2, in the expense of the spatial resolution. By summing up the counts in neighboring 16(4 X 4) mpc's, we make the Spectrometer have 64(8 X 8) effective image elements. When h = 16 d, the area of the albedo patch covered by the Spectrometer is 2h X 2h, which is a relatively small portion of the patch and gives about 1/3 of the albedo photons if the center of the patch falls near the center of the field view of the Spectrometer. Therefore, about 16 d is the upper limit of h that can be deduced by using the Hard X-ray Imaging Spectrometer.

Hence in the range

$$0.5d \lesssim h \lesssim 16d, \tag{4.1}$$

the height of the idealized point source with a quite strong intensity can be measured. For the Hard X-Ray Imaging Spectrometer for SMM, $d = 5.8 \times 10^8$ cm; therefore, the range of h deducible by using it is

$$3 \times 10^8 \text{ cm} \lesssim h \lesssim 10^{10} \text{ cm}, \tag{4.2}$$

for sources with fluxes stronger than $3.2 \times 10^{29}$ photons/(sr-sec) in the 16 to 22 keV range. This range covers most of the heights predicted by various models (Brown and McClymont 1975). For the sources with fluxes weaker than $3.2 \times 10^{29}$ photons/(sr-sec) in the 16 to 22 keV interval, the range of h deducible by using the instrument decreases accordingly. For example, for the source weaker than the above-mentioned source by a factor of four, this range is about from $10^9$ cm to $5 \times 10^9$ cm. The range for stronger sources, however, does not increase significantly from that given by equation 4.2.

2. Sources Away from the Disk Center

Because of the decrease of the differential reflectivity $R(\epsilon, \theta)$ with $\theta$, the surface brightness of the albedo patch drops as $\theta$ increases. However, because the area of the albedo patch covered by each image element is $\sec \theta \, d^2$, in terms of count statistics, the source away from the disk center is not disadvantageous. Figure 4.3 shows the counts in several image elements for $\theta = 45°$ and $h = 4d$, calculated similarly to Figures 4.1 and 4.2. Here we use the angular dependence of the differential reflectivity shown in Figure 3.18.

Many characteristics of the albedo patch of the off-center source, which are discussed in Section III. E, become evident by comparison of Figure 4.3 with Figure 4.2. However, one of the important characteristics of the albedo patch of the off-center

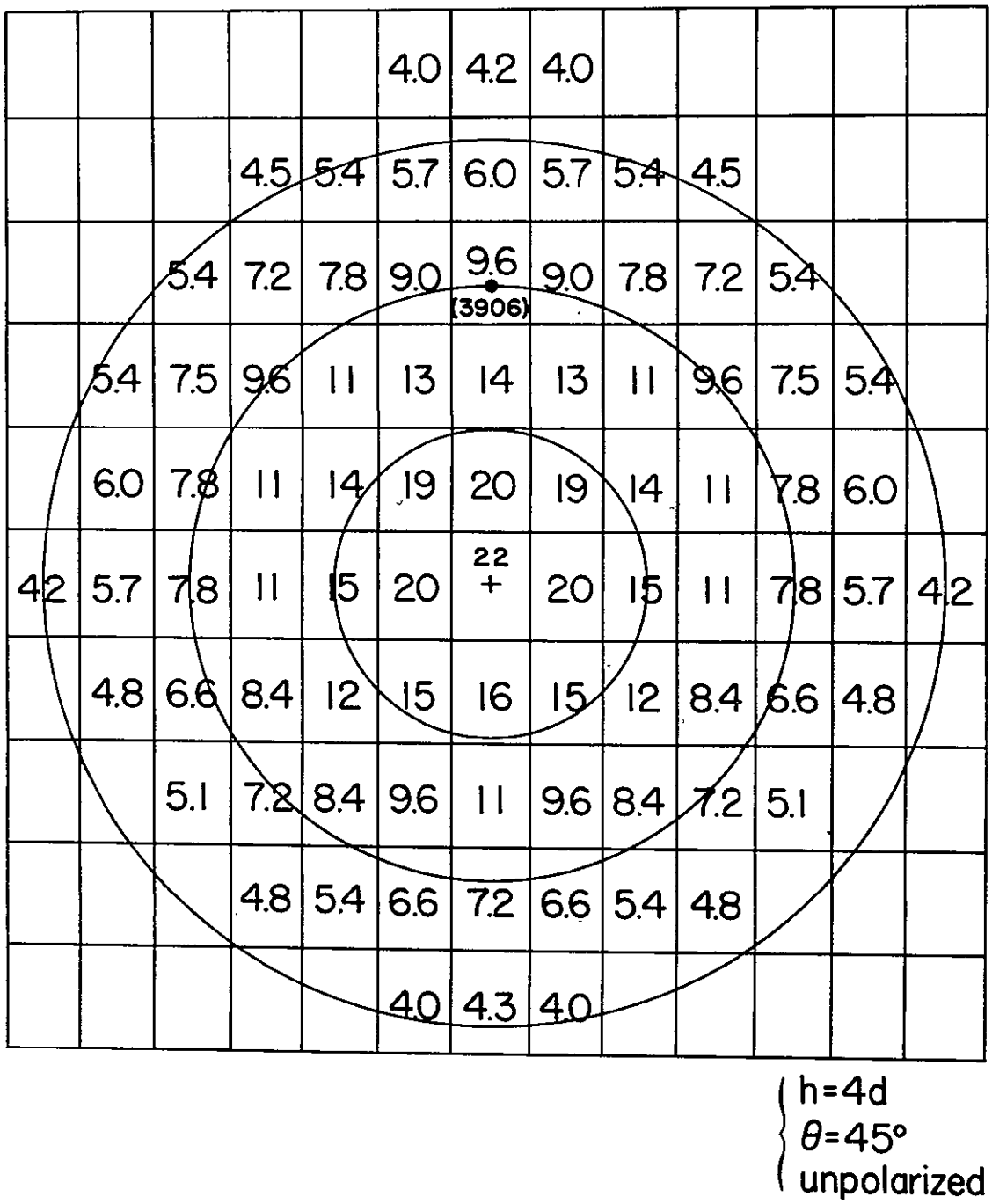


Figure 4.3. Calculated albedo photon counts, for an isotropic source at $\theta = 45°$ and h = 4d. The black dot represents the projected position of the primary source.

source is the displacement of the projection of the primary source with respect to the centroid of the albedo patch. This displacement can provide us another method in determining the height of the source.

In order for this method to be useful, the displacement, $h \tan\theta$, should be much larger than the distance on the photosphere covered by an image element along the direction of this displacement, which is $d \sec\theta$. The displacement, however, should not be larger than about one half of the field of view of the Imaging Spectrometer. These two conditions yield

$$d/\sin\theta \ll h \lesssim 16d/\sin\theta. \tag{4.3}$$

Comparing the above equation with equation (4.1), we find that the above method can increase the upper limit of h deducible by using the Hard X-ray Imaging Spectrometer. Therefore, this method can be well utilized for large h and small $\theta$. The limitation comes, however, when h becomes too large and consequently the albedo patch becomes too faint to determine the centroid of the patch.

3. Extended Sources

So far the source has been assumed to be a point source, and this assumption is good as long as the size of the source is much less than its height. If the size becomes comparable to h, the deduction of the height becomes complicated. If the source is extended in two or three dimensions and its linear size is larger than its height, the height determination is next to the impossible. However, as we have seen in Figures 4.1 through 4.3, the photon count due to the primary source is conspicuous. Therefore, for sources larger than the spatial resolution of the instrument, the shape of the primary source can be known. Hence, for the extended source with

the height larger than its size or the source of filament shape, the determination of the height is not so complicated.

### C. The Anisotropy of Solar Hard X-rays

So far we have treated isotropic primary sources only. For an anisotropic source, the angular distribution of solar hard X-rays is determined by the angular distribution of the momentum vectors of the accelerated electrons producing them. The angular distribution of primary hard X-rays, in turn, influences the brightness distribution of the albedo patch. In addition, the degree of polarization of primary hard X-rays also influences the brightness distribution of the albedo patch through the azimuthal dependence of the Compton cross section of the polarized photon beam (equation 3.11). In this section we discuss how to deduce the angular distribution of primary hard X-rays.

As we have seen in Section III. E, the fact that the differential reflectivity of a photon beam depends on the degree of polarization makes the deduction of the degree of anisotropy (and the angular distribution) of the primary X-ray source a little bit more complicated. However, the degree of anisotropy of the primary X-rays can be inferred by any of the four ways described below roughly in descending order of feasibility. First, the easiest of all, by finding out the photon count due to reflection, we can find out the number of photons released down to the photosphere. And by comparing this number with the number of photons directly coming from the primary source, we can have an idea on the anisotropy of the solar hard X-rays. Second, if we can deduce h from the displacement of the projection of the primary source with respect to the centroid of the albedo patch, then we can find the angular distribution of the hard X-rays, $Q(\epsilon, \theta_0)$, from the albedo brightness distribution. Third, the

comparison of the albedo brightness distribution measured in the 16 to 22 keV interval with that measured in the 22 to 30 keV interval may tell us the anisotropy of the accelerated electrons. The angular distribution of hard X-rays in the 16 to 22 keV interval is more or less constant in the downward hemisphere even in the anisotropic case (see Figures 3.9 and 3.11). On the other hand, in the 22 to 30 keV interval, it quite strongly depends on the anisotropy. Fourth, from the shape of the albedo patch, we may know about the degree of polarization of the primary hard X-rays incident upon the photosphere (Figure 3.22). This in turn can tell us the anisotropy of the accelerated electrons producing hard X-rays.

Figure 4.4 shows the counts registered in several image elements for a polarized anisotropic source (the same assumption of polarization as for Figure 3.22d) for $\theta = 45^\circ$ and h = 4d, calculated similarly to Figure 4.3. Here notice that the count due to the primary source in Figure 4.4 is smaller than that in Figure 4.3 because we assume that the primary source for Figure 4.4 radiates less in upward directions than downward directions. The albedo count distribution of Figure 4.4 is slightly different than that of Figure 4.3. However, it is found that, to distinguish the effect of polarization on the albedo brightness distribution, the position of the centroid of the patch should be determined within the error of about 0.1 h.

Independent of the albedo measurement, polarization measurements can give information on the anisotropy of primary hard X-rays. However, as we have seen in the previous chapter, the degree of polarization of primary hard X-rays depends not only the degree of anisotropy of the accelerated electrons producing them but also the angle between the line of sight and the direction of anisotropy. Therefore, the

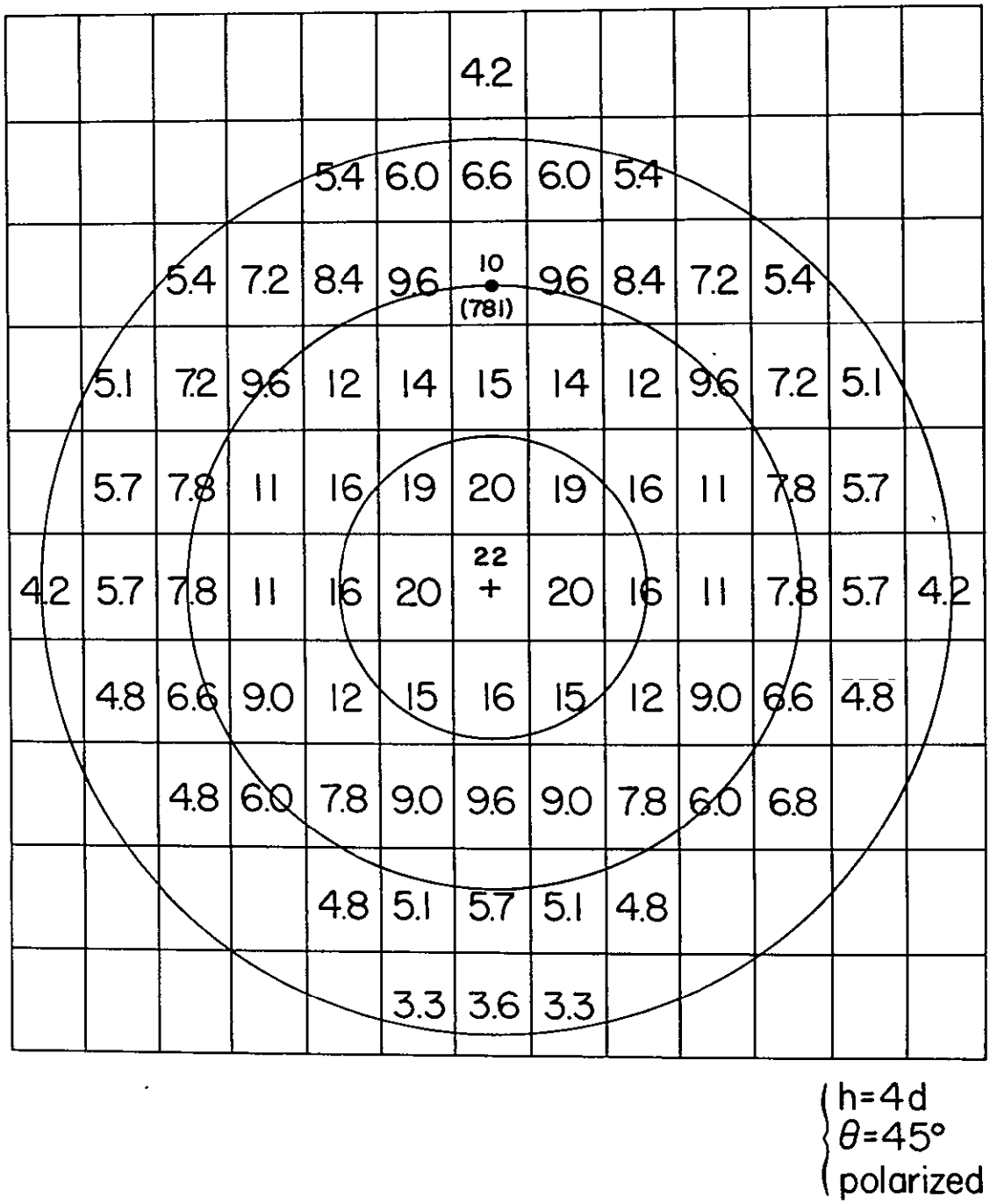


Figure 4.4. Calculated albedo photon counts, for an anisotropic polarized source at $\theta = 45°$ and h = 4d. The black dot represent the projected position of the primary source.

simultaneous measurements of both the albedo brightness and the polarization can complement each other and give less ambiguous information on the anisotropy and also the height of the primary X-ray source.

D. Discussion on Polarization Measurements

The degree of polarization of photons around 15 keV has been measured by Tindo et al. (1970, 1972a, 1972b, 1973) for various flares, and their results are plotted in Figure 4.5 together with the heliocentric angles of the flares. As can be seen, the degree of polarization is quite large except for the flares on August 7 and August 11, 1972.

As we have briefly discussed earlier in this chapter, by comparing the counting rates in the six counters surrounding the Beryllium scatterer of the polarimeter, we can find the degree and the direction of polarization. However, because the energy windows and the efficiencies of the six counters were not exactly the same, and because they were not calibrated in the laboratory before the launch, the counting rates could not be compared directly. Thus, for the flares measured in 1969 and 1970, before comparing the counting rates, Tindo et al. normalized the counting rate of each counter with respect to the counting rate of the counter at the decay phase of the flare, with the assumption that the degree of polarization is zero at the decay phase (Tindo et al. 1970, 1972a, 1972b). This assumption, however, may not be justified. If so, the actual values of the degree of polarization would be different from their estimated values. If the direction of the polarization at the decay phase of the flare was along the same direction as at the earlier phase, the actual degree of polarization would be larger than their estimation, and vice versa.

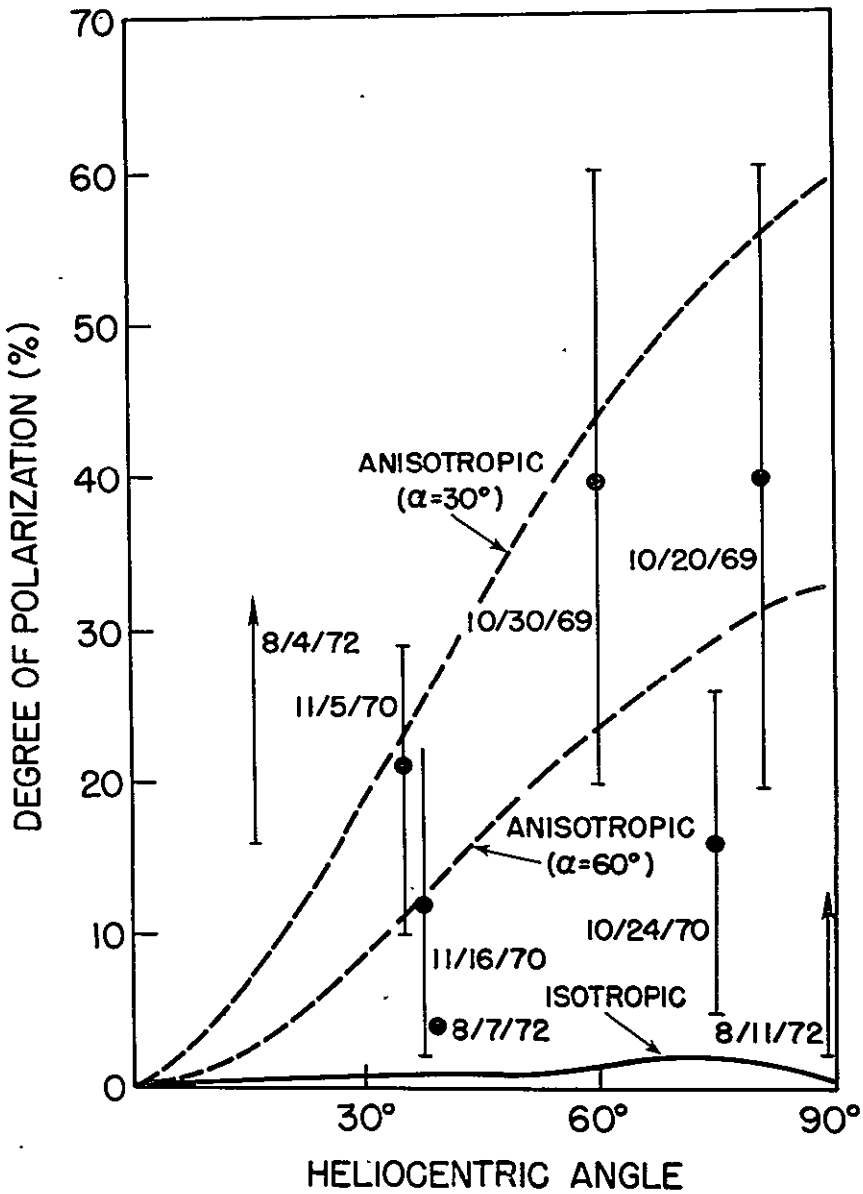


Figure 4.5. The degree of polarization measured by Tindo and his coworkers v.s. heliocentric angle of the flare. Dashed lines represent the calculated degree of polarization at 15 keV for anisotropic sources taken from Figures 3.14 and 3.15. The solid line represents the calculated degree of polarization at 15 keV for an isotropic source taken from Figure 3.13.

Any way, for the flares measured in 1969 and 1970, the degree of polarization increases roughly with the increase of the heliocentric angle of the flare (Figure 4. 5), and the directions of the polarization lie in the normal plane (containing the flare site, the center of the sun and the observer) within 10° uncertainties (Tindo et al. 1972b). Thus these results were interpreted with an anisotropic electron distribution model in which accelerated electrons are spiraling down around the vertical magnetic field lines (Tindo et al. 1972b, Brown 1972).

For the polarization measurements for the August 1972 flares, an improved detector was used. The detector could be rotated by 60° back and forth around the axis of the scatterer, which is along the direction toward the flare, in a short period (Tindo et al. 1973). Thus, the change of the counting rates due to the rotation can be easily recognized, and the efficiency of the counter can be normalized to those of the adjacent counters. Unfortunately, only the two of the six counters functioned properly. Therefore, only the lower limit of the degree of polarization could be inferred, but the heliocentric variation of the degree of polarization does not follow the variation expected from simple anisotropic models of Tindo et al. (1972b) and Brown (1972). If we accept that the direction of the anisotropy may not always be exactly along the vertical direction, we can easily explain the data. Taken as a whole, the data are not compatible with an isotropic model. In agreement with this, Nakada et al. (1974) reported that the degree of polarization inferred from their measurements is about 10%.

# CHAPTER V

# X- AND GAMMA-RAY EVIDENCE FOR TWO PHASES OF ACCELERATION IN SOLAR FLARES

## A. Introduction

Extensive measurements of solar radio emissions, X-rays, and interplanetary energetic particles have firmly established the fact that charged particles are copiously accelerated in solar flares. Even though the detailed flare acceleration mechanisms are not known, the data tend to support the suggestion (Wild, Smerd and Weiss 1963, de Jager 1969, Frost and Dennis 1971) that the acceleration process consists of at least two phases. The first phase, or flash phase, accelerates mainly electrons up to energies of several hundred keV. These electrons produce Type III radio bursts, impulsive 10 to 100 keV X-ray emissions, microwave bursts, and EUV bursts (e.g., Kane 1974); streams of energetic electrons detected in interplanetary space are also believed to be due to this acceleration phase (Lin 1974). Because the total energy in electrons accelerated in the first phase constitutes a large fraction of the energy of the flare (Lin 1974, Hudson, Jones, and Lin 1975), only very efficient first order acceleration mechanisms can be responsible for this phase of acceleration.

The second phase of acceleration occurs in a smaller number of flares than does the first phase, and it accelerates ions to tens and hundreds of MeV and electrons to relativistic energies. This acceleration phase is associated with Type II and Type IV bursts, and produces the fluxes of ions and electrons of energies greater than several MeV observed in interplanetary space. The acceleration of the ions and the electrons in the second place is probably due to the passage of shock fronts in the solar atmosphere.

For the first time, detailed measurements in many energy bands (X-ray, gamma-ray, microwave, and EUV bands) are available for the August 4, 1972 flare, which lasted for $\sim 10^3$ seconds with highly structured time profiles of the radiations in these energy bands. For this reason many authors have sutdied this flare. Brown and Hoyng (1975) and Benz (1977) have studied the hard X-rays (measured by van Beek et al. 1973) from this flare with emphasis on the time profiles. Using the measurement (Chupp et al. 1973; 1975, Suri et al. 1975) of the gamma-ray emission from this flare in the 0.35 to 8 MeV region, Ramaty et al. (1975), Ramaty and Crannell (1976), and Wang and Ramaty (1974, 1975) have studied the implications of line emissions. Suri et al. (1975), Bai and Ramaty (1975, 1976), and Ramaty et al. (1977) have studied the implications of the X- and gamma-ray continuum. Lin and Hudson (1976) have studied the energetics of various phenomena of this flare, and many other authors have also studied various aspects of this flare.

In this chapter we show that unique information on the two phases of acceleration in solar flares can be obtained by treating the gamma-ray data together with the X-ray and microwave observations of the 1972, August 4 flare. A similar study has already been published (Bai and Ramaty 1975, 1976). However, Ramaty et al. (1977) have shown that the gamma-ray continuum due to Doppler broadening of gamma-ray lines produced by interactions of accelerated nuclei could account for all the continuum radiations in the 4 to 8 MeV region of the August 4, 1972 flare. Therefore, we closely reinvestigate the continuum radiation in the 0.35 to 8 MeV region, which shows the spectral flattening around 1 MeV, by taking the continuum due to nuclear gamma rays into account. From the deduced spectra of the accelerated electrons and the accelerated protons and the observed time profiles of the X-rays, gamma rays, and

microwave emissions of this flare, we suggest that the particle acceleration process of this flare consists of at least two phases.

In Section B we deduce the spectra of the accelerated electrons and the accelerated protons. We calculate photon spectra produced by electrons and protons with various spectra, and fold the resultant photon spectra into the response function of the gamma-ray detector of the New Hampshire group, and then choose the electron and proton spectra which give the best fit to the observed data. In Section C, by investigating the time profiles of the hard X-rays, the gamma rays, and the microwave emissions (Croom and Harris 1973), and we find some constraints for the acceleration mechanisms. In Section D we summarize our results.

## B. The Energy Spectrum of the Accelerated Electrons

In Chapter II we have discussed the formulas for e-p bremsstrahlung and e-e bremsstrahlung, and we have also discussed how to calculate the instantaneous photon production rate due to bremsstrahlung of the accelerated electrons with the isotropic momentum distribution. Though at low energies ($\ll mc^2$) e-e bremsstrahlung is negligible, at high energies it becomes comparable to e-p bremsstrahlung. In addition to bremsstrahlung, in the MeV range the gamma-ray continuum due to Doppler broadening of nuclear gamma-ray lines becomes important.

Figure 5.1 shows the hard X- and gamma-ray spectrum measured by van Beek et al. (1973) and by Chupp et al. (1975). The shaded area in this figure shows the range of variability of the observed hard X-ray flux in the time interval from 06:23 UT to 06:30 UT, and the error bars represent the average observed gamma-ray flux over the time interval from 06:24 UT to 06:33 UT. As can be seen, two sets of data agree reasonably well. Note here that the photon spectrum flattens above 1 MeV. The

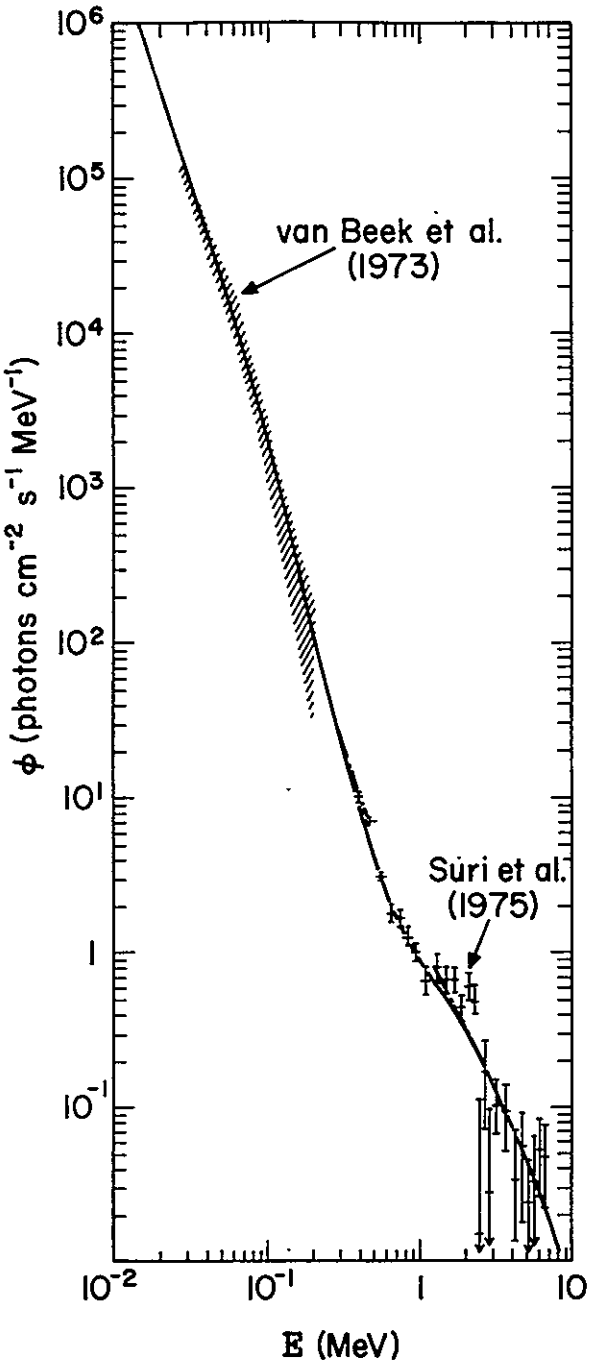


Figure 5.1. The observed hard X-ray and gamma-ray continuum from the 1972, August 4 flare. The shaded area is based on the data of van Beek et al. (1973) and includes all their spectra between 0623 and 0630 UT. The data points are from Suri et al. (1975). The solid line represents the bremsstrahlung spectrum calculated from the electron spectrum given by equation (5.1) (Bai and Ramaty 1976).

solid line represents the bremsstrahlung photon spectra calculated by using the following electron spectrum (Bai and Ramaty 1976):

$$nN(E) = \begin{cases} 3.3 \times 10^{44}\ E^{-2.4}, & E \leq 0.1\ \text{MeV} \\ 2.6 \times 10^{43}\ E^{-3.5}, & 0.1\ \text{MeV} < E \leq 0.8\ \text{MeV} \\ 1.4 \times 10^{42}\ \exp(-E/4), & E > 0.8\ \text{MeV} \end{cases} \tag{5.1}$$

However, this result was obtained without including the gamma-ray continuum due to nuclear gamma rays.

Nuclear interactions due to collisions of accelerated protons, alpha particles, and heavy ions with the ambient material produce nuclear gamma rays in the MeV region. Reactions due to energetic protons or alpha particles produce narrow lines with full widths at half maximum (FWHM) less than 150 keV; reactions due to energetic heavy ions give rise to broad lines with about 1 MeV FWHM, which overlap each other and make highly structured gamma-ray continuum. While the previous works (Ramaty et al. 1975 and references therein) mainly dealt with narrow lines, for the first time, Ramaty et al. (1977) have studied in detail the gamma-ray continuum due to nuclear interactions in solar flares. They have shown that the nuclear gamma-ray continuum not only can account for the total number of photons observed in the 4 to 8 MeV region from the August 4, 1972 flare but also can account for the observed shape of the continuum.

Therefore, Suri, Ramaty, and Bai (1977) extend the calculation of the gamma-ray continuum due to nuclear reactions down to 0.35 MeV, using the solar abundances given by Cameron (1973). Table 5.1 lists the various nuclear interaction modes included in the calculation and the corresponding gamma-ray energies. Table 5.2 gives abundances of various nuclei relevant to the calculation. The interaction cross

Table 5.1

Prompt gamma-ray lines (after Ramaty et al. 1975).

| Photon Energy (MeV) | Origin | Production Modes | Approximate Relative Intensity |
|---|---|---|---|
| 0.431 | $^{7}Be^{*0.431} \rightarrow$ g.s. | $^{4}He(\alpha,n)^{7}Be^{*0.431}$ | 1 |
| 0.478 | $^{7}Li^{*0.478} \rightarrow$ g.s. | $^{4}He(\alpha,p)^{7}Li^{*0.478}$<br>$^{4}He(\alpha,n)^{7}Be \xrightarrow{12\%} {}^{7}Li^{*0.478}$ | 1 |
| 0.72 | $^{10}B^{*0.72} \rightarrow$ g.s. | $^{12}C(p,2pn)^{10}B^{*0.72}$<br>$^{16}O(p,\ )^{10}B^{*0.72}$ | 0.1 |
| 0.845 | $^{56}Fe^{*0.845} \rightarrow$ g.s. | $^{56}Fe(p,p')^{56}Fe^{*0.845}$ | 0.2 |
| 1.24 | $^{56}Fe^{*2.08} \rightarrow {}^{56}Fe^{*0.845}$ | $^{56}Fe(p,p')^{56}Fe^{*2.08}$ | 0.2 |
| 1.38 | $^{24}Mg^{*1.37} \rightarrow$ g.s. | $^{24}Mg(p,p')^{24}Mg^{*1.37}$ | 0.1 |
| 1.63 | $^{20}Ne^{*1.63} \rightarrow$ g.s.<br>$^{14}N^{*3.94} \rightarrow N^{*2.31}$<br>$^{23}Na^{*2.07} \rightarrow {}^{23}Na^{*0.44}$ | $^{20}Ne(p,p')^{20}Ne^{*1.63}$<br>$^{14}N(p,p')^{14}N^{*3.94}$<br>$^{16}O(p,2pn)^{14}N^{*3.94}$<br>$^{24}Mg(p,2p)^{23}Na^{*2.67}$ | 0.2 |
| 1.78 | $^{28}Si^{*1.78} \rightarrow$ g.s. | $^{28}Si(p,p')^{28}Si^{*1.78}$ | 0.2 |
| 1.99 | $^{11}C^{*1.99} \rightarrow$ g.s. | $^{12}C(p,pn)^{11}C^{*1.99}$ | 0.07 |
| 2.31 | $^{14}N^{*2.31} \rightarrow$ g.s. | $^{14}N(p,p')^{14}N^{*3.94} \rightarrow {}^{14}N^{*2.31}$<br>$^{14}N(p,n)^{14}O \rightarrow {}^{14}N^{*2.31}$<br>$^{16}O(p,2pn)^{14}N^{*2.31}$ | 0.3 |
| 2.75 | $^{16}O^{*8.88} \rightarrow {}^{16}O^{*6.14}$ | $^{16}O(p,p')^{16}O^{*8.88}$ | 0.07 |
| ~3.62 | $^{13}C^{*3.68} \rightarrow$ g.s.<br>$^{6}Li^{*3.56} \rightarrow$ g.s. | $^{16}O(p,3pn)^{13}C^{*3.68}$<br>$^{12}C(p,\ )^{6}Li^{*3.56}$ | 0.07 |
| 3.84 | $^{13}C^{*3.85} \rightarrow$ g.s. | $^{16}O(p,3pn)^{13}C^{*3.84}$ | 0.07 |
| 4.43 | $^{12}C^{*4.43} \rightarrow$ g.s. | $^{12}C(p,p')^{12}C^{*4.43}$<br>$^{12}C(\alpha,\alpha')^{12}C^{*4.43}$<br>$^{16}O(p,p\alpha)^{12}C^{*4.43}$ | 1 |
| ~5.3 | $^{15}O^{*5.26} \rightarrow$ g.s.<br>$^{15}N^{*5.28} \rightarrow$ g.s.<br>$^{15}N^{*5.31} \rightarrow$ g.s. | $^{16}O(p,pn)^{15}O^{*5.26}$<br>$^{16}O(p,2p)^{15}N^{*5.28}$<br>$^{16}O(p,2p)^{15}N^{*5.31}$ | 0.3 |
| 6.14 | $^{16}O^{*6.14} \rightarrow$ g.s. | $^{16}O(p,p')^{16}O^{*6.14}$<br>$^{16}O(\alpha,\alpha')^{16}O^{*6.14}$ | 0.5 |
| 6.33 | $^{15}N^{*6.33} \rightarrow$ g.s. | $^{16}O(p,2p)^{15}N^{*6.33}$ | 0.5 |
| ~6.7 | $^{11}B^{*6.76} \rightarrow$ g.s. | $^{12}C(p,2p)^{11}B^{*6.76}$<br>$^{12}C(p,2p)^{11}B^{*6.81}$<br>$^{12}C(p,pn)^{11}C^{*6.50}$ | 0.07 |
| 7.12 | $^{16}O^{*7.12} \rightarrow$ g.s. | $^{16}O(p,p')^{16}O^{*7.12}$ | 0.2 |

Table 5.2.

Atomic abundances used for nuclear gamma-ray calculations.

| Nucleus | Relative abundance |
|---|---|
| H | 1.0 |
| He | 0.1 |
| C | $3.7 \times 10^{-4}$ |
| N | $1.2 \times 10^{-4}$ |
| O | $6.8 \times 10^{-4}$ |
| Ne | $1.1 \times 10^{-4}$ |
| Mg | $3.3 \times 10^{-5}$ |
| Si | $3.1 \times 10^{-5}$ |
| S | $1.6 \times 10^{-5}$ |
| Fe | $2.6 \times 10^{-5}$ |

sections and the method of calculation are well described in Ramaty et al. (1975, 1977), and the kinematics influencing the line broadening and the method how to fold a given photon spectrum into the response function of the gamma-ray detector of the New Hampshire group are discussed in Ramaty et al. (1977).

Figure 5.2 shows the observational data and the photon spectrum obtained from folding the nuclear gamma rays calculated as follows; We assume the momentum vectors of the accelerated nuclei are isotropic, and we use the differential energy spectra of the accelerated nuclei given by

$$N_i(E) = K_i E^{-2}, \tag{5.2}$$

where the subscript i denotes the species of the nuclei, $K_i$ is proportional to the atomic abundances listed in Table 5.2, and E is in units of MeV/nucleon. Here we use the spectrum $E^{-2}$, because it is deduced from the comparison between the observed and calculated gamma-rays (Ramaty et al. 1977). The histogram in the figure represents the data, and the solid dots represent the theoretical result due to nuclear gamma-rays. The figure shows that above ~2.5 MeV the continuum due to nuclear gamma-rays could account for the data. However, below this energy additional continuum radiation due to bremsstrahlung is necessary.

To the result due to nuclear gamma rays shown in Figure 5.2, we have added the contribution due to a power-law bremsstrahlung continuum which fits the data at low energies, and we find the result does not give a satisfactory fit to the data. To have a good fit, additional photons in the 1 to 2.5 MeV region are necessary. Thus, to account for the data, we need accelerated electrons with a spectrum other than a simple power-law spectrum. This result is in agreement with the previous

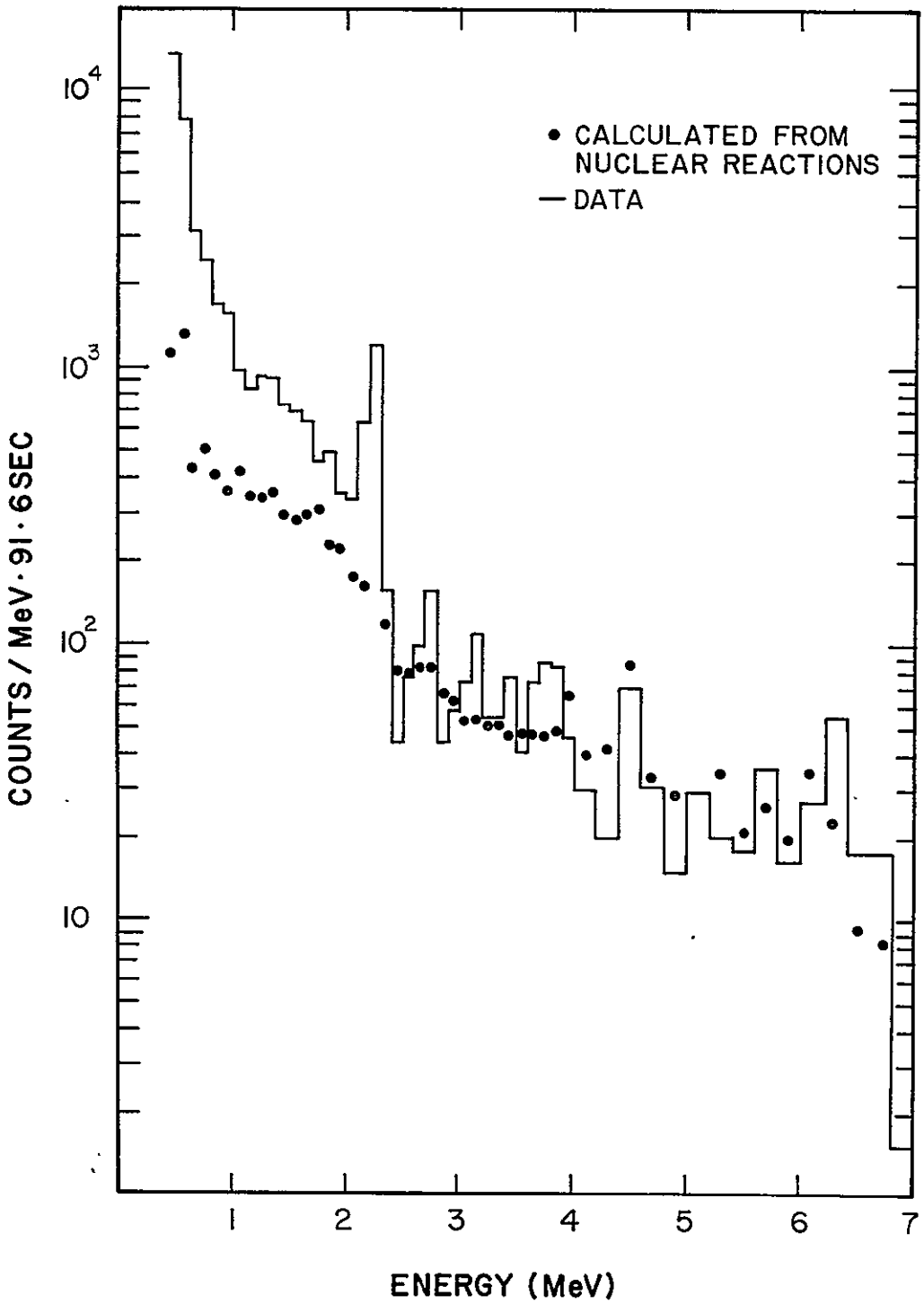


Figure 5.2. The gamma-ray counts from the 1972, August 4 flare measured by the New Hampshire group and the calculated nuclear gamma-ray counts. For solid dots, the calculated gamma-ray continuum is folded into the response function of the detector.

interpretation (Bai and Ramaty 1975, 1976). As we have seen in Chapter II, e-e bremsstrahlung contribution becomes important for mildly relativistic and relativistic energies. Including e-e bremsstrahlung, we calculate photon spectra due to various electron spectra. We find that the electron spectra which give good fits to the data should have the following characteristics: The electron spectrum consists of two distinctive components. The low energy component is in a form of a power-law spectrum which steeepens drastically at about 0.8 MeV; the high energy component is flat below about 4 MeV and decreases very rapidly above this energy.

Figure 5.3 shows the data and a theoretical result calculated from an electron spectrum given by

$$nN(E) = \begin{cases} 6.9 \times 10^{43}\ E^{-3.12} & 0.3\ \text{MeV} \leq E \leq 0.85\ \text{MeV} \\ 6.0 \times 10^{42}\ \delta(E - 3.5) & E > 0.85\ \text{MeV} \end{cases} \tag{5.3}$$

This spectrum is plotted in Figure 5.4. Here a delta-function spectrum is shown as a representative of the high energy component. Accelerated electrons are assumed to be isotropic. However, even if the assumption of isotropy is removed, the observed photon spectrum cannot be easily explained with one electron component with a smoothly varying spectrum.

The proton spectrum used in this calculation (deduced by Ramaty et al. 1977) is also shown in the figure. At high energies the proton number is much larger than the electron number. Though we have no direct information on accelerated protons at low energies $\lesssim 1$ MeV, considering the energetics, the proton number is likely to be comparable to or less than the electron number.

The peculiar shape of the electron spectrum is expected to be revealed in the microwave emission spectrum. Indeed the microwave spectrum measured by Croom

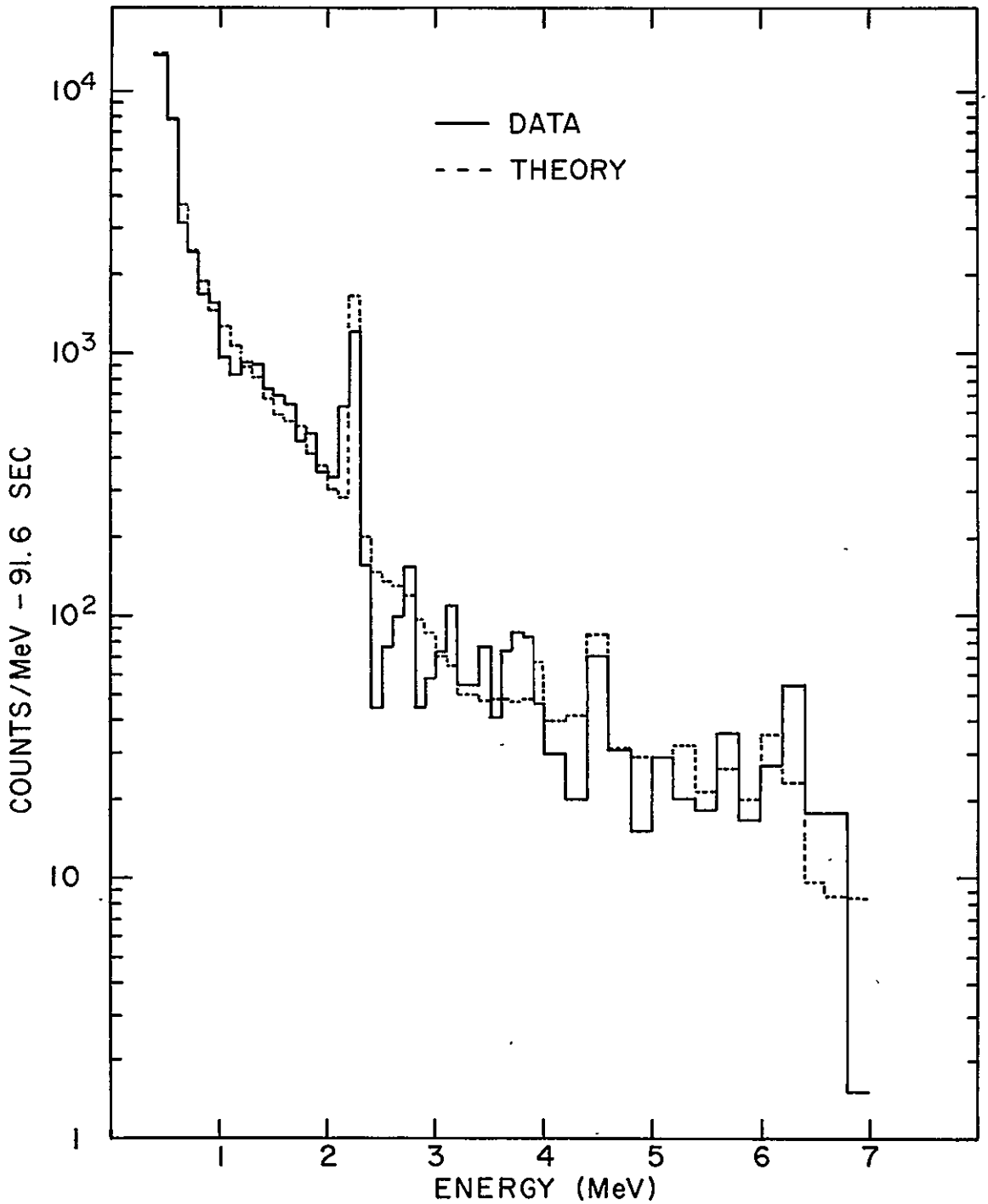


Figure 5.3. The gamma-ray counts from the August 4, 1972 flare and a theoretical fit to the data. The dashed line represents the theoretical counts calculated from the bremsstrahlung of the electron spectrum shown in Figure 5.4, in addition to the nuclear gamma-ray contribution shown in Figure 5.2.

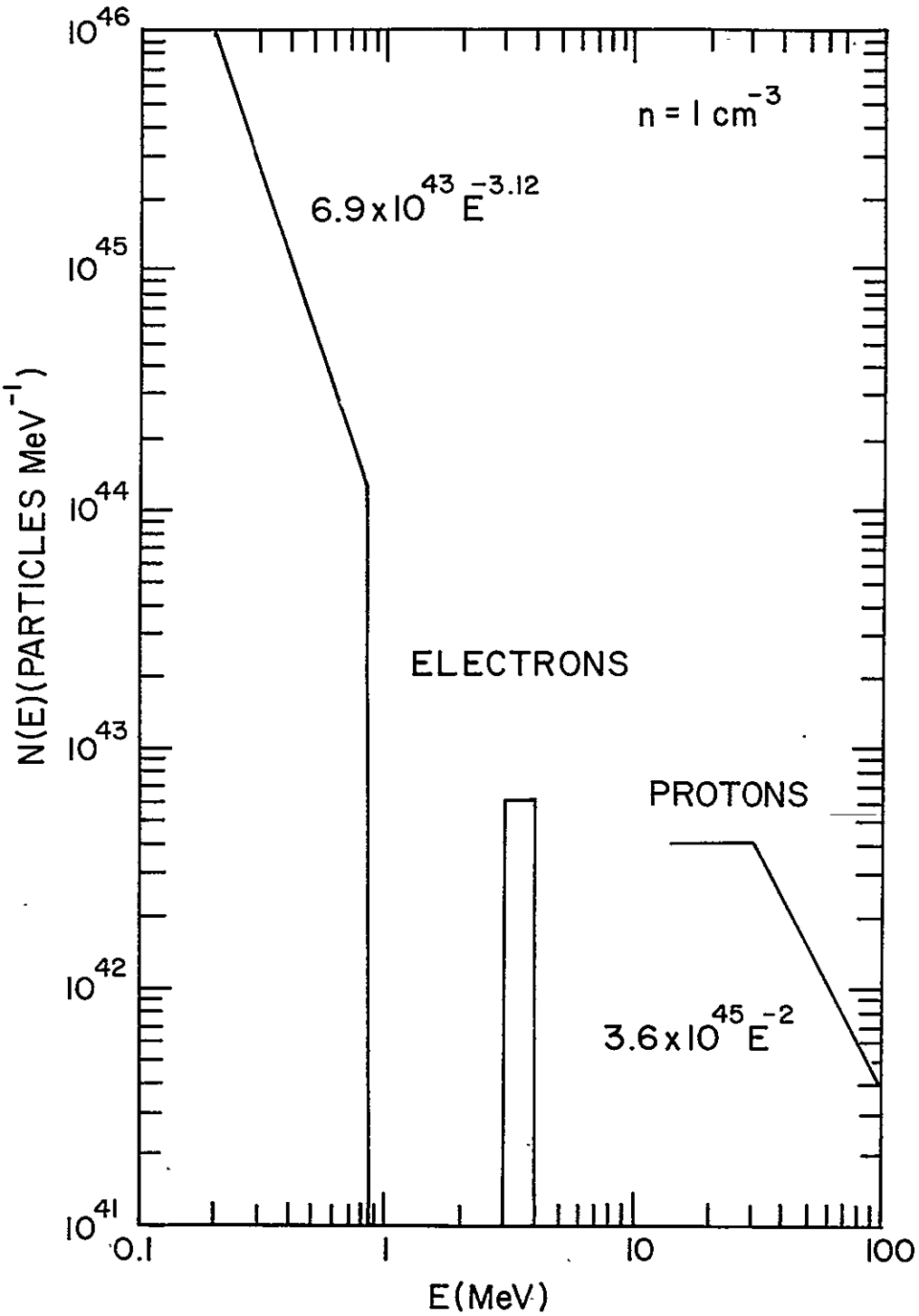


Figure 5.4. An electron spectrum which gives a best fit to the continuum data. The proton spectrum deduced by Ramaty et al. (1975) is also shown here.

and Harris (1973) shows a flattening at the frequency of about 37 GHz. Bai and Ramaty (1976) have shown that the spectrum and intensity of the observed microwave emissions can be consistently explained by the synchrotron radiation in the common emitting region by the same electrons producing hard X-rays. We can get a similar result by using the revised electron spectrum. Thus, the observed microwave spectrum renders more confidence to the two-component electron spectrum.

For the following reasons, we suggest that two phases of acceleration are responsible for the acceleration of particles for this flare: (1) It is very unlikely that the peculiar shape of the electron spectrum could be due to a single acceleration mechanism. (2) The accelerated electrons and protons have very differing energy spectra. It can also be shown that they have differing velocity spectra and rigidity spectra.

### C. Time Profiles of Radiation Intensities

The observed time dependences of the X-ray emission in the energy range 29 to 41 keV (van Beek et al. 1973), of the gamma-ray flux in the range 0.35 to 8 MeV (Suri et al. 1975), and of the microwave emission at 37 GHz (Croom and Harris 1973) are shown in Figure 5.5. The variation in time of the X-rays depends on the time profile of electrons of several tens of keV in the flare region. On the other hand, the time dependence of the gamma rays is determined by the temporal variation of electrons of energies greater than hundreds of keV; according to Bai and Ramaty (1976), radio emission at 37 GHz is also due to electrons in this energy range. Indeed, as seen in Figure 5.5, the general rise time of both the continuum gamma rays and 37 GHz radio emission ($\sim$4 minutes) is longer than that of the X-rays ($\sim$2 minutes). This result provides support to the suggestion made on the basis of spectral information in Section B, that electrons above several hundreds of keV are accelerated by a different

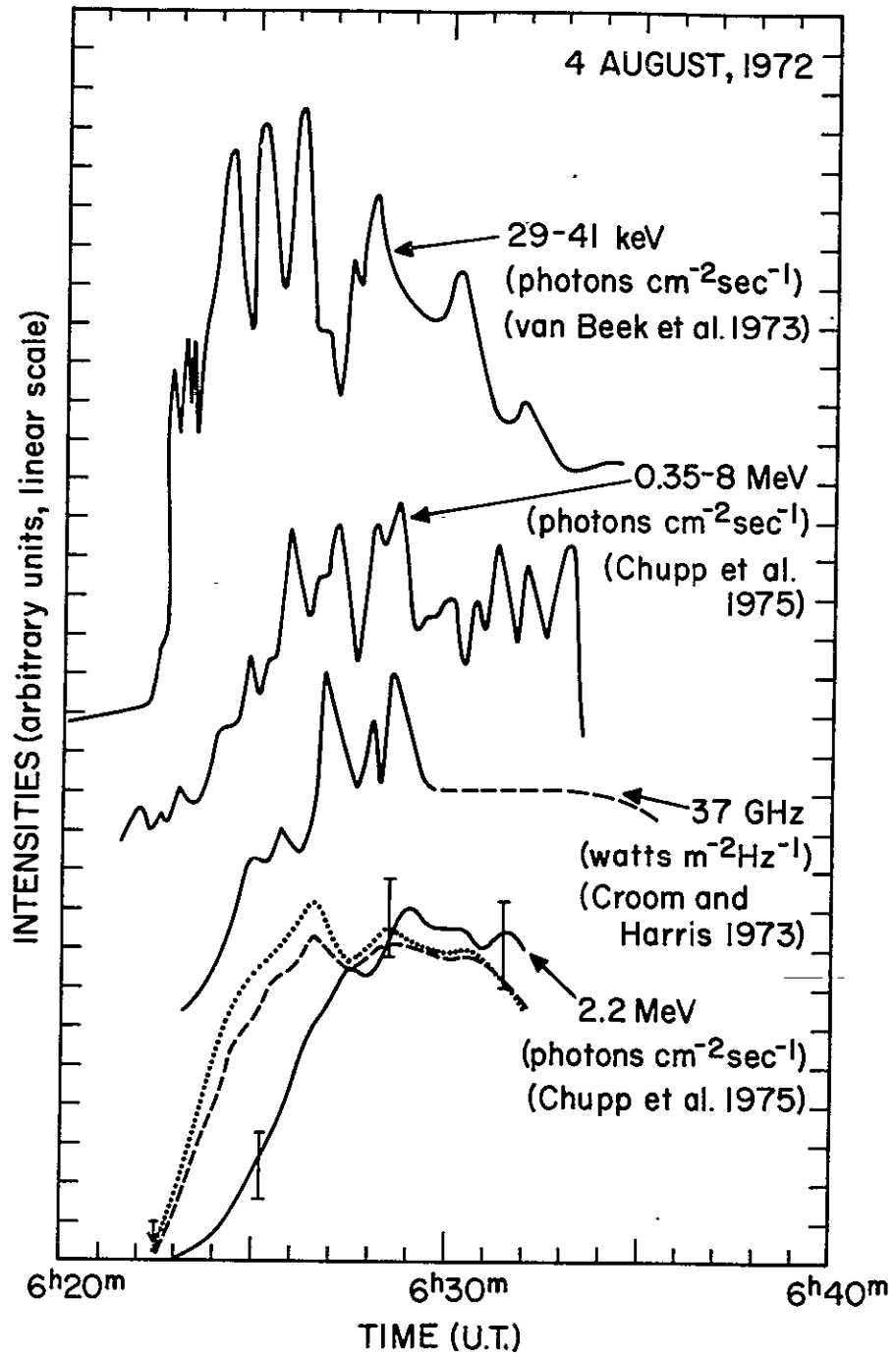


Figure 5.5. Time dependences of radiations of the 1972 August 4, flare. The three upper lines are the measured time profiles of X-rays (29 ~41 keV), gamma rays (0.35 ~8 MeV), and microwaves (37 GHz). The error bars in the lower part of the figure represent the measured intensities of the 2.2 MeV line. The solid, dashed, and dotted lines are calculated time profiles of the 2.2 MeV line. The solid line is obtained by assuming that the instantaneous number of nuclei in the flare region has the same time dependence as that of the observed 0.35 to 8 MeV gamma rays. The dashed and dotted lines are obtained by assuming that the time dependence of the nuclei is the same as that of the 29 to 41 keV X-rays. For the solid and dotted lines we used a photospheric $^3$He abundance $^3$He/H = 5 X $10^{-5}$; for the dashed line, $^3$He/H = 0.

mechanism than the mechanism which accelerates lower energy electrons. We should point out, however, that there is good observational correlation between the individual peaks of the X-ray, gamma-ray, and microwave time profiles, as can be seen in Figure 5.5. Therefore, the first-phase and second-phase acceleration mechanisms should be closely related. For example, the first-phase mechanism could serve as an injection source for the second mechanism. This possibility is supported by the total number of electrons in the two components: from Figure 5.4 we calculate that the number of electrons in the high-energy component is only 0.14% of the number of electrons in the lower energy component above 100 keV.

If different acceleration mechanisms are responsible for the acceleration of low- and high-energy electrons, it is of considerable interest to determine which of the two mechanisms accelerates protons and nuclei. The time profile of the nucleonic component in the flare region can be deduced directly from the observed time profile of the 2.2 MeV line. This line is due to the reaction $n + p \rightarrow d + \gamma$, where the neutrons are the products of nuclear reactions of energetic protons and nuclei in the flare region (Ramaty et al. 1975).

The error bars on the 2.2 MeV gamma-ray time profile shown in Figure 5.5 are the measured intensities of this line (Chupp et al. 1975). The solid, dashed, and dotted lines are calculated time profiles of the 2.2 MeV line obtained by using the results of Wang and Ramaty (1974). The solid line is obtained by assuming that the instantaneous number of nuclei in the flare region has the same time dependence as that of the observed 0.35 to 8 MeV gamma-rays. The dashed and dotted lines are obtained by assuming that the time dependence of the nuclei is the same as that of the 29 to 41 keV X-rays. For

the solid and dotted lines we used a photospheric $^3$He abundance, $^3He/H = 5 \times 10^{-5}$; for the dashed line, $^3He/H = 0$.

As can be seen, the measured time profile of the 2.2 line is in good agreement with the calculated result shown by the solid line. The dashed and dotted lines, however, give poorer fits to the data, independent of the amount of $^3$He in the photosphere. (A smaller amount of $^3$He in the photosphere results in a slower loss of neutrons and hence a longer delay of the 2.2 MeV line.) This result implies that the nuclei are probably accelerated by the second-phase mechanism.

By assuming that the hard X-and gamma-ray continuum and the microwave emission from the August 4, 1972 flare are due to the same accelerated electrons in the common emitting region, Bai and Ramaty (1976) have obtained the following parameters of the common emitting region: $B = 415$ gauss, $n = 7.1 \times 10^{10} cm^{-3}$, $T = 4.5 \times 10^6$ K. This method is unique. However, mainly because a uniform magnetic field is assumed and the background radiation at 71 GHz is large, the above parameters are uncertain--probably within a factor of 2. The changes in the values of the above mentioned parameters due to the revision of the electron spectrum made in the preceding section are estimated to be within the above-mentioned uncertainties. Therefore, we do not repeat the procedure to determine these parameters again. From statistically significant fine structures of the X-ray time profiles observed down to 1.2 seconds, the time resolution of the instrument, van Beek et al. (1973) concluded that the ambient density is larger than $3 \times 10^{10} cm^{-3}$, in consistence with Bai and Ramaty (1976).

At energies below $\sim 100$ keV, the collisional energy loss rate of electrons in the ionized hydrogen plasma is given by (Trubnikov 1965)

$$\frac{dE}{dt}(E) = -1.55 \times 10^{-13}\, nE^{-1/2} \text{ (MeV/sec)}, \tag{5.4}$$

and above 150 keV, it is given by (Ginzburg and Syrovatskii 1964)

$$\left.\frac{dE}{dt}(E)\right]_c = -3.8 \times 10^{-13}\ n(\mathrm{MeV/sec}), \tag{5.5}$$

where n is the number density per cm and E is in units of MeV. In the relativistic domain, energy loss rate due to synchrotron radiation becomes important, and it is represented by (Ginzburg and Syrovatskii 1964)

$$\left.\frac{dE}{dt}(E)\right]_s = -3.75 \times 10^{-9}\ B^2(E + .511)^2\ (\mathrm{MeV/sec}), \tag{5.6}$$

where B is in gauss. In the non-relativistic energies, the energy loss rate of protons is given by (Hayakawa and Kiato 1956)

$$\frac{dE}{dt}(E) = -8.4 \times 10^{-12}\ nE^{-1/2}\ (\mathrm{MeV/sec}), \tag{5.7}$$

and, below the energy where the proton velocity becomes equal to the thermal velocity of the ambient electrons, the energy loss rate of protons become constant (Ginzburg and Syrovatskii 1964).

Using the energy loss rates given above and the values of the flare parameters mentioned earlier and $T = 4.5 \times 10^6$ K (Bai and Ramaty 1976), we find the energy loss times, $E/(dE/dt)$, of electrons and protons, which are shown in Figure 5.6. It is noticeable that the energy loss times have very differing values at different energies. From this figure alone, we can see that a single acceleration mechanism is very unlikely to be responsible for the acceleration of particles over the entire energy region. For example, a Fermi type acceleration mechanism can be efficient at high energies where energy loss time is very large; on the other hand, such a mechanism cannot be efficient at low energies where energy loss time is very short.

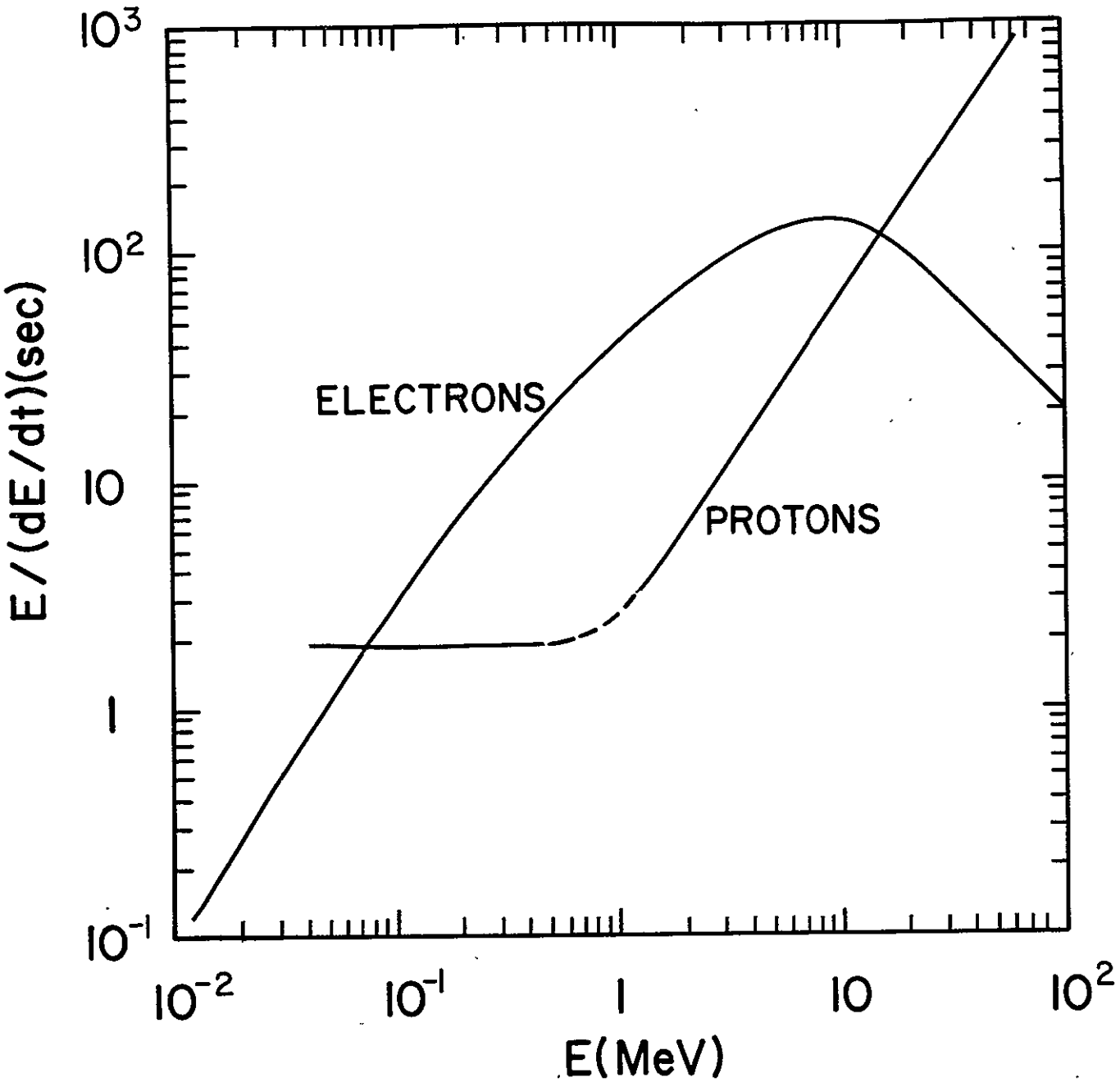


Figure 5.6. Energy loss times, E/(dE/dt), of electrons and protons in the medium with $n = 7.1 \times 10^{10}$ $cm^{-3}$, B = 415 gauss, and $T = 4.5 \times 10^6$K.

Whatever the acceleration mechanism is, the acceleration time should be shorter than the energy loss times. Otherwise, the acceleration mechanism cannot be efficient. Energy loss times of electrons with energies below 50 keV are shorter than about 1 second. Considering the rapid changes of the X-ray intensities observed in the time scale of 1.2 seconds, van Beek et al. (1973) concluded the acceleration time might be shorter than 1.2 seconds. Therefore, the characteristic time for the first phase acceleration is expected to be shorter than $\sim 1$ second.

Figure 5.7 shows the time profiles of X-ray intensities measured in several energy intervals (van Beek et al. 1973). Because electrons with energies below 50 keV have energy loss times shorter than 1 second (see Figure 5.6), in the time scales longer than 1 second, the time profile of the X-rays in the 29 to 41 keV interval reflects the time profile of the intensity of the electron acceleration rate. Though the time profiles of X-rays in the different energy bands, shown in this figure, are quite similar to each other, a delay of temporal features, increasing with increasing energy, can be noticed. This delay was also noticed by Hoyng (1975) and by Benz (1977). It was also reported that the X-ray spectrum is flatter at flux minima than at flux maxima (Brown and Hoyng 1975, Benz 1976). Though these authors gave different interpretations, one of the simplest interpretations of these characters is that these are due to the increasing energy loss times with increasing energy. With this interpretation, the above-mentioned characters are compatible with the earlier interpretation that the acceleration time is less than 1 second.

## D. Summary and Conclusion

We have performed a detailed study of the observed spectrum of the hard X-and gamma-ray continuum of the August 4, 1972 flare, by using an accurate e-e

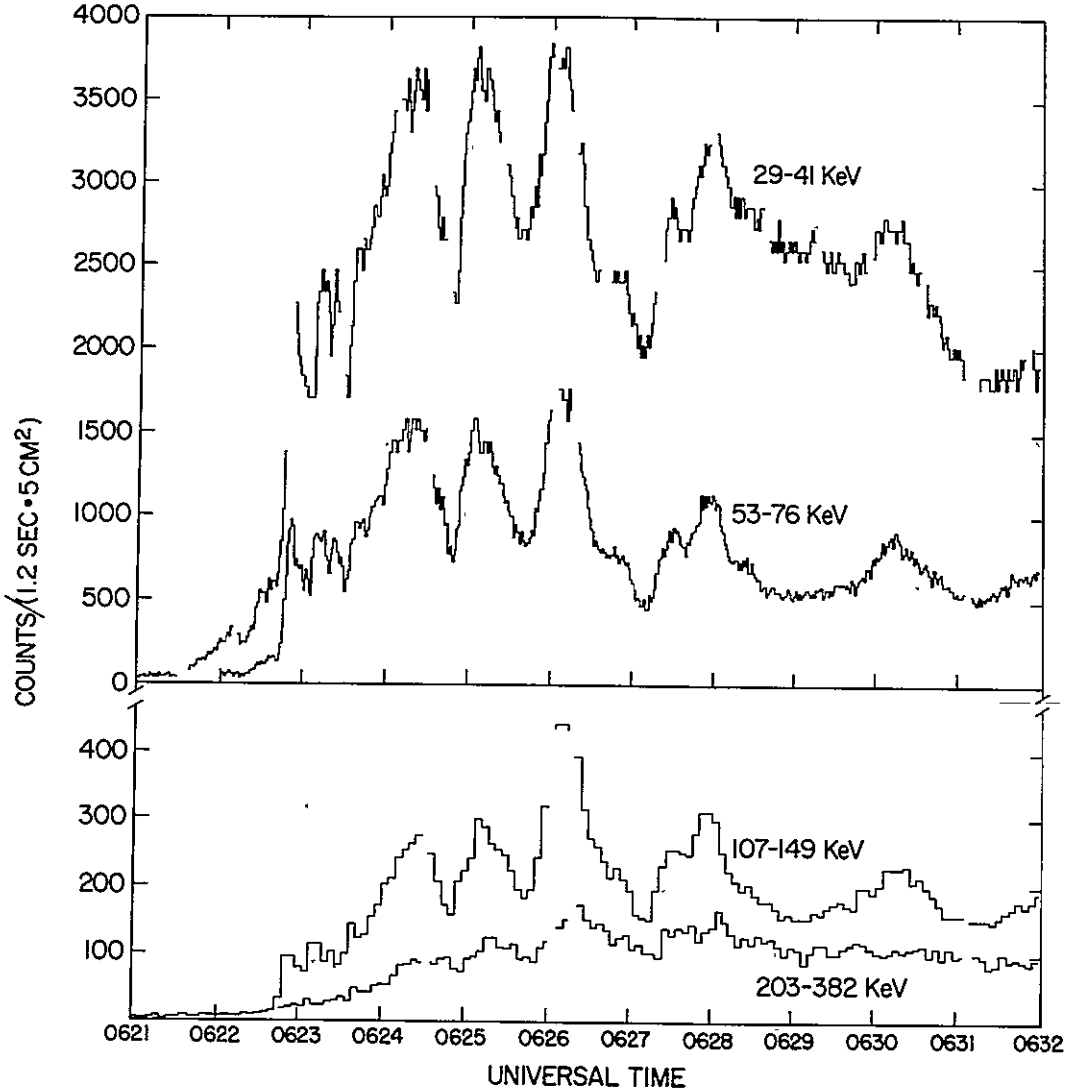


Figure 5.7. Observed count rates for the 1972, August 4 flare. The time resolution is 1.2 seconds for the top two curves and 4.8 seconds for the bottom two curves. The bottom curve is multiplied by two. (Digital data of the Utrecht group are used from the courtesy of Peter Hoyng.)

bremsstrahlung cross section and taking the nuclear gamma-ray continuum into account. The deduced electron spectrum consists of two distinct components, and this spectrum is compatible with the observed microwave data. This spectrum supports the suggestion (Wild et al. 1963, de Jager 1969, Frost and Dennis 1971) of two acceleration phases. The two-phase acceleration theory is also supported by the study of time dependences. For the August 4, 1972 flare, the first phase accelerates electrons (and probably protons also) up to several hundred keV; the second phase accelerates electrons to at least several MeV. The above interpretation is basically the same as the previous interpretation (Bai and Ramaty 1975, 1976).

The observed time profile of the 2.2 MeV gamma-ray line is consistent with the assumption that the number of accelerated nuclei has the same time dependence as the electron number at energies greater than several hundred keV. On the other hand, the 2.2 MeV time profile calculated by assuming that the nuclei have a similar time dependence as the X-rays below $\sim 100$ keV, precedes the data by about 100 seconds. This result supports the idea that the second phase accelerates protons to tens and hundreds of MeV. From the comparison of the electron and proton spectra, we can know that the second phase accelerates much larger number of protons than electrons (compared at the same energies, it is $\sim 100:1$), and this agrees with the interplanetary observations of flare-associated particles (Datlowe 1971, Simnett 1974).

The energy deposited in the flare medium by electrons accelerated in the first phase is of the order of $10^{32}$ ergs, and it is enough to cause other flare phenomena, such as EUV, UV, and optical radiations and also shock waves (Lin and Hudson 1976). According to these authors, above a certain height, the energy input to the flare medium by the electrons accelerated in the first phase cannot be balanced by cooling due to

various cooling mechanisms. Thus, the medium above this height "boils", and consequently shock waves are generated. The shock fronts and the turbulence due to the passage of shock fronts can serve as the second phase acceleration mechanism. This model is compatible with the study of this chapter.

# CHAPTER VI

## SUMMARY AND CONCLUSION

In Chapter I we have described the historical perspective of the work of this thesis by reviewing the history of solar hard X-ray research. In Chapter II, by comparing various production mechanisms of hard X-rays and gamma-rays, we have shown that the inverse Compton scattering of photospheric photons by relativistic electrons and bremsstrahlung due to collisions of accelerated protons with the ambient electrons are not important in solar flares. We have devoted most of Chapter II to the discussion of various properties of e-p and e-e bremsstrahlung, which is the most important production mechanism of solar hard X-rays. By integrating the e-e bremsstrahlung cross section over the photon emission angle, we have tabulated the e-e bremsstrahlung cross section with respect to photon and electron energies. In order to fully understand the properties of continuum radiation in the transition region from nonrelativistic to relativistic electron energies, it is necessary to include the e-e bremsstrahlung contribution. In this chapter we have also calculated photon spectra due to isotropic electrons with power-law energy spectra.

In Chapter III we have shown that the anisotropy, polarization, and Compton backscatter of solar hard X-rays are interrelated and therefore should be studied together in a coherent fashion. The effect of Compton backscatter is not appreciable for isotropic primary sources. However, this effect is significant for anisotropic sources which radiate predominantly downward. Because of this effect, the large limb brightening which was expected for such anisotropic sources disappears, and for such anisotropic sources the photon spectrum in the 15 to 50 keV range becomes steeper

as the heliocentric angle of the flare increases. The limb steepening of the X-ray spectrum is compatible with the observations of Datlowe et al. (1974). The observed X-rays due to an isotropic, unpolarized primary source are slightly polarized due to Compton backscatter: The degree of polarization does not exceed 4%. However, for anisotropic sources due to accelerated electrons with anisotropic distributions, the observed X-rays are highly polarized. For the anisotropic electron distribution we have used in this thesis, the degree of polarization of observed X-rays with energies between about 15 and 30 keV can be as large as 60% for limb flares.

By investigating the differential reflectivity as a function of incident X-ray beam direction, in Chapter III we have also discussed the information that can be obtained from detailed measurements of the surface brightness of the albedo patch. The height and degree of anisotropy of the primary X-ray source might be deduced from such studies.

In Chapter IV we have discussed how to utilize future albedo measurements with detectors having good spatial resolution. We have shown that heights ranging from $3 \times 10^8$ cm to $10^{10}$ cm could be deduced by using the Hard X-ray Imaging Spectrometer to be flown on board the SMM. We have also discussed the implications of polarized data. The existing polarization data suggest that hard X-rays around 15 keV are due to anisotropic distribution of accelerated electrons.

In Chapter V we have carefully analyzed the X-and gamma-ray continuum of the August 4, 1972 flare, by taking e-e bremsstrahlung and nuclear gamma-ray continuum into consideration. This spectrum shows a pronounced flattening at 1 MeV. By folding the calculated photon spectrum into the response function of the detector which measured the continuum of this flare and comparing with the measurement, we

have deduced the electron spectrum that can best explain the observation. We then have provided the deduced two-component electron spectrum as evidence for the two-phase acceleration theory. We have also shown that the time dependences of radiations from this flare support the two-phase acceleration theory. The spectral and temporal evidence we have given is the most direct evidence for this theory among the observational evidence given so far.

In this thesis solar hard X-rays with energies greater than 15 keV are implicitly assumed to be nonthermal in nature. Even though they may be tentative, the existing polarization data support this assumption. Statistically significant fine structures in the X-ray time profiles observed (by the Utrecht group; Hoyng 1975) down to 1.2 seconds, the time resolution of the instrument, and very good temporal correlations with other nonthermal radiations (UV, EUV, white light, microwave, and gamma-radiation) are best explained by the nonthermal interpretation. The lack of the effect of hard X-ray limb brightening is not contradictory to this interpretation, and the limb steepening of the X-ray spectrum is better explained by the downward anisotropic model. However, there is a class of flares whose X-ray spectra up to several tens of keV resemble thermal spectra and whose rises and decays are symmetric. Hard X-rays with energies up to several tens of keV from such flares may be due to a thermal plasma (Matzler 1977, private communication).

The aim of the study of solar hard X-rays and gamma-rays is to enhance the knowledge on the properties of accelerated flare particles and of the medium of the emitting region and thereby ultimately to understand the acceleration mechanisms. To pursue this aim effectively, complementary to the experiments which will be flown on board the SMM, measurements of hard X-ray polarization and of microwave emissions

at frequencies greater than about 50 GHz are badly needed. To determine the nature of solar hard X-rays and to find out the direction and degree of anisotropy of accelerated electrons, it is better to have simultaneous measurements of albedo and polarization of hard X-rays, which can complement each other. The polarimeters by Tindo and his co-workers did not function at the optimum condition. Reliable measurements of polarization not only can determine the nature (thermal or nonthermal) of solar hard X-rays conclusively, but also can give detailed information on the directionality of accelerated electrons when they complement with simultaneous albedo measurements.

Detailed measurements of time profiles of X- and gamma-rays can also further our understanding of accelerated flare particles. A hard X-ray detector with time resolution down to $10^{-3}$ seconds (Frost 1976) and a gamma-ray detector which can give better time profiles than the previous one (Chupp 1976) will be flown on board the SMM. However, because solar gamma-ray fluxes are low, the time resolution achievable in the gamma-ray measurements cannot be very good. On the other hand, the microwave emissions at frequencies greater than about 50 GHz, which are believed to be due to synchrotron radiation of relativistic electrons in the flare, can provide much better time profiles. Such time profiles can give information on the relativistic electrons which are thought to be accelerated in the second phase.

## APPENDIX A

## THE ANGLE BETWEEN THE SCATTERING PLANE AND THE NORMAL PLANE OF THE SCATTERED PHOTON

Let the reference frame S be the frame where the direction of propagation of the initial photon is along the Z-axis and the normal to the photosphere is in the X-Z plane. In this frame the momentum vector of the initial photon, $\vec{k}_1$, the momentum vector of the scattered photon, $\vec{k}_2$, and the normal vector $\vec{n}$ are expressed as follows:

$$\vec{k}_1 = k_1(0, 0, 1) \tag{A.1}$$

$$\vec{k}_2 = k_2 (\sin\theta_s \cos\theta_s, \sin\theta_s \sin\phi, \quad \cos\theta_s), \tag{A.2}$$

$$\vec{n} = (-\sin\theta_1, 0, \cos\theta_1). \tag{A.3}$$

The angle between $\vec{n}$ and $\vec{k}_2$ is given by

$$\cos\theta_2 = \vec{n} \cdot \vec{k}_2/k_2 = \cos\theta_1 \cos\theta_s - \sin\theta_1, \sin\theta_s \cos\phi_s \,. \tag{A.4}$$

The normal to the $\vec{k}_1$- $\vec{k}_2$ plane is

$$\vec{A} = (\vec{k}_1 \times \vec{k}_2)/(k_1 k_2 \sin\theta_s) = (-\sin\theta_s, \cos\theta_s, 0). \tag{A.5}$$

The normal to the $\vec{k}_2$- $\vec{n}$ plane is

$$\begin{aligned} \vec{B} &= (\vec{k}_2 \times \vec{n})/(k_2 \sin\theta_2) \\ &= (\cos\theta_1 \sin\theta_s \sin\phi_s, - \cos\theta_s \sin\theta_1 - \cos\theta_1 \sin\theta_s \cos\phi_s, \sin\theta_1 \sin\theta_s \sin\phi_s)/\sin\theta_2. \end{aligned} \tag{A.6}$$

The angle between the $\vec{k}_1$ - $\vec{k}_2$ plane and the $\vec{k}_2$ - $\vec{n}$ plane, $\alpha$, is given by

$$\cos\alpha = \vec{A} \cdot \vec{B} = -(\sin\theta_1 \cos\theta_s \cos\phi_s + \cos\theta_1 \sin\theta_s)/\sin\theta_2. \tag{A.7}$$

$$\sin\alpha = |\vec{A} \cdot \vec{B}| = \sin\phi_s \sin\theta_1/\sin\theta_2. \tag{A.8}$$

## APPENDIX B

## MONTE CARLO METHODS

Because explanations of Monte Carlo methods are available in many books, here we give only a brief explanation. The essence of the Monte Carlo method is to generate values of x which are distributed according to the distribution function y = f(x) in the interval between a and b. The often used method is to invert the integral of the distribution function:

Let

$$F(x) = \int_a^x f(x)dx \Big/ \int_a^b f(x)dx. \tag{B. 1}$$

Then the desired values of x are obtained by

$$x = F^{-1}(R), \tag{B. 2}$$

where the values of R are chosen to have a uniform distribution in the interval from 0 to 1.

If the distribution function f(x) is not easily integrable and the value of f(x) does not change drastically in the interval between a and b, the following method is more convenient. Generate a set of two independent random numbers ($R_1$, $R_2$) which runs from 0 to 1, and generate the following two numbers:

$$x_1 = (b - a)R_1 + a, \tag{B. 3}$$

$$y_1 = y_m \cdot R_2, \tag{B. 4}$$

where $y_m$ is the maximum of f(x) in the interval between a and b. The many sets of numbers ($x_1$, $y_1$) corresponding to many sets of random numbers ($R_1$, $R_2$)

define points which are uniformly distributed in the rectangle made of the following four lines:

$$x = a, x = b, y = 0, y = y_m.$$

By choosing only the sets $(x_1, y_1)$ which satisfy the condition

$$y_1 < f(x_1), \tag{B. 5}$$

we obtain values of $x$ which are distributed according to the distribution function $f(x)$ in the interval from $a$ to $b$.

## APPENDIX C

## THE REFLECTION PROBABILITY DUE TO THE SINGLE SCATTERING

The probability for a photon incident upon the photosphere with energy $\epsilon_o$ along the direction $(\theta_o, \phi_o = 0)$ to be backscattered out of the photosphere along the direction $(\theta, \phi)$ due to a single scattering is given as follows: The probability for this photon to traverse X(H-atoms/cm$^2$) without scattering is

$$P_a = \exp\left[-(\sigma_c + \sigma_a)X\right]. \tag{C.1}$$

The probability for this photon to experience a Compton scattering in the distance dx along the direction $(\theta, \phi)$ is

$$P_b = \frac{d\sigma_c}{d\Omega}(\epsilon_o, \theta_s(\theta_o, \theta, \phi), \phi_s)dX. \tag{C.2}$$

The probability for the photon to escape from the photosphere after the Compton scattering without further scattering is

$$P_c = \exp\left[-(\sigma_c + \sigma_a)\, X\left(\frac{-\cos\theta_o}{\cos\theta}\right)\right]. \tag{C.3}$$

By multiplying equations (C.1), (C.2), and (C.3) and integrating over x from 0 to $\infty$, we get

$$P^1(\epsilon_o, \theta_o, \theta, \phi) = \frac{1}{\sigma_c(\epsilon_o) + \sigma_a(\epsilon_o)} \frac{d\sigma_c}{d\Omega}(\epsilon_o, \theta_s(\theta_o, \theta, \phi), \phi_s) \cdot \frac{1}{1 + \frac{-\cos\theta_o}{\cos\theta}}, \tag{C.4}$$

where $\cos\theta_s = \cos\theta_0 \cos\theta + \sin\theta_0 \sin\theta \cos\phi$.

We have already discussed in Section III.B how to find the Stokes parameters after the scattering. Since we know the reflection probability due to a single scattering, we can find the degree of polarization of photons reflected (due to a single scattering) along a given direction, by numerically integrating over the incident direction.

## REFERENCES


Akhiezer, A. I. and Berestetskii, V. B.: 1965, Quantum Electrodynamics, Interscience Publisher, New York.

Allen, C. W.: 1964, Astrophysical Quantities, 2nd edition, Athlone Press, London.

Bai, T. and Ramaty, R.: 1975, Conference Papers, 14th International Cosmic Ray Conference, Munich, W. Germany, p. 1662.

Bai, T. and Ramaty, R.: 1976, Solar Phys. 49, 343.

Beigman, I. L.: 1975, Sov. Astron. 18, No. 5, 600.

Benz, A. O.: 1977, Astrophys. J. 211, 270.

Bethe, H. A. and Heitler, W.: 1934, Proc. Roy. Soc. (London) A 146, 83.

Boldt, E. A. and Serlemitsos, P. J.: 1969, Astrophys. J. 157, 557.

Brown, J. C.: 1971, Solar Phys. 18, 489.

Brown, J. C.: 1972, Solar Phys. 26, 441.

Brown, J. C.: 1975, Proc. of IAU/COSPAR Symposium. No. 68, Solar Gamma-, X- and EUV Radiations, edited by S. Kane, p. 245.

Brown, J. C. and Hoyng, P.: 1975, Astrophys. J. 200, 734.

Brown, J. C. and McClymont, A. N.: 1975, Solar Phys. 41, 135.

Brown, J. C., McClymont, A. N., and McLean, I. S.: 1974, Nature 247, 448.

Brown, J. C., van Beek, H. F., and McClymont, A. N.: 1975, Astron. Astrophys. 41, 395.

Cameron, A. G. W.: 1973, Space Sci. Rev. 15, 121.

Chubb, T. A.: 1972, Solar Terrestrial Physics/1970, Pt. I, edited by E. R. Dyer, D. Reidel Publishing Co., Holland.

Chubb, T. A., Friedman, H., and Kreplin, R. W.: 1960, J. Geophys. Res. 65, 1831.

Chupp, E. L.: 1976, in "A Brief Summary of the Solar Maximum Mission," GSFC X-682-76-238.

Chupp, E. L., Forrest, D. J., Higbie, P. R., Suri, A. N., Tsai, C., and Dunphy, P. P.: 1973, Nature 241, 333.

Chupp, E. L., Forrest, D. J., and Suri, A. N.: 1975, Proc. of IAU/COSPAR Symposium No. 68, Solar Gamma-, X- and EUV Radiations, edited by S. Kane, p. 341.

Cline, T. L. and McDonald, F. B.: 1968, Solar Phys. 5, 507.

Colgate, S. A., Audouze, J., and Fowler, W. A.: 1977, to be published.

Croom, D. L. and Harris, L. D. J.: 1973, World Data Center Report UAG-28, Pt. I., p. 210.

Datlowe, D. W.: 1971, Solar Phys. 17, 436.

Datlowe, D. W., Elcan M. J., and Hudson, H. S.: 1974, Solar Phys. 39, 155.

Datlowe, D., L'Heureux, J., and Meyer, P.: 1970, Acta Phys. Hung. 29, Suppl. 1.

Datlowe, D. W., O'Dell, Sl. L., Peterson, L. E., and Elcan, M. J.: 1977, Astrophys. J. 212, 561.

De Jager, C.: 1969, Cospar Symposium on Solar Flares and Space Research, edited by C. De Jager and Z. Svestka (Amsterdam: North-Holland Publishing), p. 1.

De Jager, C.: 1976, in "A Brief Summary of the Solar Maximum Mission," GSFC X-682-76-238.

Dillworth, C., Maccagni, D., Perotti, F., Tanzi, E. G., Mercier, J. P., Raviart, A., Treguer, L., and Gros, M.: 1972, Solar Phys. 23, 487.

Elwert, G.: 1968, Structure and Development of Solar Active Regions, edited by K. O. Krepenheuer, IAU Symp. 35, 444.

Elwert, G. and Haug, E.: 1970, Solar Phys. 15, 234.

Feenberg, E. and Primakoff, H.: 1948, Phys. Rev. 73, 449.

Felten, J. E. and Morrison, P.: 1966, Astrophys. J. 146, 686.

Fireman, E. L.: 1974, Ap. J. 187, 57.

Frost, K. J.: 1976, in "A Brief Summary of the Solar Maximum Mission," GSFC X-682-76-238.

Frost, K. J. and Dennis, B. R.: 1971, Astrophys. J. 165, 655.

Gingerich, O., Noyes, R. W., Kalkofen, W., and Chuy, K.: 1971, Solarphys. 18, 347.

Ginzburg, V. L. and Syrovatskii, S. I.: 1964, The Origin of Cosmic Rays, Macmillan and Co., New York.

Gluckstern, R. L. and Hull, M. H.: 1953, Phys. Rev. 90, 1003.

Gruber, D. E., Peterson, L. E., and Vette, J. I.: 1973, High Energy Phenomena on the Sun, edited by R. Ramaty and R. G. Stone, NASA SP-342 (National Aeronautics and Space Administration, Washington, D.C.), p. 147.

Haug, E.: 1972, Solar Phys. 25, 425.

Haug, E.: 1975, Z. Naturforsch. 30a, 1099.

Hayakawa, S. and Kiato, K.: 1956, Prog. Theo. Phys. 16, No. 2, 139.

Henoux, J. C.: 1975, Solar Phys. 42, 219.

Heitler, W.: 1933, Z. Physik 84, 145.

Heitler, W.: 1949, The Quantum Theory of Radiation. 2nd edition, Oxford University Press, London, p. 161.

Hodes, I.: 1953, Ph.D. Thesis, University of Chicago.

Holt, S. S.: 1974, High Energy Quanta in Astrophysics, edited by F. B. McDonald and C. E. Fichtel, MIT Press, p. 312.

Holt, S. S. and Cline, T. L.: 1968, Astrophys. J. 154, 1027.

Holt, S. S. and Ramaty, R.: 1969, Solar Phys. 8, 119.

Hoyng, P.: 1975, Ph.D. thesis, University of Utrecht, the Netherlands.

Hudson, H. S., Jones, T. W., and Lin, R. P.: 1975, Proc. of IAU/COSPAR Symposium No. 68, Solar Gamma-, X-, and EUV Radiations, edited by S. Kane, p. 425.

Jackson, J. D.: 1962, Classical Electrodynamics, John Wiley and Sons, New York.

Kane, S. R.: 1971, Astrophys. J. 170, 587.

Kane, S. R.: 1973, Symp. on High Energy Phenomena on the Sun, edited by R. Ramaty and R. G. Stone, GSFC X-693-73-193, p. 55.

Kane, S. R.: 1974, Coronal Disturbances, IAU Symposium No. 57 (D. Reidel, Dordrecht--Holland), p. 105.

Kane, S. R. and Anderson, K. A.: 1970, Astrophys. J. 162, 1003.

Karzas, W. J. and Latter, R.: 1961, Ap. J. Suppl. 6, 167.

Klein, O. and Nishina, Y.: 1929, Z. Physik. 52, 853.

Koch, H. W. and Motz, J. W.: 1959, Rev. Modern Phys. 31, 920.

Korchak, A. A.: 1967, Soviet Phys. -Dokl. 12, 192.

Langer, S. H. and Petrosian, V.: 1977, Astrophys. J. (to be published).

Lin, R. P.: 1974, Space Sci. Rev. 16, 189.

Lin, R. P. and Hudson, H. S.: 1976, preprint.

May, M. M.: 1951, Phys. Rev. 84, 265.

Maxon, M. S. and Corman, E. G.: 1967, Phys. Rev. 163, No. 1, 156.

McDonald, F. B., Fichtel, C. E., and Fisk, L. A.: 1974, High Energy Particles and Quanta in Astrophys., edited by F. B. McDonald and C. E. Fichtel, MIT Press.

McMaster, W. H.: 1961, Rev. Mod. Phys. 33, 8.

Meliorensky, A. S., Pissarenko, N. F., Shamolin, W. M., Likin, O. B.: 1975, Astron. and Astrophys. 41, 379.

Milkey, R. W.: 1971, Solar Phys. 16, 465.

Nakada, M. P., Neupert, W. M., and Thomas, R. J.: 1974, Solar Phys. 37, 429.

Ohki, K.: 1969, Solar Phys. 7, 260.

Peterson, L. E., Datlowe, D. W., and McKenzie, D. L.: 1973, Symp. on High Energy Phenomena on the Sun, edited by R. Ramaty and R. G. Stone, GSFC X-693-73-193, p. 132.

Peterson, L. E. and Winckler, J. R.: 1959, J. Geophys. Res. 64, 697.

Petrosian, V.: 1973, Ap. J. 186, 291.

Pinter, S.: 1969, Solar Phys. 8, 149.

Pizzichini, G., Spizzichino, A., and Vespignani, G. R.: 1974, Solar Phys. 35, 431.

Ramaty, R. and Crannell, C. J.: 1976, Astrophys. J. 203, 766.

Ramaty, R., Kozlovsky, B., and Lingenfelter, R. E.: 1975, Space Sci. Rev. 18, 341.

Ramaty, R., Kozlovsky, B., and Suri, A. N.: 1977, Astrophys. J. (to be published).

Santangelo, N., Horstman, H., and Horstman-Moretti, E.: 1973, Solar Phys. 29, 143.

Shklovskii, I. S.: 1965, Soviet Astron. A. J. 8, 538.

Simnett, G. M.: 1972, Solar Phys. 22, 189.

Simnett, G. M.: 1973, High Energy Phenomena on the Sun, edited by R. Ramaty and R. G. Stone, GSFC X-693-73-193.

Simnett, G. M.: 1974, Space Sci. Rev. 16, 257.

Sullivan, J. D.: 1970, Ph. D. Thesis, University of Chicago.

Suri, A. N., Chupp, E. L., Forrest, D. J., and Reppin, C.: 1975, Solar Phys. 43, 415.

Svestka, Z.: 1976, Solar Flares, Reidel Publishing Co., Dordrecht--Holland.

Takakura, T.: 1967, Solar Phys. 1, 304.

Takakura, T. and Kai, K.: 1966, Publ. Astron. Soc. Japan 18, 57.

Takakura, T., Ohki, K., Shibuya, N., Fujii, M., Matsuoka, M., Miyamoto, S., Nishimura, J., Oda, M., Ogawara, Y., and Ota, S.: 1971, Solar Physics 16, 454.

Tindo, P. I., Ivanov, V. D., Mandel'stam, S. L., and Shuryghin, A. I.: 1970, Solar Phys. 14, 204.

Tindo, I. P., Ivanov, V. D., Mandel'stam, S. L., and Shuryghin, A. I.: 1972, Solar Phys. 24, 429.

Tindo, I. P., Ivanov, V. D., Valnicek, B., Livshits, M. A.: 1972, Solar Phys. 27, 426.

Tindo, I. P., Mandelstam, S. L., Shuryghin, A. I.: 1973, Solar Phys. 32, 46 p.

Tomblin, F. F.: 1972, Ap. J. 171, 377.

Trubnikov, B. A.: 1965, Rev. Plasma Phys. 1, 105.

van Beek, H. F., Hoyng, P., and Stevens, G. A.: 1973, World Data Center Report UAG-28, Pt. II, p. 319.

Wang, H. T. and Ramaty, R.: 1974, Solar Phys. 36, 129.

Wang, H. T. and Ramaty, R.: 1975, Astrophy. J. 202, 532.

Wild, J. P., Smerd, S. F., and Weiss, A. A.: 1963, Ann. Rev. Astron. Astrophys. 1, 291.

Withbroe, G. L.: 1971, The Menzel Symposium, NBS Special Pub. 353, edited by K. B. Gebbie (Washington: U.S.G.P.O.), p. 127.